Delft University of Technology
Faculty of Applied Sciences
Kavli Institute of NanoScience
Physics of NanoElectronics

Leiden University
Faculty of Science
Leiden Observatory

Submicron Kinetic Inductance Detectors for SAFARI

Improving MKID sensitivity through width reduction

Master's thesis by : R.M.J. Janssen, BSc.
Student number : TUD1188488 & UL0781614

Professor : Prof. dr. ir. T.M. Klapwijk (TUD)
Supervisor : Dr. A. Endo (TUD)
Supervisor : Dr. B.R. Brandl (UL)
Period : September 2009 - December 2010

Summary

A longstanding hypothesis in astronomy is the hierarchical evolution of galaxies. While this theory is in agreement with a wide range of observations, it overestimates the number of high mass galaxies in the local universe. To match this observation a mechanism is required that stops the star formation (SF) in massive galaxies. It was recently shown that the radio-jets of active galactic nuclei (AGNs) have the energy to do this. However, even with this feedback it is not understood what is the exact evolutionary sequence that creates the massive galaxies we see today. What triggers and turns of SF and AGN activity? Do SF and AGN activity occur simultaneously or is either one triggered first?

These questions are difficult to answer at the moment, because of the lack of good far-infrared (FIR) detector technology. Microwave Kinetic Inductance Detectors (MKIDs) are a new detector technology based on superconducting resonators. These resonators are extremely sensitive to changes in the Cooper pair density. FIR photons are energetic enough to break Cooper pairs. This means a superconducting resonator can be used as a pixel for a FIR camera. The inherent multiplexing advantage of MKIDs means they can easily be fabricated in arrays of up to 5000 pixels.

By putting such an array in the SAFARI instrument on the cooled SPICA telescope a blind spectroscopic survey that can detect Milky Way sized galaxies out to redshift $z \sim 2$ will be possible. The large sample of galaxies that is obtained in this way can be used to construct the evolutionary time line that describes the co-evolution of AGN and their host galaxies.

However, in order to achieve background limited performance on a cooled telescope like SPICA the current Noise Equivalent Power of MKIDs must be improved from $NEP = 7 \times 10^{-19}$ W Hz$^{-0.5}$ to $NEP = 2 \times 10^{-19}$ W Hz$^{-0.5}$. This project aims to achieve this NEP reduction by lowering the width, s, of the resonator coplanar waveguide (CPW). Previous measurements on aluminum resonators with $s \geq 2\ \mu\mathrm{m}$ have shown that $NEP_A \propto s^{0.7}$ and $NEP_\theta \propto s^{0.4}$ for amplitude and phase read-out, respectively. These resonators were made using optical lithography, which limits the CPW width to $s \geq 2\ \mu\mathrm{m}$.

To make resonators with a submicron CPW a fabrication method using electron beam lithography and reactive ion etching was developed. The fabrication process presented in this thesis allows resonators as narrow as $s = 300$ nm.

Using this fabrication method NbTiN resonators with a central line width varying between 0.3 $\mu\mathrm{m}$ and 3 $\mu\mathrm{m}$ were made. These resonators were used to do a systematic study of the width dependence of the kinetic inductance fraction, quality factor, responsivity, read-out power, noise and NEP. For amplitude read-out a sensitivity improvement of $NEP_A \propto s^{0.21\pm0.11}$ was found. However, for phase read-out the sensitivity hardly improved, $NEP_\theta \propto s^{0.16\pm0.31}$. Because the magnetic penetration depth of NbTiN is longer than that of aluminum, the kinetic inductance fraction did not increase as strongly as accounted for in aluminum. This explains the discrepancy between the measured and theoretical width dependence.

Two prototype submicron pixel arrays were made in aluminum. The first used a hybrid design in which only the last 20% of the quarter-wave resonator had a $s = 660$ nm. A $NEP_A = 2.3 \times 10^{-18}$

W $\mathrm{Hz}^{-0.5}$ was measured for this design. However, using a thinner and higher quality film should improve the sensitivity of the hybrids at least to the level of the "regular" micron-sized resonator, $NEP_A \approx 4 \times 10^{-19}$ W $\mathrm{Hz}^{-0.5}$.

The second array used a design of fully submicron, $s = 600$ nm, half-wave resonators. These resonators had a responsivity that was an order of magnitude higher than the micron-sized resonators. Despite this improvement their NEP was only $NEP_A \approx 2 \times 10^{-18}$ W $\mathrm{Hz}^{-0.5}$. The main reason for this low sensitivity is the lower maximum read-out power. A decrease of 20 dB was found compared to the hybrid and micron-sized resonators. This decrease is larger than what was expected based on the experiments in NbTiN.

Based on these results power handling seems a key issue that will determine if submicron resonators are a viable route to improve the MKIDs sensitivity. These results of this project indicate that aluminum has a different width dependence of its power handling compared to NbTiN. Therefore, a systematic study of submicron resonators in aluminum, which focuses on the power handling, is required.

Contents

Summary **I**

1 Introduction **1**
- 1.1 Microwave Kinetic Inductance Detectors 2
- 1.2 Outline of this Thesis 3

2 Investigating Galaxy Evolution using SAFARI **5**
- 2.1 Creating the Local Universe through Galaxy Evolution 5
  - 2.1.1 Environmental Influence 6
  - 2.1.2 Galaxy Evolution at Redshift $z > 0.3$ 7
- 2.2 Observational Requirements for the Investigation of Galaxy Evolution 8
- 2.3 The SPICA Far-InfraRed Instrument 9
  - 2.3.1 SAFARI Detector Requirements 10
- 2.4 SAFARI Detector Candidates 12
  - 2.4.1 Ge:Ga Photoconductors 12
  - 2.4.2 Silicon Bolometers 13
  - 2.4.3 Superconducting Transition Edge Sensors 13
  - 2.4.4 Microwave Kinetic Inductance Detectors 14

3 Engineering High Sensitivity MKIDs **15**
- 3.1 Design of a MKID Pixel 15
- 3.2 A Coplanar Waveguide Resonator 16
  - 3.2.1 Capacitive Coupling between Parallel CPWs 17
- 3.3 A Superconducting Resonator 19
  - 3.3.1 Electrical Conductivity of a Superconductor 20
  - 3.3.2 Kinetic Inductance 22
- 3.4 MKID Read-Out 23
  - 3.4.1 Power Handling 25
- 3.5 Noise Sources in Superconducting Resonators 27
  - 3.5.1 Amplifier Noise 27
  - 3.5.2 Generation-Recombination Noise 27
  - 3.5.3 Fano Noise 27
  - 3.5.4 Two-Level System Noise 28
- 3.6 Resonator Responsivity 28
- 3.7 Noise Equivalent Power 29

4 Design and Fabrication of Submicron Resonators **33**
4.1 Material Choice . . . 34
4.2 Wafer Cleaning . . . 35
4.3 Film Deposition . . . 35
4.4 Electron Beam Lithography . . . 36
    4.4.1 Electron Sensitive Resist . . . 36
    4.4.2 Intelligent Electronic Pattern Design . . . 37
    4.4.3 Development . . . 38
4.5 Etching . . . 38
    4.5.1 Wet Etching . . . 38
    4.5.2 Dry Etching using SF_6 . . . 39
    4.5.3 Dry Etching using Chlorine . . . 40
4.6 Resist Removal . . . 41
4.7 Final Fabrication Results . . . 42

5 Properties of a Superconducting Resonator as a Function of Width **45**
5.1 Measurement Chip Design . . . 45
5.2 TU Delft Measurement Setup . . . 45
    5.2.1 Cryostat . . . 45
    5.2.2 Microwave Setup . . . 46
5.3 Measurement Results . . . 47
    5.3.1 Kinetic Induction Fraction . . . 48
    5.3.2 Internal Quality Factor . . . 50
    5.3.3 Responsivity . . . 51
    5.3.4 Power Handling . . . 53
    5.3.5 Noise . . . 55
5.4 “Noise Equivalent Power” . . . 55

6 Submicron MKID Pixels for SAFARI **57**
6.1 SRON Measurement Setup . . . 57
6.2 Width Hybrid Pixels . . . 58
    6.2.1 Hybrid Design . . . 58
    6.2.2 Basic Measurement Results . . . 59
6.3 Fully Submicron Pixels . . . 60
    6.3.1 Submicron Pixel Design . . . 60
    6.3.2 Basic Measurement Results . . . 60
6.4 Micron-sized Pixels . . . 61
    6.4.1 Micron-sized Pixel Design . . . 61
    6.4.2 Basic Measurement Results . . . 62
6.5 Pixel Layout Comparison . . . 63
    6.5.1 Kinetic Induction Fraction . . . 63
    6.5.2 Responsivity . . . 63
    6.5.3 Power Handling . . . 65
    6.5.4 Noise . . . 65
6.6 Noise Equivalent Power . . . 66

7 Conclusion and Discussion **69**

Bibliography **78**

A Submicron MKIDS Fabrication Process **79**

Acknowledgements **81**

Chapter 1

Introduction

The bewildering variety of galaxy morphologies has long marveled and challenged astronomers [38]. A striking example can be found in our astronomical backyard by looking at the Andromeda galaxy and Centaurus A. While these galaxies have approximately the same mass, the multi-wavelength images in figure 1.1 show a clear difference in morphology. This is already visible at optical wavelengths where Andromeda is a prototype spiral galaxy and Centaurus A is an elliptical galaxy. The big disk of dust around Centaurus A could fool one into thinking it is a spiral as well, but at infrared wavelengths one can look through these clouds and clearly see the bulge of stars behind the dust lane. The radio and X-ray images are dominated by Centaurus A's two enormous radio-lobes extending 250 kpc out off the galaxy to each side. A big difference compared to the Andromeda galaxy where the radiation of all the wavelengths closely follows the galaxies overall structure, consisting of a spiral armed disk with a small nucleus in the center.

The cause of the differences between Andromeda and Centaurus A can be found at infrared and sub-millimeter wavelengths. Inside the giant elliptical bulge of Centaurus A the remnants of a spiral galaxy can be seen [61, 41]. The gas and dust of this spiral galaxy is now accreted by the super massive black hole in the center of Centaurus A. The enormous amounts of energy released in this accretion process creates the giant radio lobes around Centaurus A. This makes Centaurus A one of the nearest Active Galactic Nuclei (AGNs). In the center of the Andromeda galaxy, and even in the center of the Milky Way, there is a super massive black hole with approximately the same mass as the black hole in Centaurus A. What is keeping these black holes from becoming an AGN as well?

The simple answer is the absence of gas and dust to feed the black hole. There are, however, many types of AGN as well. While it is assumed they are all the result of a super massive black hole accreting gas and dust, the complete underlying physics is not yet understood. To improve our understanding of the processes driving an AGN, one will need to investigate a large number of AGN and find a pattern in their differences.

The ideal wavelength to do this is the mid- to far-infrared. At these wavelengths dust, obscuring the AGN at optical wavelengths, becomes transparent and the emission is no longer dominated by the stars in the host galaxy. The mid- and far-infrared, $2 < \lambda < 200$ μm, is also the wavelength at which a blackbody spectrum with a temperature between 14 and 1450 K peaks. This is the temperature range of the gas expected to be at various distances from the black hole [70].

The perfect telescope to gather this data on a large number of AGN would be able to quickly map a large area of the sky with over a wide bandwidth using a low spectral resolution. The Japanese led SPICA (SPace Infrared telescope for Cosmology and Astrophysics) [64] mission goes a long way in fulfilling these requirements. This 3 m telescope will be able to map the sky using its low spectral

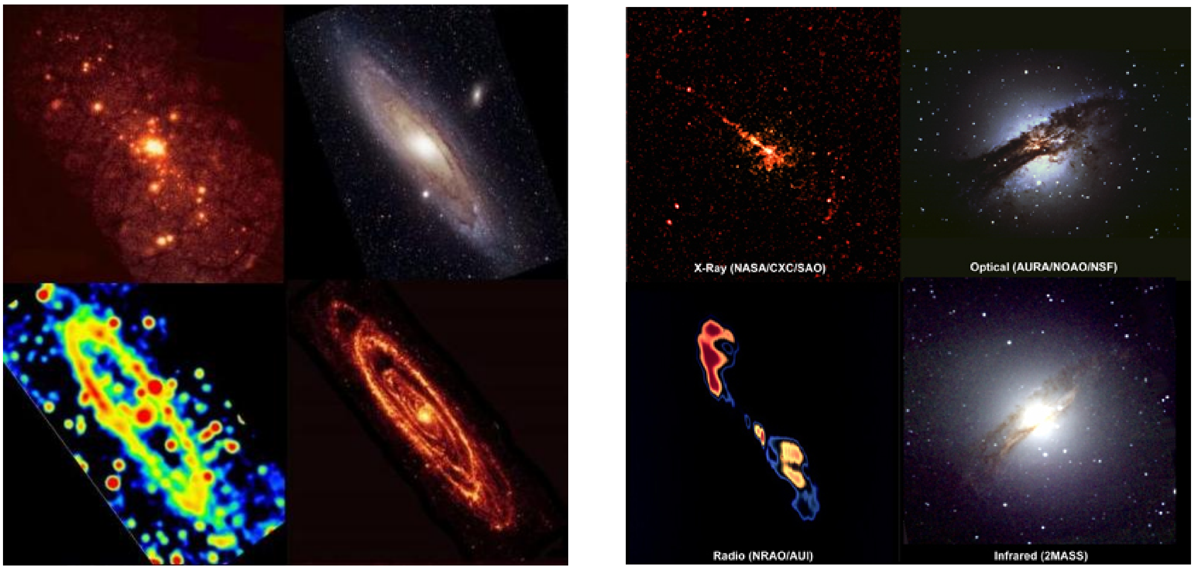

(a) The Andromeda Galaxy

(b) Centaurus A

Figure 1.1: Images of two nearby galaxies, Andromeda and Centaurus A. For both galaxies an observation in the X-ray (top left), optical (top right), radio (bottom left) and infrared (bottom right) is shown.

resolution instruments MIRMES and SAFARI for the mid- and far-infrared, respectively. The main advantage of this mission will be the fact the entire telescope is cooled to 4 K. This means that the background radiation limiting the performance is due to natural astronomical sources, instead of the telescopes own blackbody radiation. However, to achieve background limited performance detectors are required with an unprecedented low Noise Equivalent Power (NEP), $\mathrm{NEP} = 2\times10^{-19}$ W Hz$^{-0.5}$. One of the detector technologies attempting to reach this sensitivity are microwave kinetic inductance detectors (MKIDs) [19]. Just 7 years after their concept was published the first ground-based observations were made using these superconducting direct detectors [77, 62]. However, for background limited performance on SPICA the detectors' NEP needs to be improved by nearly 4 orders of magnitude compared to the performance on this first engineering runs. Experiments at SRON have already shown a $\mathrm{NEP} = 1.5\times10^{-18}$ W Hz$^{-0.5}$ [88]. This is close to the NEP shown by Transition Edge Sensors (TES), 1.3×10^{-18} W Hz$^{-0.5}$ [63], which is the lowest NEP today for any practical astronomical detector.

1.1 Microwave Kinetic Inductance Detectors

MKIDs or superconducting resonators are, as the second name implies, based on sensing the change in the properties of a superconductor with a resonant structure. In a superconductor there is a critical temperature, T_c, below which the electrons in the material form Cooper pairs. These electron pairs can travel through the material without scattering. This results in the absence of resistance to a DC current. However, there is an impedance against an AC current. The alternating electric field generating this AC current will continuously accelerate and decelerate the Cooper pairs. This means the kinetic energy of the Cooper pairs is either increasing or decreasing by gaining energy from or releasing energy to the electric field. This uptake and release of energy is equivalent to an inductance

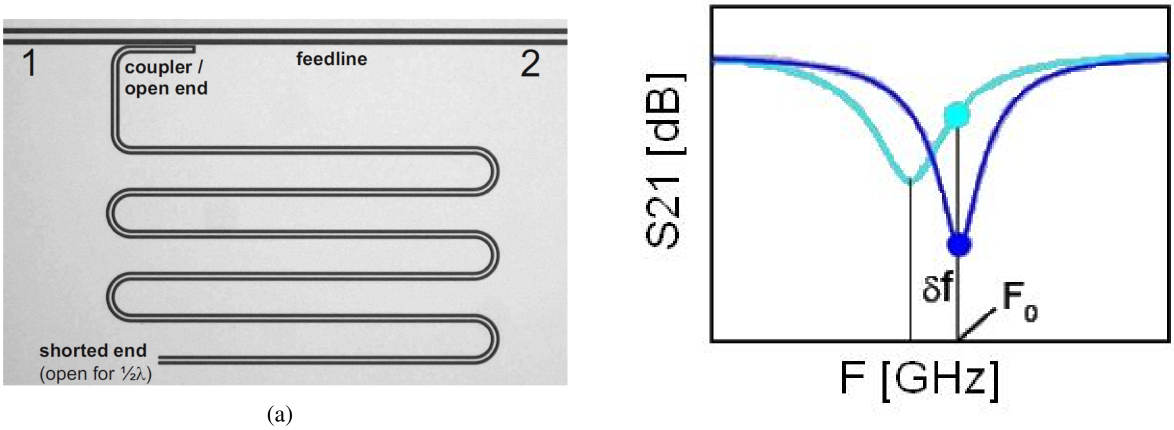

(a)

(b)

Figure 1.2: A superconducting resonator (a) and the resulting feedline transmission (b). The resonant structure, as shown in (a), is patterned in a superconducting film. When sending a microwave signal through the feedline at the top of (a) the transmission will show a dip, as shown in (b). This dip will be at the resonance frequency of the resonator. When incoming radiation breaks the Cooper pairs inside the superconducting material this changes the impedance of the resonator. This imdepance variation, which changes the resonance frequency of the resonator, changes the dark blue curve in figure (b) into the light blue curve. By measuring this change radiation can be detected.

in an electronic circuit.

By creating a pattern in the superconducting film similar to figure 1.2(a) this inductance can be probed. The meandering structure is the actual resonator, which is capacitively coupled to the feedline by means of its top tail. This resonator acts as an LC-circuit with a resonance frequency, $f = 1/\sqrt{LC}$. When a broadband microwave signal is sent along the feedline, the microwaves at the resonance frequency will experience the resonator as an electrical short circuit. This creates a dip in the feedline transmission, as shown in figure 1.2(b).

If photons with an energy higher than the binding energy of the Cooper pairs, $h\nu > 2\Delta$, are absorbed in the superconducting film, these photons will break Cooper pairs and create loose electrons, so-called quasi-particles. This change increases the resistance and inductance of the superconducting film. The increased inductance reduces the resonance frequency. The additional resistive losses decrease the dip depth. As a result the transmission dip is changed from the dark blue to the light blue curve in figure 1.2(b). By measuring the change in the transmission dip, hence sensing the change in kinetic inductance, one will have a structure sensitive to incoming radiation.

To reduce the NEP of these detectors this research will investigate the effects of a width reduction of the resonant structure. Because a narrow resonator will have a smaller volume the total amount of Cooper pairs will be lower. This gives a single broken Cooper pair a larger influence on the transmission dip, which increases the responsivity of the device. Since the responsivity is inversely proportional to the NEP it is therefore expected that a width reduction will improve the NEP.

1.2 Outline of this Thesis

This research attempts to reduce the Noise Equivalent Power (NEP) of MKIDS by reducing the width of the resonator below the limits of optical lithography. This reduction is needed to create background limited detectors for SAFARI. Chapter 2 will elaborate on the importance of SAFARI for the study of galaxy evolution. It will show which observations will be made possible if background limited performance is achieved by the SAFARI detectors. The current performance, advantages and disadvantages of all four candidate detectors for SAFARI, which includes MKIDs, will be discussed briefly. Chapter 3 will describe the physics and operational principle behind MKIDs. Chapter 3 will conclude by showing that, from a theoretical perspective, reducing the width of the resonator can be used to improve the detector sensitivity. The fabrication process described in chapter 4 was developed to make these narrow resonators. Using this fabrication process resonators were produced for a systematic investigation of the width dependence of various resonator properties. This investigation is presented in chapter 5. Based on these results two prototype submicron MKID pixel designs were made. The performance of these pixels on a single pixel and array level is shown in chapter 6. The change in NEP will be of particular interest in these measurements. In chapter 7 conclusions will be drawn from the results and recommendations will be made for future research.

The work presented in this thesis was done as a graduation project for the Master Applied Physics at Delft University of Technology (TUD) and the Master Astronomy at Leiden University (UL). The work was performed under the direct supervision of Dr. A. Endo in the research group Physics of NanoElectronics, lead by Prof. Dr. Ir. T.M. Klapwijk, at the faculty of Applied Sciences (TUD). Dr. B.R. Brandl was the supervisor for this project from the astronomy department (UL). The research was carried out in close collaboration with Netherlands Institute for Space Research (SRON).

Chapter 2

Investigating Galaxy Evolution using SAFARI

2.1 Creating the Local Universe through Galaxy Evolution

A longstanding hypothesis in astronomy is that galaxies evolve in a hierarchical scenario [44]. In this scenario the galaxies that we observe in the local universe, redshift $z < 0.3$, have been formed through the merging with other galaxies. This scenario predicts that the galaxy mass spectrum follows a power law. Such a mass spectrum is observed for the dark matter halos surrounding the galaxies in the local universe, but the galaxies themselves show an exponential cut-off at the high mass end [76]. The galaxies at this high mass end, $M_* > 10^{10.5}$ $\mathrm{M}_\odot$, are primarily bulge-dominated galaxies hosting an old, "red", stellar population. These galaxies are depleted of cold gas and have experienced little star formation (SF) in the last few billion years. This growth-stop is in sharp contrast with the active SF in the family of disk-dominated galaxies. These galaxies have masses below $M_* < 10^{10.5}$ $\mathrm{M}_\odot$, are rich in cold gas and host a young, "blue", stellar population.

To explain these observations a mechanism is required that stops the star formation in high mass galaxies. The stellar winds of massive stars and shock waves of supernova explosions could potentially inject enough energy to expel all the cold gas from the interstellar medium (ISM) of a galaxy [37] and decrease the star formation rate (SFR). However, a recent discovery points towards different feedback mechanism. In the local universe a strong correlation was found between the mass of a galaxies super massive black hole (SMBH) and key galaxy properties, such as the luminosity [47] and the mass of its bulge [30]. This correlation suggests a strong link between the growth of a galactic bulge through star formation and the mechanism that turns a quiescent SMBH into an Active Galactic Nucleus (AGN).

An AGN is believed to be matter falling into a SMBH through its relativistic potential [45]. This process is extremely efficient at releasing energy. As a result AGNs are small, but extremely luminous objects. Because AGNs can have up to 100 times the bolometric luminosity of their host galaxy, it can be difficult to observe this host if the AGNs emission is seen directly. Luckily, most of the highly energetic emission from of the AGN is absorbed by the various structures of gas and dust around the SMBH. This gives AGN hosts a unique spectrum that includes high-ionization emission lines in the ultraviolet (UV), optical (VIS) and infrared (IR) as well as excess mid-infrared (MIR) emission from the dusty torus.

In the local universe AGNs are generally hosted by galaxies from the so-called "green" valley. These hybrid galaxies with a typical mass of $M_* \approx 10^{10.5}$ $\mathrm{M}_\odot$ form the transition between the red and blue galaxy population described above. They have the structure of red galaxies, but the young stellar population of blue galaxies. The mass consumption rates of SF and AGN accretion in “green” valley galaxies is in agreement with the $\frac{M_*}{M_{SMBH}} \approx 10^3$ ratio observed in nearby bulge galaxies. However, it is found that this activity is not triggered by major mergers, $M_1 : M_2 < 4 : 1$, as predicted by the hierarchical evolution [14]. Instead minor mergers, $M_1 : M_2 > 4 : 1$, secular cold gas accretion and the mass loss through stellar winds are required to provide the cold gas for both SF and AGN activity [37, 75, 50].

In addition to the so-called “quasar” mode AGN described above there is another type of AGN found in the most massive elliptical galaxies [11]. These “radio” mode AGN [17] accrete the hot gas from the X-ray halo around them [12]. Spherical cooling flows bring this gas into the galaxy [13] where it is accreted by the SMBH in a radiatively inefficient way. As a result, most of the energy is not released by emission, but through the creation of collimated relativistic outflows of radio-emitting plasma. These jets carry enough energy to blow out the ISM, stopping SF, and large parts of the inter galactic medium (IGM) around the host galaxy. Direct evidence for this is provided by the massive bubbles of X-ray emitting gas around radio galaxies [28].

While we have now identified a feedback mechanism that can stop SF, it is not understood what is the evolutionary sequence that creates the old and massive galaxies observed locally. What triggers the SF? What triggers the AGN to turn of SF? Do SF and AGN activity occur simultaneously or is either one triggered first? How is the tight correlation between M_{SBMH} and M_* created in this scenario? Where do major merging events, the backbone of hierarchical evolution, fit in the picture?

To answer these questions we will need to trace back the formation of local elliptical galaxies in the history of the universe.

2.1.1 Environmental Influence

Before investigating the history of local galaxies, we can look into the effects the environment has on them. The universe today is highly non-uniform, as can be seen from a rendering of the millennium simulation at $z = 1.4$ [80] shown in figure 2.4. There are regions where a large number of galaxies have clustered together, but also places where only a few galaxies are still present. These different environments also influence a galaxy’s evolution.

The obvious candidate to be influenced by the environment is the galaxy merging rate. An obvious relation would be the increase of the merging rate with increasing density [53]. However, observations indicate that in the local universe it is mainly galaxies in small groups, which have a low to intermediate density, that merge [67]. This is because at low redshift the internal velocity dispersion of galaxies in a cluster is so high that merging is rare [34].

The environment also influences AGN activity and SFRs. It has been shown by Tasse et al. [82] for galaxies at redshift $z \sim 0.7$ that radio-mode AGNs are preferentially located in dense cluster environments. These environments also have the lowest SFR.

While this is true for the local universe Oliver et al. [66] show that for increasing redshift the preferred environment for SF shifts from a low density in the local universe to a high density at $z = 2$. Semi-Analytical Models (SAMs), which simulate the evolution of the universe to create the situation observed locally, show that between these two redshifts also the major-merger rate, τ^{-1}, increases significantly. This increase can be described, on average, by $\tau^{-1} \propto (1 + z)^3$. However, a closer look reveals that there has been a steady decline in the major-merger rate inside clusters since $z = 1$. The major-merger rate in galaxy groups and isolated galaxies on the other hand shows an increase since $z = 1$ [34]. To confirm these simulations, observations are required that map galaxies in different environments out to redshift $z \approx 2$.

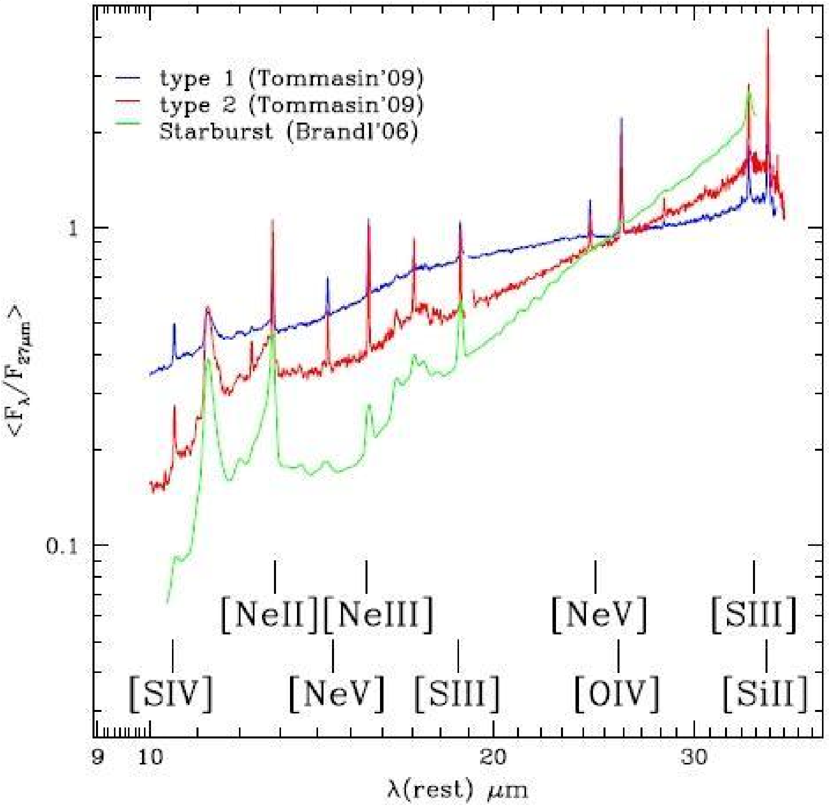

Figure 2.1: The mid-infrared spectra of 2 quasar-mode AGN in the local universe compared to that of a starburst galaxy. Image taken from [79]

2.1.2 Galaxy Evolution at Redshift z > 0.3

Using deep optical and X-ray observations it was found that both SF and AGN activity have decreased by an order of magnitude since redshift $z \sim 2$ [60]. This means most of the galaxies seen in the local universe are the result of evolution at redshifts $1 < z < 2$.

This is supported by the recent discovery of a population of massive, dusty galaxies, which emit most of their radiation in the infrared and sub-mm [24, 39]. These (Ultra) Luminous InfraRed Galaxies ((U)LIRGs) are presumed to be the result of major merging events. The merging event clusters the cold gas, which results in high SFRs. This gives (U)LIRGs a young and luminous stellar population. These stars are thought to be the progenitors of the old stellar population seen in local elliptical galaxies. However, if all the (U)LIRGs would be allowed to passively age this would create an overabundance of massive galaxies in the local universe. Therefore, (U)LIRGs must trigger an AGN at some point in their evolution. However, it is an open question how many of the (U)LIRGs host an AGN [52]. Deep observations of a small number of sources in the X-ray, optical, IR and sub-mm have been made. But these observations are consistent with scenarios of no AGN, a weak AGN and a heavily obscured AGN [1].

The small sample size is the weakness of our current understanding of galaxy evolution. Each galaxy that we observe is a snapshot of its own evolutionary timeline. By collection a large sample of galaxies, and determining for each of them the relative SF and AGN activity, one could reconstruct the timeline that describes the co-evolution of AGN and their host galaxies.

2.2 Observational Requirements for the Investigation of Galaxy Evolution

(U)LIRGs were only discovered so recently, because they are generally not identified as massive galaxies in optical surveys. Despite their young stellar population, they emit most of their radiation in the infrared. The dust inside (U)LIRGs absorbs most of the ultraviolet and optical light of the young stars. This energy is then emitted at infrared wavelengths. Dust obscuration is not only present in (U)LIRGs, however. Both SF and AGN activity are often enshrouded in optically thick dust [71]. This makes tracking of the SF and AGN activity through the history of the universe difficult.

Luckily mid- and far-infrared observation can still discriminate between SF and AGN activity, because the dust emission is influenced by the type of radiation that is heating it. Dust close to an AGN will be subject to much more X-ray emission than dust near a young star, which typically emits in the UV. The resulting temperature difference means that AGNs emit most of their IR radiation at wavelengths $\lambda < 60\ \mu\mathrm{m}$, while star formation dominates the spectral energy distribution (SED) at longer wavelengths. The dominant energy source in a galaxy can therefore be determined using broadband IR emission [70].

However, this method is too crude to determine the relative strength of the SF and AGN activity, which are often present simultaneously. This relative strength can still be determined, because UV and X-ray photons ionize atoms differently. This means the gas around young stars and AGN cools through different emission lines. Figure 2.1 shows the IR spectra of an AGN that is obscured by its own torus (type II, red), an AGN that does not have this obscuration (type I, blue), and a starburst galaxy (green), which is dominated by SF activity. Both activities will produce strong [NeII]12.8 $\mu\mathrm{m}$ and [OIII]88 $\mu\mathrm{m}$ emission. However, the AGN emission creates more [OIV]25.91 $\mu\mathrm{m}$ than SF and the HII region around young stars emits more [CII]158 $\mu\mathrm{m}$. This means infrared spectroscopy can be used to determine the relative contribution to the luminosity. From this the relative gas consumption of AGN and SF activity can be determined [79].

Another advantage of IR spectroscopy is that it helps resolve individual objects. The long wavelength of FIR radiation means the diffraction limited beam of a telescope is relatively big. In addition to this the number of sources in the FIR is larger than in any other wavelength. The combination of a high source density and large beam means that FIR telescopes will see multiple sources in one beam. This blurs the individual sources as can be seen in figure 2.2(a). Confusion limited observations like these make identification of individual (weak) sources difficult. A larger telescope improves the resolution, but launching a very large FIR telescope into space is difficult. FIR observations can only be done from space, because FIR radiation is absorbed by the atmosphere of the earth. Luckily, the availability of spectroscopy can help astronomers beat the confusion limit. Each astronomical source has a different SED, because of a different redshift for example. Therefore, the relative strength of different sources will vary as a function of wavelength, as can be seen in figure 2.2. By correlating the positions of each source between wavelengths individual sources can still be identified.

While spectroscopy helps identifying individual sources, these sources still need to be detected. A Milky Way type galaxy at $z = 2$ is extremely weak. It has a bolometric flux of $3.5 \times 10^{-18}\ \mathrm{W\,m^{-2}}$. To detect a large sample of these galaxies within a reasonable observation time a very sensitive instrument is required. Combined with a large field of view (FOV) this will create an instrument with a high mapping speed. This is exactly what is required to create a 3D map of the universe.

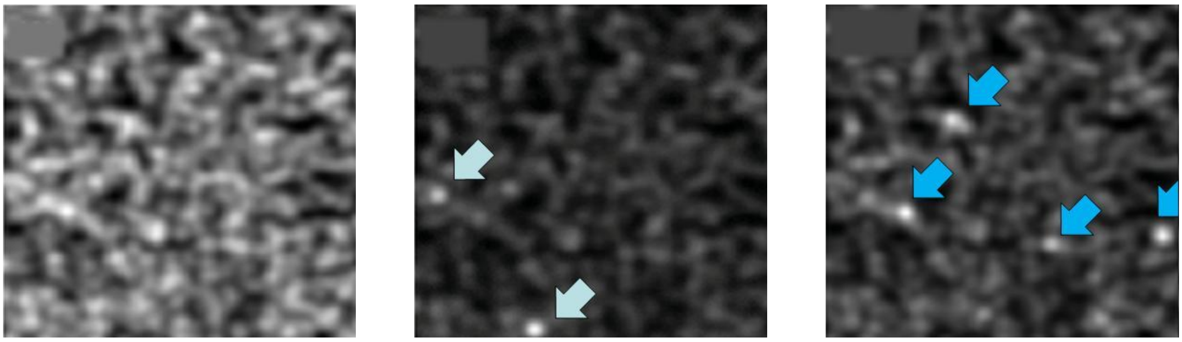

(a) Photometry $\lambda = 120\ \mu$m (b) Spectroscopy $\lambda = 63.2\ \mu$m (c) Spectroscopy $\lambda = 58.3\ \mu$m

Figure 2.2: Using spectroscopy SAFARI will be able to resolve the confusion limited observations in the far-infrared [29]. While it is difficult to identify individual sources in a photometric observation, the difference in their spectra means they appear in different spectroscopic slices.

To summarize, the ideal instrument for the study of galaxy evolution will meet the following requirements:

- Observe in the mid- and far-IR to avoid limitations caused by dust obscuration.
- A spectroscopic observation mode to distinguish between AGN and SF activity and beat the confusion limit.
- A high sensitivity to detect Milky Way sized galaxies out to $z > 2$ and map the sky quickly.
- A large field of view to further improve the mapping speed.

2.3 The SPICA Far-InfraRed Instrument

The instrument that suits these requirements is the SPICA FIR Instrument (SAFARI). SAFARI is the European contribution to the SPICA (SPace Infrared telescope for Cosmology and Astrophysics) mission, which is scheduled for launch in 2018 [64]. SAFARI is an image Fourier Transform Spectrometer (iFTS) that provides continuous wavelength coverage between $35 < \lambda < 210\ \mu$m. The advantage of the iFTS design is that it naturally provides both a photometric mode and spectroscopic mode. The latter can reach a spectral resolution up to $R \sim 1000$. After the beam combiner of the interferometer the image is simultaneously focused onto three focal plane arrays (FPAs) of cryogenic detectors. Each of these arrays Nyquist samples the full 2×2 arcmin FOV. The FOV is limited by the design of the iFTS.

The PACS integral field spectrograph [69] has similar specifications for wavelength coverage, spectral resolution and FOV. The advantage of SAFARI is that it is mounted on SPICA instead of the Herschel space telescope. SPICA and Herschel are both 3.0 m class space telescopes designed for observations in the mid- and far-infrared. This gives the instruments on both telescopes the same diffraction limited resolution. However, the main advantage of SPICA over other space-born infrared observatories, like Herschel, is the fact that the entire 3.0 m telescope will be cooled to 4 K. This means that the background radiation seen by the instruments on SPICA is not the blackbody radiation of the telescope, but the the zodiacal and cirrus emission, as shown in figure 2.3. This gives SAFARI a spectroscopic

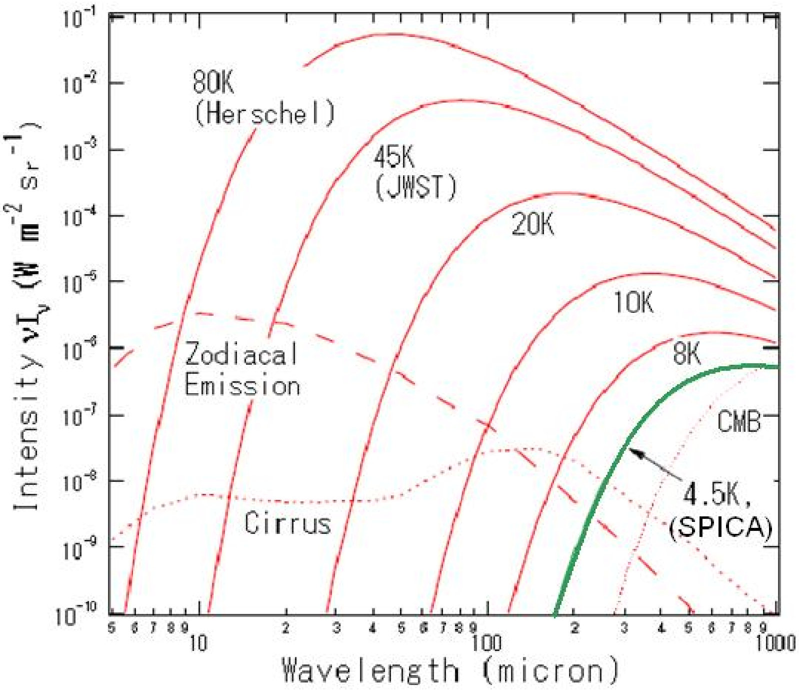

Figure 2.3: The background emission that limits the telescope performance of various telescopes. Any far-infrared instrument on the Herschel and James Webb Space Telescope (JWST) will see the blackbody of the telescope as their background. However, instruments on SPICA, which is cooled to 4 K, will see the natural background created by cirrus and zodiacal emission. Compared to Herschel this gives an improvement of 2 orders of magnitude in photometric sensitivity [65].

sensitivity of 3×10^{-19} W m^{-2} (5σ,1 hour) [29] compared to only 5×10^{-18} W m^{-2} for PACS [69]. In the photometric mode the difference is even bigger. SAFARI has a sensitivity of 50 μJy (5σ,1 hour) while PACS only manages 5.1 mJy.

The effect of this sensitivity improvement is best shown in the difference in mapping speed. Figure 2.4 shows a rendering of the millenium simulation at $z = 1.4$ [80] with 3 boxes. The blue box is the FOV of PACS. To map this 1 arcmin^2 with a spectral resolution of $R = 1000$ to an image depth of 5×10^{-19} W m^{-2} will require 1800 hours of observation time. An image of the same depth made by SAFARI, whose FOV is indicated by the yellow square, will have the size of 1 degree^2 (green box) after only 900 hours. This image will contain the spectra of all galaxies with a luminosity $L \approx 10^{11}$ $L_\odot$ out to $z = 1$ and $L \approx 10^{12}$ $L_\odot$ out to $z = 2$. This means SAFARI allows us to trace the evolution of modest - Milky Way type - galaxies out to $z \sim 3$ by means of a blind spectroscopic survey.

2.3.1 SAFARI Detector Requirements

To reach the mapping speed illustrated in figure 2.4 the detectors in SAFARIs focal plane must meet some very challenging requirements. The critical driver is the sensitivity. Expressed in Noise Equivalent Power (NEP) the sensitivity must be 2×10^{-19} W Hz$^{-0.5}$. This is crucial in order to characterize a large number of sources spectroscopically. Since observation time, $t_{obs} \propto NEP^2$, loss of sensitivity will quickly decrease the mapping speed. In addition, for a $NEP > 4 \times 10^{-19}$ W Hz$^{-0.5}$ SAFARI will become detector limited. This means the signal-to-noise ratio, S/N, becomes proportional to the

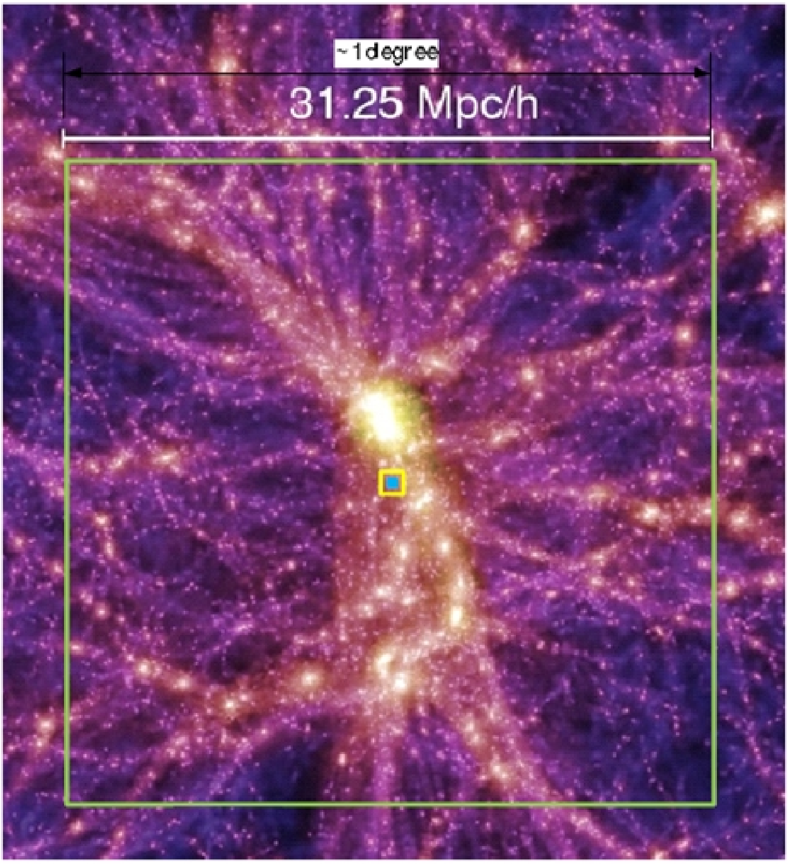

Figure 2.4: A rendering of the millenium simulation at $z = 1.4$ [80]. It clearly shows that the universe is non-uniform. A large section of space will need to be mapped in order to determine the environmental effect on galaxy evolution at various redshift. The SPICA/SAFARI combination is far better suited for this than the Herschel/PACS instruments. The improved sensitivity of SPICA/SAFARI, which has a field of view given by the yellow square, allows it to spectroscopically ($R = 1000$) map a full square degree of sky (green box) in 900 hours. To reach the same spectral resolution and image depth of 5×10^{-19} W m^{-2} Herschel/PACS will require 1800 hours for just its own field of view (blue square). [29]

detective efficiency, η_d, of the detector. Instead of $S/N \propto \sqrt{\eta_d}$ in a photon limited observation. In any case a high η_d is favorable. Therefore, the SAFARI design aims at $\eta_d = 0.80$.

The second requirement for a high mapping speed is a Nyquist sampled FOV [35]. To meet this requirement the 3 FPAs must meet the wavelength coverage, number of pixels and pixel size listed in table 2.1. Band 1 (B1) is the most demanding as it requires a 4096 pixel array with a pixel size of 480 $\mu\mathrm{m}$.

If the detectors of SAFARI meet both the sensitivity and FOV requirement they will be able to observe 7 to 10 sources simultaneously. These sources will not all have the same intensity, however. Therefore a large dynamic range, 2000:1, is very important for the detectors.

The final detector requirement is the response time. A higher response time means it takes longer to take a spectrum, because it takes longer to read and reset the entire array. A speed of response of 20

Hz is demanded from the SAFARI detectors.

2.4 SAFARI Detector Candidates

Four detector techonologies are attempting to meet the requirements for the SAFARI FPAs. These requirements, outlined in the previous section, are summarized in table 2.2. The current performance of the 4 competing technologies is given in this table as well. The 4 technologies are:

- Ge:Ga Photoconductors (PC): Detectors based on photoconductors are now very common on astronomical telescopes. However, making them work on the SAFARI frequencies means stretching the technology to the limit [23, 73].
- Silicon Bolometers (Si-bol): These detectors performed above expectations on the Herschel/PACS instrument [69]. Due to the similarities between SAFARI and PACS this makes silicon bolometers a viable candidate.
- Superconducting Transition Edge Sensors (TES): TES are slowly becoming the main detector technology for earthbound sub-mm and IR observations [2, 58]. Their potential for a very high sensitivity makes them the most likely candidate for SAFARI [55].
- Microwave Kinetic Inductance Detectors (MKIDs): These detectors developed from idea [19] to the first light at a telescope [77, 62] in just a decade. Their multiplexing advantage and steadily improving sensitivity [89] make them a candidate detector for SAFARI [31].

2.4.1 Ge:Ga Photoconductors

Photoconducting (PC) detectors are the workhorse of modern astronomy. Based on semi-conductor technology they have lifted on the technological development of this industry. When a photon is absorbed in a semi-conducting wafer it can lift an electron from the valance band into the conduction band, which decreases the resistance. This resistance change is measured using electrodes that immediately define the pixels [74].

For SAFARI a 2 band design based on gallium doped germanium (Ge:Ga) wafers is proposed. The first band, $50 < \lambda < 110$ μm, is covered by 4 monolithic Ge:Ga arrays of 32×32 pixels [23]. These arrays will be based on the AKARI detectors [22]. The second band is based on PACS technology [69]. It is an array of 32×32 pixels of stressed Ge:Ga [73]. The stressing is needed to modify the bandgap such that the detectors cover the $110 < \lambda < 210$ μm wavelength range.

The advantages of PCs are that they are proven technology and do not require an additional 50 mK

Table 2.1: Design goals for each of the 3 SAFARI bands. For each band the wavelength, λ (μm), and frequency range, ν (THz), is given. Along with the physical pixel size for a focal ratio of 20, the diffraction limited pixel size on the sky and number of required pixels to Nyquist samples the 1.9 by 1.9 arcmin field of view.

Band	λ μm	ν THz	Physical Pixel Pitch μm	Pixel Size on Sky arcsec	Number of Pixels
B1	$35 - 60$	$5.00 - 8.57$	480	1.8	64×64
B2	$60 - 110$	$2.73 - 5.00$	850	3.05	38×38
B3	$110 - 210$	$1.43 - 2.73$	1600	5.75	20×20

stage in the cooler. The iFTS design of SAFARI brings the first problem, however. An incident photon will reflect multiple times inside the Ge:Ga. This improves the detective efficiency, but gives a wavelength dependent detector sensitivity due to interference effects. This is no problem for broad band applications, but it is for a spectrometer. Anti-reflection coating is under development to combat this problem, but it will reduce the already low detection efficiency, $\eta_d = 0.25$.

The biggest problem for PCs is the silicon based cryogenic read-out electronics (CRE). The indium bump bonds connecting the silicon and Ge:Ga break during cool-down due to the difference in thermal expansion between the 2 wafers. This limits the array size to 16×16 pixels. The sensitivity is also limited by the noise of the CRE. The best proven performance is 8×10^{-18} W Hz$^{-0.5}$ by the PACS detectors. This sensitivity is not expected to be improved to the level required for SAFARI.

2.4.2 Silicon Bolometers

The surprise of PACS for the detector community was the high performance of the silicon bolometer detectors. In these detectors the light is caught in a resonant silicon cavity. In this cavity a grid-like silicon membrane is suspended. On this membrane a titanium-nitride (TiN) film is deposited that absorbs the incoming radiation. This absorption heats the TiN film. The change in temperature is measured by a silicon thermometer. This silicon is highly doped to create a high, temperature dependent, resistance. This resistance is read using CRE, which are bump bonded to the cavity walls. Because both are silicon based there is no problem with expansion differences.

In PACS [69] a 16×16 array is showing a sensitivity of 5×10^{-18} W Hz$^{-0.5}$. This technology is expected to be scalable to 32×32 pixels. Simulations show that operationing this array at 50 mK instead of 1.7 K will improve the sensitivity to 3×10^{-19} W Hz$^{-0.5}$. The downsides of these bolometers are the relatively large pixels size of 0.65 mm and the fact they have to be tuned to a very specific optical load. This means their dynamic range is severely limited. Their response time is also correlated with their sensitivity, $NEP \propto \sqrt{1/\tau}$.

2.4.3 Superconducting Transition Edge Sensors

Superconducting Transition Edge Sensors (TES) are based on the same basic principle as silicon bolometers. A feedhorn focuses the radiation on a titanium-gold (Ti/Au) bilayer. The absorption of the photons in this bilayer causes a temperature increase. Because the bilayer is voltage-biased at the superconducting transition to the normal state, this temperature change will cause a large resistance change [55]. The bilayer is suspended on a silicon-nitride (SiN) membrane with very long legs to

Table 2.2: An overview of the performance requirements for the detectors on SAFARI. The current performance of the 4 competing technologies is given as well. The 4 technologies are Ge:Ga photoconductors (PC), Silicon bolometers (Si-bol), Transition Edge Sensors (TES) and Microwave Kinetic Inductance Detectors (MKIDs).

Property	Requirements	PC	Si-bol	TES	MKIDS
Sensitivity (W Hz$^{-0.5}$)	2×10^{-19}	8×10^{-18}	5×10^{-18}	1.3×10^{-18}	1.5×10^{-18}
Detective Efficiency (%)	80	25	> 80	70	10
Dynamic Range	2000:1	-	500:1	-	5000:1
Pixel Size (mm)	0.48	0.50	0.65	0.55	0.45
Array Size	64×64	16×16	16×16	38×38	20×20
Response Time (ms)	50	-	-	2	2

create a very low thermal conductance, G. Combined with the low operating temperature, $T = 50$ mK, this gives a high sensitivity:

$$NEP_{TES} \approx \sqrt{4k_bT^2G} \tag{2.1}$$

Currently $NEP = 1 \times 10^{-18}$ W Hz$^{-0.5}$ is reached with a very long legged TES [46]. Because of these legs pixels are big, 2.5 mm. However, simulations show that by using a spiderweb design for the membrane a lower G and smaller pixel size can be achieved. A 5×5 array of B1 pixels has been fabricated using this design.

Upscaling to larger arrays brings up the Achilles heel of TES. In order to multiplex TES a SQUID read-out system is required for each pixel. This makes the devices sensitive to magnetic fields and means 1.1 wires/TES are required to read them out. This problem is in addition to the dynamic range and response time issues also found in silicon bolometers.

2.4.4 Microwave Kinetic Inductance Detectors

Microwave Kinetic Inductance Detectors (MKIDs) are a young technology that uses superconducting resonators to sense a change in the density of superconducting Cooper pairs [19]. These pairs are broken by incoming radiation. While a full description of their operation can be found in the next chapter, a few key aspects of MKIDs will be highlighted here.

MKIDs have an inherent multiplexing advantage, because the resonance frequency of the superconducting resonator can be changed through the resonator length. This means that up to 5000 resonators (or pixels) can be coupled to a single feedline, which requires only 2 cables to read. This multiplexing advantage means that MKIDs are the only technology, which is able to cover the B1 FOV with 1 array. Using multiple feedlines it would be possible to cover the entire 3.8×3.8 arcmin FOV alloted to SAFARI, if the iFTS did not limit it.

The two main disadvantages of MKIDs are the low operating temperature, which needs to be < 100 mK and the low detective efficiency. This low efficiency is due to the lens-antenna combination that is required to focus the light into the sensitive part of the resonator. These resonators are so sensitive that their performance is severely limited by any stray light.

SAFARI Detector Downselection

In June 2010, when this project was in the final measurement stages, the SAFARI consortium reconvened for the detector downselection. In this meeting TES were selected as the detector for SAFARI. MKIDs were mentioned as a technology to watch. Although the technological readiness level of the MKID detector is deemed to be insufficient for a space mission, these detectors are most likely the future of large FIR and sub-mm detector arrays [33].

Chapter 3

Engineering High Sensitivity MKIDs

3.1 Design of a MKID Pixel

The microwave kinetic inductance detector (MKID) pixel design is based on a superconducting microwave resonator. The design of a typical resonator is shown in figure 1.2(a). The resonance frequency, f_{res}, of this resonator corresponds to its length, l.

$$f_{res} = \frac{1}{4l\sqrt{L \times C}} \tag{3.1}$$

Where L and C are the total inductance and capacitance per unit length of the resonator. Instead of a short, which creates quarter-wave (QW) resonator, an open end can be used at the end of the resonator. This creates a half-wave (HW) resonator. A HW resonator should be twice as long as a QW for the same resonance frequency. The resonator, which is capacitively coupled to the feedline, forms a short circuit at resonance [8]. This create a dip in the forward transmission of the feedline, S_{21}. Because a single resonator only affects the transmission close to its resonance frequency, multiple resonantors with different lengths can be coupled to the same feedline. This gives MKIDs their inherent frequency domain multiplexing advantage, which allows up to 5000 resonators to be read-out with just 2 coaxial cables.

Due to the high quality factor of the superconducting resonator, which can be $Q \geq 1 \times 10^6$, the resonant microwave will experience a loss of only one millionth of the stored energy per resonant cycle. Therefore, the resonator is very sensitive to any other loss mechanism introduced during its operation. This happens when the superconducting Cooper Pairs are broken by a temperature increase or incoming radiation (see further section 3.3). This changes the frequency and depth of the transmission dip created by the resonator as described in section 3.4. By monitoring these changes a superconducting resonator can be used as a very sensitive radiation detector.

To couple radiation into the coplanar waveguide (CPW) geometry of the resonator a planar antenna is patterned close to the shorted end of a QW or in the center of a HW resonator (see figures 6.2 and 6.3). However, these antennas are usually much smaller than the pixel size, which is determined by the space required for the meandering CPW. To avoid the creation of a detector array with a very low active area, a silicon lens is used to focus the light on the antenna. The use of a lens can be avoided by using a lumped element resonator design [25]. In this design a tightly meandered superconducting line and interdigitated capacitor are used to form the resonator. The filling factor of these lines can be designed such that the superconducting line also acts as an absorber. For SAFARI the antenna design was chosen, because it decouples the microwave and radiation absorbing properties. This gives more

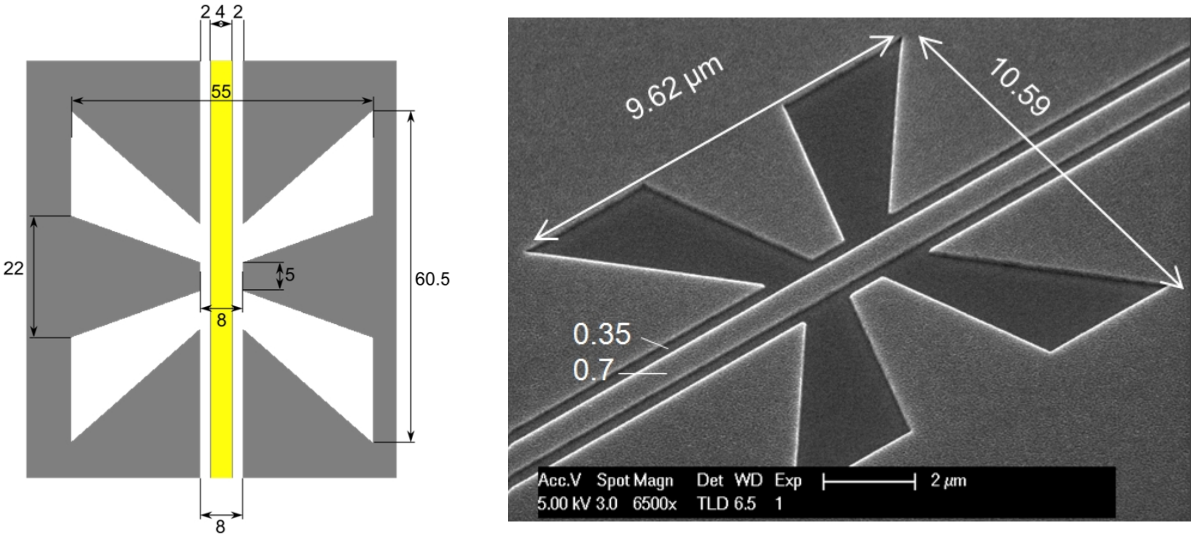

(a) Design at 1.1 THz

(b) Realization at 6.3 THz

Figure 3.1: The MKID pixels on SAFARI will use the X-slot antenna design of A. Neto (TUD/TNO) to couple radiation into the superconducting resonator.

parameters for optimization and allows the technology to be applied to many wavelengths by a simple change of the antenna design.
The antenna design proposed for SAFARI is the X-slot designed by A. Neto (TNO/TUD). This planar antenna design, as seen in figure 3.1(a), is optimized for a very broad absorption bandwidth. By scaling the complete design the center frequency can be tuned to the 3 SAFARI bands. Recent measurements with HEB mixers in spiral and twin slot planar antenna designs show that, in contrast to earlier publications, this can be done without efficiency loss [33]. However, scaling to the SAFARI B1 band means the central line of the CPW becomes $s = 700$ nm, as shown in figure 3.1(b).
Unless the antenna design is modified, the width of the CPW needs to be reduced to submicron dimensions. In the remainder of this chapter it will be shown that this width reduction also promises to give the noise equivalent power (NEP) reduction that is required to meet the SAFARI requirements.

3.2 A Coplanar Waveguide Resonator

The preferred transmission line geometry for superconducting resonators is the coplanar waveguide (CPW), which is the planar version of a coaxial cable. This geometry, as shown in figure 3.2(a), consists of a central transmission line of width s, which is separated from the ground planes by slots of width w. The advantages of a CPW transmission line over other transmission line geometries, for example a microstrip [57], are [15]:

- the easy fabrication. The CPW has a simple planar geometry that does not require processing on both sides of the substrate to make the short between the transmission line and the ground plane. All components using CPW transmission lines can be made by a single layer lithographical process (see further chapter 4).

- the minimal use of dielectrics, which are the main noise source in MKIDs [32].

- the balanced electro-magnetic (EM) fields. Because both s and w are smaller than the wavelength of the microwaves send through it, the CPW will operate in the (quasi-) TEM mode. This means the EM fields are perpendicular to the propagation velocity of the microwave, resulting in EM fields as sketched in the inset of figure 3.2(a). As can be seen from this inset all EM fields start and end within the CPW. This means other nearby conductors are not influenced by the transmission line. This shielding allows closer packaging and tighter meandering, which results in smaller pixels.
- the low radiative losses [85]. The even mode of the CPW, for which the EM fields are as shown in the inset of figure 3.2(a), will radiate very little. For typical resonator parameters the quality factor will not be limited by radiative losses unles $s > 75\ \mu\mathrm{m}$. However, if the ground planes on both sides of the resonator are not at the same potential, EM field in the CPW odd-mode will arise. These EM fields will go directly from the left to the right ground plane. This odd mode does radiate strongly. Suppressing this odd mode can be done by connecting both sides of the CPW using wire bonds or bridges.

The current generated by the EM field in a CPW will experience both a capacitance, C_g, and inductance, L_g, due to the geometry of the CPW. The value of this geometrical capacitance and inductance is given by [15]:

$$L_g = \frac{\mu_0}{4}\frac{K(k')}{K(k)} \tag{3.2}$$

$$C_g = 4\epsilon_0\epsilon_{eff}\frac{K(k)}{K(k')} \tag{3.3}$$

Where $K(x)$ is the complete elliptical integral of the first kind, $k = s/(s + 2w)$ and k' can be determined using $k^2 + k'^2 = 1$. In order to calculate the capacitance of the the CPW one will need to take into account that the electric fields are present in both the air/vacuum above the metal and in the substrate below it. This means that besides the permittivity of free space, ϵ_0, one needs to define an effective dielectric constant, ϵ_{eff}. Given that ϵ_r is the relative dielectic constant of the substrate, ϵ_{eff} can be approximated by $\epsilon_{eff} \approx (1 + \epsilon_r)/2$, if the metal film is thin compared to the width of the CPW.

Together with the kinetic inductance explained in section 3.3 L_g and C_g will determine the resonance frequency and impedance, $Z_0 = \sqrt{L/C}$, of the resonator. Due to the capacitive coupling of the resonator to the feedline (see further section 3.2.1) it does not really matter what the impedance of the resonator is. For the feedline, however, it is important that the impedance is close to 50 Ω. If this is not the case a mismatch will occur between the on chip feedline and the SMA cables leading to and from the chip. This causes unwanted standing waves in the feedline, which disturb the measurement.

3.2.1 Capacitive Coupling between Parallel CPWs

In order to couple the microwave signal from the feedline into the resonators a capacitive coupling is used. This capacitive coupling is achieved by putting the CPW of the resonator over a length L_c parallel to the feedline, which also uses a CPW geometry, as can be seen in figure 3.3. The two CPW structures are separated by a small ribbon of ground plane of width V. It is important to keep this ground plane to avoid stimulation of the odd mode in the feedline. In order to estimate the coupling to the resonator the microwave simulation package SONNET is used. In this package the layout of figure 3.3 is created using an infinitely thin sheet of lossless metal, sandwiched between a layer of silicon and a layer of air. The properties of which are given in table 3.1.

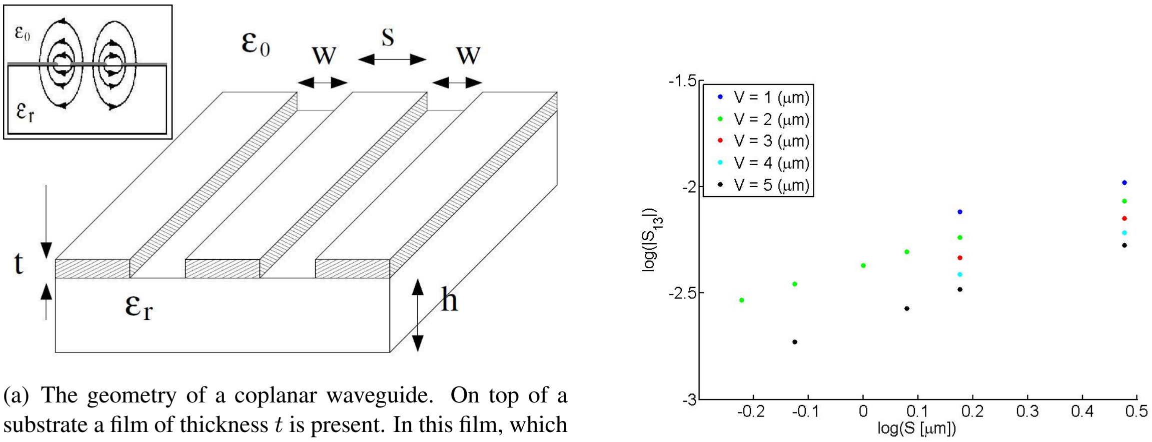

(a) The geometry of a coplanar waveguide. On top of a substrate a film of thickness t is present. In this film, which forms the ground plane of the CPW are 2 parallel slots of width w. These slots define the central transmission line that has a width s. The inset shows the electric field lines present in the TEM mode transmission of this line. This figure and inset were taken from Vardulakis [84] and Collins [15], respectively.

(b) Results of SONNET simulation to determine the dependency of the coupling strength on the width of the resonator, s, and the width of the ground plane, V, between resonator and feedline.

Figure 3.2: A schematic overview of a CPW geometry and the coupling strength between 2 parallel CPW transmission lines as simulated by SONNET.

SONNET can now be used to determine the scattering parameters between the three ports, S_{12}, S_{23} and S_{13}. The latter gives us the coupling strength between the feedline and the resonator. It was shown by Mazin [56] that $|S_{13}|$ depends linearly on L_c and f_{res}. For the research presented in this thesis the dependence on s, and V was investigated. The results for $L_c = 350$ μm and $f_{res} = 5$ GHz are shown in figure 3.2(b). It was found that:

$$|S_{13}| \propto f_{res} \times L_c \frac{s^{0.66}}{\sqrt{V}} \tag{3.4}$$

While the linear dependence on f_{res} and L_c is again found, the results of this investigation should not be trusted blindly. While the results presented here might give a reasonable first estimate it should not be used if accurate estimates are required. A problem of SONNET is that a uniform grid is enforced over the entire simulated area. In addition the structures rendered by SONNET are rounded to the nearest grid point. This means, for example, that a 200 nm grid spacing is required over the entire 1000×160 μm box to simulate the coupling of a $s = 600$ nm by $w = 400$ nm resonator to a $St = 10$ μm by $Wt = 6$ μm feedline. This makes the simulations computationally expensive. This severely limited the generation of data for submicron resonators and made simulation of $s = 300$ nm

Table 3.1: Properties of the dielectrics used in the SONNET simulation to determine the capacitive coupling strength to a resonator. The properties that define the dielectric are the thickness, t, relative dielectric constant, ϵ_r, dielectric loss tangent, $\tan\delta_e$, dielectric conductivity, σ_d, relative magnetic permeability, μ_r, and the magnetic loss tangent, $\tan\delta_m$.

Dielectric	t (μm)	ϵ_r	$\tan\delta_e$	σ_d (Ω^{-1}m^{-1})	μ_r	$\tan\delta_m$
Air	5000	1.0	0.0	0.0	1.0	0.0
Silicon	550	11.9	0.004	$4.4e-4$	1.0	0.0

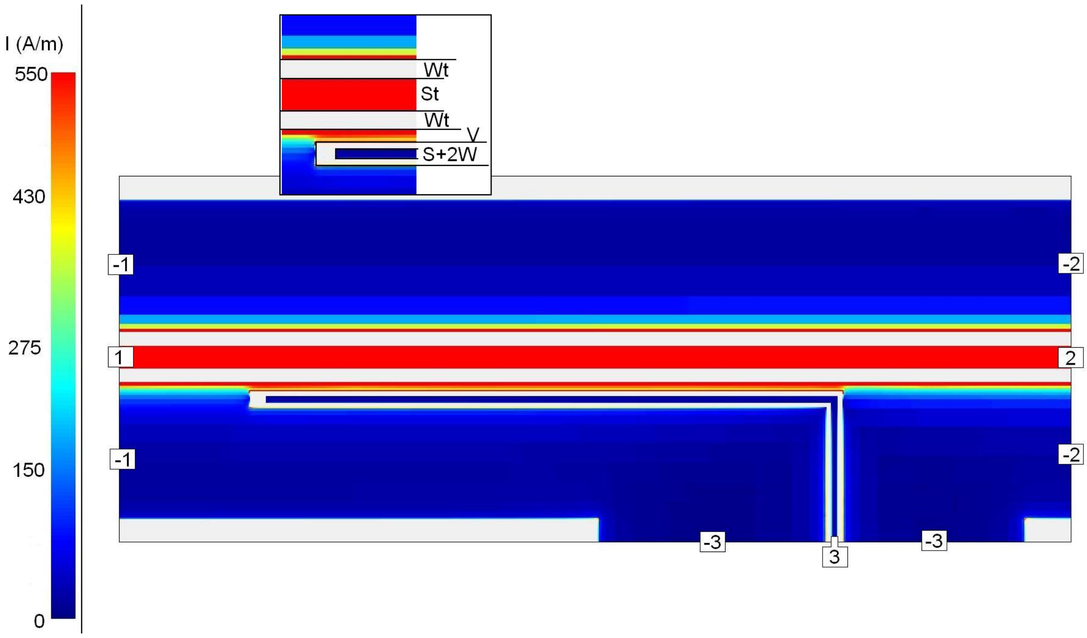

Figure 3.3: The geometry used during the SONNET simulations displaying a typical current density profile. The feedline runs from the left, port 1, to the right, port 2. Parallel to it runs a smaller CPW structure, which bends away to port 3. Negative ports are defined in SONNET such that the current into port x is the same as the current out of port $-x$. This structure is very similar to the coupler design used in this project. The coupler can be varied in length parallel to the throughline, ground plane width between the 2 central lines, V, and the central line width, S, and slot width, W, of the coupler or feedline (St, Wt). From the current profile it can be seen that a current is only running close to the CPW line and that a minute portion of the current is coupled into the resonator.

resonators impossible. In addition fabrication seems to affect the coupling as well. These simulations were therefore not confirmed experimentally in this work. Future research is advised to estimate the dependency on the coupler parameters using conformal mapping [90].

3.3 A Superconducting Resonator

Below the transition temperature, T_c, the electrons in a superconducting material form Cooper pairs [16]. The formation of these pairs between electrons of equal and opposite momentum and spin is energetically favorable due to the electron-phonon interactions in the material [4]. The binding energy of the Cooper pair is typically of the order of milli-electronvolt. At $T = 0$ K the binding energy, 2Δ, is given by:

$$2\Delta(0) = 3.528 k_b T_c \tag{3.5}$$

In which $k_b = 1.38 * 10^{-23}\ \mathrm{m^2\ kg\ s^{-2}\ K^{-1}}$ is the Boltzmann constant. This binding energy manifest itself as an energy gap in the superconducting density of states. In this gap around the Fermi level there are no states available, except the bosonic state of the Cooper pairs. However, when an energy $E > 2\Delta$ is supplied a Cooper pair can be broken into the 2 fermionic electrons it is created from. These excitations are usually called quasi-particles. The quasi-particle creation mechanism of interest for detector development is photon induced quasi-particle generation. However, since we can never cool our detector to the absolute 0, a more common mechanism that creates quasi-particles is the absorption of a thermal phonon. Eventually any quasi-particle will encounter another quasi-particle and recombine into a Cooper pair under the emission of a phonon. The characteristic timescale for this process is the quasi-particle relaxation time, τ_{qp}, which is given by [43]

$$\frac{1}{\tau_{qp}} = \frac{\sqrt{\pi}}{\tau_0} \left(\frac{2\Delta}{k_b T_c}\right)^{5/2} \sqrt{\frac{T}{T_c}} \exp\left(\frac{-\Delta}{k_b T}\right) \tag{3.6}$$

Where τ_0 is a material-specific electron-phonon scattering time. The continuous generation and recombination of quasi-particles under the emission and absorption of thermal phonons will create a steady-state number density of thermally excited quasi-particles, n_{qp}. For temperatures far below T_c, where MKIDs are usually operated, this density can be estimated using

$$n_{qp} = 2N(0)\sqrt{2\pi\Delta k_b T} e^{-\Delta/k_b T} \tag{3.7}$$

This approximation is accurate to within 2% at $T = 0.1T_c$ [84]. In equation 3.7 $N(0)$ is the single spin density of states at the Fermi level in the normal state. Δ is the temperature dependent energy gap of the superconductor. $\Delta(T)$ can be determined by inverting [83]:

$$\frac{1}{N(0)V_{eff}} = \int_{-\hbar\omega_D}^{\hbar\omega_D} \frac{1}{2\sqrt{E^2 + \Delta^2(T)}} \tanh\left(\frac{\sqrt{E^2 + \Delta^2(T)}}{(2k_b T)}\right) dE \tag{3.8}$$

In this equation V_{eff} is the effective attractive potential between electrons and ω_D is the Debye frequency. This is the highest possible phonon frequency and thus represents a cut-off frequency for the electron-phonon interaction. Using the reduced Planck's constant, $\hbar$, ω_D can be translated in the energy of the most energetic phonons.

Equation 3.8 also provides an indication why the macroscopic properties of different superconductors are so different. Both $N(0)V_{eff}$, the total phonon energy scattering potential, and the Debye frequency depend on the lattice structure of the material. Equation 3.8 can also be used to determine T_c by substituting $\Delta = 0$ during the inversion. This explains why T_c is different for different materials. In table 3.2 typical values of V_{eff}, $N(0)$, $\Delta(0)$, T_c and the Debye temperature, $\Theta_D = \hbar\omega_D/k_b$, can be found for NbTiN and aluminum.

3.3.1 Electrical Conductivity of a Superconductor

The formation of Cooper pairs in a superconductor results in the two characteristic macroscopic properties of a superconductor. The first of these is the lack of resistance against a DC current [42]. In a normal metal this resistance is caused by electrons scattering of the atoms in the lattice structure of the material. These scattering events changes the electrons momentum. Because the momentum

Table 3.2: Typical values for the Debye temperature, single spin density of states, phonon exchange potential, superconducting gap energy and transition temperature for the 2 superconducting materials used in this research. Values for NbTiN taken from [5] and for aluminum from Vardulakis [84].

Material	Θ_D (K)	$N(0)/10^{23}$ (eV^{-1} cm^{-3})	$V_{eff}/10^{23}$ (eV cm^3)	$\Delta(0)$ (meV)	T_c (K)
NbTiN	275	0.184	1.78	2.247	14.8
Al	420	0.174	0.97	0.193	1.27

of the electrons that form a Cooper pair is matched and a single scattering event cannot change both, Cooper pairs are resistant to scattering. This means Cooper pairs can travel through the superconductor without resistance and sustain a supercurrent, $\vec{J}_s$, even in the absence of an electric field London and London [51].

The second hallmark of a superconductor is the so-called Meissner effect [59]. In the presence of an external magnetic field a superconductor will generate a screening current at its surface. This screening current will generate its own magnetic field such that there is no net flux in the bulk of the superconductor. At the surface where the screening current is running the external magnetic field is allowed to penetrate. The characteristic length scale in which the external magnetic field decays is called the magnetic penetration depth, λ. The size of this magnetic penetration depth can be estimated by [81, 4]

$$\lambda \approx 100(\mathrm{nm})\sqrt{\frac{\rho(\mu\Omega\mathrm{cm})}{T_c(\mathrm{K})}} \tag{3.9}$$

At finite temperature Cooper pairs are not the only charge carriers in a superconductor. Quasi-particles behave as regular electrons. In the presence of an electric field, $\vec{E}$, they will be accelerated until they are scattered. This creates a second conduction channel of normal current, J_n, that is subject to the ohmic surface resistance, R_s. The Cooper pairs also have a "resistance" against the acceleration by the electric field. The mass of the Cooper pairs means they cannot instantaneously respond to changes in the electric field. In an alternating electric field with frequency ω, such as that of microwave read-out electronics, the Cooper pairs will continuously accelerate and decelerate. This results in a transfer of energy between the electric field and the kinetic energy of the Cooper pairs. In a macroscopic circuit this is observed as a surface impedance, L_s, to which the supercurrent, $\vec{J}_s$, is subject. Together R_s and L_s form the surface impedance of a superconductor.

$$Z_s = R_s + i\omega L_s \tag{3.10}$$

An alternative mathematical description of this phenomena is by means of the complex conductivity, $\sigma = \sigma_1 - i\sigma_2$. This quantity can be used to directly relate the electric field, $\vec{E}$, to the current it generates in the superconductor, $\vec{J}$.

$$\vec{J} = \vec{J}_n + \vec{J}_s = (\sigma_1 + i\sigma_2)\vec{E} \tag{3.11}$$

This equation does not hold, however, if the electric field varies over the size of the Cooper pair. The typical distance between the two electrons of a Cooper pair is given by the coherence length ξ. This coherence length is determined by the superconducting material dependent coherence length ξ_0 and the materials mean free path l_e.

$$\frac{1}{\xi} = \frac{1}{\xi_0} + \frac{1}{l_e} \tag{3.12}$$

While Cooper pairs are resistant to scattering of the atoms of the superconducting material, any contamination or disorder will have a different electron-phonon interaction. At the location of the contamination or lattice irregularity the electrons of a Cooper pair can scatter. This limits the mean free path in the superconductor.

If the electric field varies over the size of a Cooper pair, $\lambda \ll \xi$, the Cooper pair will "feel" the average electric field within its size [68]. Based on this principle Mattis and Bardeen [54] developed a microscopic theory to describe the electrodynamic response of a Cooper pair. Using this theory σ_1 and σ_2 can be determined for superconducting materials in the dirty ($l_e \ll \xi_0$) and extreme anomalous limit

($\xi_0 \gg \lambda$ and $l_e \gg \xi_0$). While this normally requires the evaluation of multiple integrals, the Mattis and Bardeen [54] integrals can be simplified in the limit $k_bT, \hbar\omega << \Delta$ [6].

$$\frac{\sigma_1}{\sigma_n} = \frac{4\Delta}{\hbar\omega} e^{-\Delta/(k_bT)} \sinh\left(\frac{\hbar\omega}{2k_bT}\right) K_0\left(\frac{\hbar\omega}{2k_bT}\right) \tag{3.13}$$

$$\frac{\sigma_2}{\sigma_n} = \frac{\pi\Delta}{\hbar\omega}\left[1 - 2e^{-\Delta/(k_bT)} e^{-\hbar\omega/(2k_bT)} I_0\left(\frac{\hbar\omega}{2k_bT}\right)\right] \tag{3.14}$$

Where I and K are modified Bessel functions of the first and second kind, respectively. Using Maxwell's equations this complex conductivity can be related to the surface impedance of the superconductor [84, 6].

$$Z_s = \sqrt{\frac{i\mu_0\omega}{\sigma_1 - i\sigma_2}} \coth\left(\frac{t}{\lambda}\sqrt{\frac{\sigma_2 + i\sigma_1}{\sigma_2}}\right) \tag{3.15}$$

At the low temperatures where resonators usually operate the inductance due to Cooper pairs will be far bigger than the resistance due to the quasi-particles, $\sigma_2 \gg \sigma_1$. This allows us to split the surface impedance back into its two components of surface resistance and surface inductance.

$$R_s = \mu_0\omega\lambda\frac{\beta\sigma_1}{2\sigma_2}\coth(t/\lambda) \tag{3.16}$$

Where $\beta = 1 + \frac{2t/\lambda}{\sinh(2t/\lambda)}$. The superconducting films used in this research are usually in the thin film limit, which means $\beta \approx 2$.

$$L_s = \mu_0\lambda\coth(t/\lambda) \tag{3.17}$$

It seems that the surface inductance does not depend on the complex conductivity. But the magnetic penetration depth can also be described using the complex conductivity.

$$\lambda(\omega, T) = \frac{1}{\sqrt{\mu_0\omega\sigma_2(\omega, T)}} \tag{3.18}$$

3.3.2 Kinetic Inductance

Due to the surface impedance in a superconducting film there is another inductance, which determines the MKIDs resonance frequency together with C_g and L_g. This second inductance is called the kinetic inductance, L_k, because it is related to the kinetic energy stored in the Cooper pairs. The kinetic inductance per unit length of a resonator will be determined by the surface inductance, L_s, and the resonator geometry.

$$L_k = g \times L_s \tag{3.19}$$

For a CPW the geometry factor, g, is the sum of the geometry factor for the central line, g_c, and the ground planes, g_g [15].

$$g_c = \frac{1}{4s(1-k^2)K^2(k)}\left[\pi + \ln\left(\frac{4\pi s}{t}\right) - k\ln\left(\frac{1+k}{1-k}\right)\right] \tag{3.20}$$

$$g_g = \frac{1}{4s(1-k^2)K^2(k)}\left[\pi + \ln\left(\frac{4\pi(s+2w)}{t}\right) - \frac{1}{k}\ln\left(\frac{1+k}{1-k}\right)\right] \tag{3.21}$$

Where $K(x)$ is the complete elliptical integral of the first kind and $k = s/(s+2w)$. These equations are accurate to within 10% for $t < 0.05S$ and $k < 0.8$.

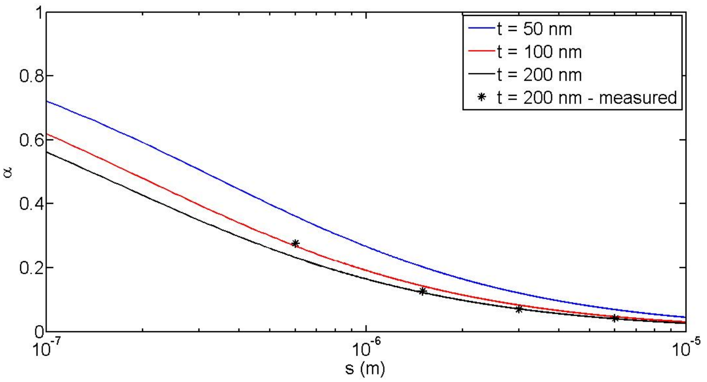

Figure 3.4: The kinetic induction fraction, α, as a function of the width of the central line in an aluminum film, $\lambda = 64$ nm, of thickness t on silicon substrate, $\epsilon_{eff} = 6.45$. The ratio of s/w is taken to be $3/2$. The trend in α is similar for all 3 thicknesses. The line also fits, for high s, the measured data of Gao [32] on 200 nm aluminum.

While the geometric inductance is completely dictated by the geometry of the resonator, the kinetic inductance can be changed by breaking Cooper pairs. This makes it useful to know how much of the inductance experienced by the microwave in the resonator is due to the geometry and how much due to Cooper pairs. Thus we define the kinetic inductance fraction α

$$\alpha = \frac{L_k}{L_g + L_k} = \frac{(g_c + g_g)L_s}{L_g + (g_c + g_g)L_s} \tag{3.22}$$

This kinetic inductance fraction depends strongly on the width of the resonator. The kinematic inductance fraction of a CPW line in an aluminium film, $\lambda = 64$ nm [32], on a high resistivity silicon substrate, $\epsilon_{eff} = 6.45$, is estimated based on equations 3.17 through 3.22. The result is shown in figure 3.4. This was done for 3 different film thicknesses. The ratio s/w was taken to be $3/2$ for comparison to the studies of Barends [6] and Gao [32]. The ratio $2/1$, more commonly used at SRON [88], will give a slightly higher kinetic induction fraction as their $3/2$ counterpart, but also a similar trend. It is clear that the kinetic inductance fraction strongly increases below a central line width of $1\ \mu\text{m}$. However, note that in this regime $t < 0.05S$ does not hold anymore, resulting in a larger uncertainty of the estimation. Measurements by Gao [32] of a 200 nm aluminum film, displayed in figure 3.4 as diamonds, show the equations given above underestimate the kinetic inductance fraction. Combining equations 3.1 and 3.22 shows that the actual change in resonance frequency due to the presence of a kinetic inductance is given by:

$$\alpha = 1 - \left(\frac{f_{res}}{f_{res}^{g}}\right)^2 \tag{3.23}$$

Where f_{res}^{g} is the resonance frequency if there is only a geometric capacitance and inductance. f_{res} on the other hand does include the kinetic inductance.

3.4 MKID Read-Out

MKIDs are read-out by sending a microwave signal over the feedline to which all resonators are coupled. On resonance the resonator loads the feedline, producing a dip in its transmission, S_{21}. This transmission dip, as shown in figure 3.5, can be described by [6]

$$S_{21}(f) = \frac{S_{21}^{min} + i2Q_l \frac{\delta f_{res}}{f_{res}}}{1 + i2Q_l \frac{\delta f_{res}}{f_{res}}} \tag{3.24}$$

Where $\delta f_{res} = f - f_{res}$. The maximum depth of the resonance dip, S_{21}^{min}, is given by:

$$S_{21}^{min} = \frac{Q_c}{Q_c + Q_i} \tag{3.25}$$

The dip depth is set by the losses inside the resonator. These losses are described by means of a quality factor Q. $1/Q$ is the fraction of the energy stored in the resonator that is lost per resonance cycle. The internal loss mechanism in a superconducting resonator is the dissipation of energy by the quasi-particles. Because the number of quasi-particles is very low at the operating temperature of MKIDs, internal quality factors, Q_i, between 1×10^5 and 1×10^6 are not uncommon.

$$Q_i = \frac{\omega L}{R} = \frac{\omega L_s}{\alpha R_s} \tag{3.26}$$

Where $\omega = 2\pi f$. But there is a second loss mechanism, which can be to some degree designed. The coupler does not only send microwaves into the resonator, but also allows the radiation to escape back into the throughline. The energy loss to the feedline is described with the coupling quality factor, Q_c, which depends on the scattering parameter S_{13} determined in section 3.2.1.

$$Q_c = \frac{n\pi}{2|S_{13}|^2} \tag{3.27}$$

Where n is the resonance mode in the QW resonator: $n\lambda/4$. By adding the losses the loaded quality factor, Q_l can be found.

$$\frac{1}{Q_l} = \frac{1}{Q_i} + \frac{1}{Q_c} = \frac{Q_i Q_c}{Qi + Qc} \tag{3.28}$$

When photons are absorbed in the resonator the number of quasi-particles increases. This changes the complex conductivity and increases the losses in the resonator. It was shown by Gao [32] that for the temperature and frequency range in which MKIDs operate the change in complex conductivity due to thermal and optically excited quasi-particles is approximately equal. This is convenient from an experimental point of view, because it is easier to create a well defined number of quasi-particles by increasing the temperature (equation 3.7). The effect of temperature on the transmission near the resonance frequency of a $s = 1$ μm NbTiN resonator can be seen in figure 3.5. As the temperature is increase from 320 mK to 3 K the number of quasi-particles within the resonator increases. The increased surface resistance reduces the depth of the transmission dip. Because the decreased number of Cooper pairs decreases σ_2 the kinetic inductance increases. This decreases the resonance frequency. By measuring the change in frequency and transmission depth a very sensitive thermometer or radiation detector can be made. However, for the actual read-out electronics a different parameter space is used. Typically a mixer is used to measure the real and imaginary part of S_{12}. When these variables are plotted in the complex plane a circle is traced, as shown in figure 3.6. In the complex plane the radius (or amplitude) of the resonance circle, $A = Q_l/(2Q_c)$, is a measure for the losses in the resonator. In amplitude read-out the change in amplitude is measured from which the increase in losses can be determined.

$$\delta A = \frac{2Q_c}{Q_i + Q_c} \frac{\delta Q_i}{Q_i} \tag{3.29}$$

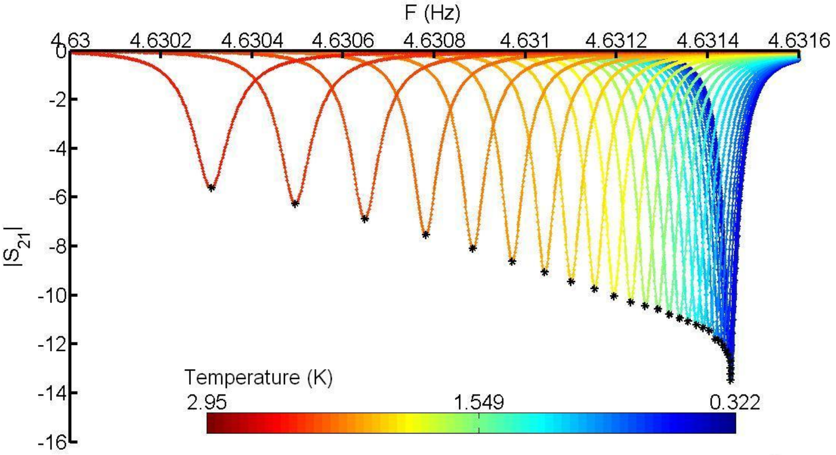

Figure 3.5: The feedline transmission near the resonance frequency of a $s = 1\ \mu\text{m}$ NbTiN resonator. As the temperature increases the number of thermally excited quasi-particles increases. This increases the kinetic inductance, which shifts the resonance frequency down. The larger number of quasi-particles also increases the losses in the resonator, which results in a shallower dip.

The second read-out mode of a MKID is phase read-out, which is equivalent to the frequency shift.

$$\delta\theta = -4Q_l \frac{\delta\omega_{res}}{\omega_{res}} \tag{3.30}$$

When monitoring a specific frequency, for example the resonators resonance frequency at 320 mK, the phase of this frequency will change as the temperature is increased. This example is illustrated by the black circles in figure 3.6 where the base resonance frequency traces a path from $\theta = 0$ ($[\mathrm{Re}(S_{12}), \mathrm{Im}(S_{12})] = [0, -0.4]$) at 320 mK to $\theta = \pi$ at 3 K.

3.4.1 Power Handling

Superconducting resonators can in principle be used to store a single microwave photon [86]. However, for resonators used as photon detectors it is desirable to maximize the read-out power, P_{read}. A higher read-out power increases the signal-to-noise ratio of the phase and amplitude measurement by the read-out electronics. A higher read-out power also increases the power inside the resonator, P_{int}.

$$P_{int} \cong \frac{2Q_l^2}{\pi Q_c} \frac{Z_{feedline}}{Z_{res}} P_{read} \tag{3.31}$$

The two-level system noise that dominates in phase read-out is shown to decrease for increasing internal power. Unfortunately, there is a maximum internal power above which the resonator starts showing non-linear behavior. This non-linear behavior, which is shown in figure 3.7, is undesirable in a detector.

The mechanism that causes this non-linear behavior is poorly understood. Many effects are a potential candidate, but microwave heating seems to dominate at the low operating temperatures of MKIDs [21]. It is difficult to identify the dominator mechanism that limits power handling, because all mechanism depend on the microwave current density in the resonator. Because the current density is limited

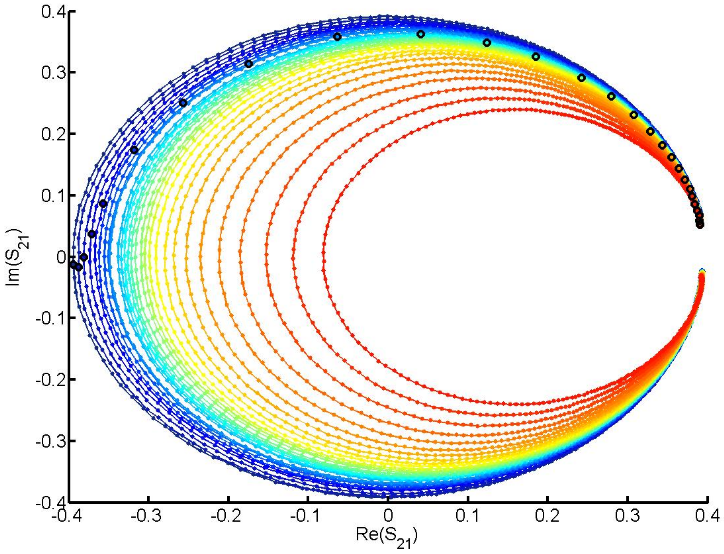

Figure 3.6: The resonance circles of a $s = 1\ \mu\text{m}$ NbTiN resonator as a function of temperature. The difference in temperature is indicated using the same colors as used in figure 3.5. The resonance circles are normalized to the lowest temperature circle measured $T = 320$ mK. The black circles indicate the location of the resonance frequency measured at $T = 320$ mK. As can be seen from these points an increase in the number of quasi-particles gives a response in both phase and amplitude.

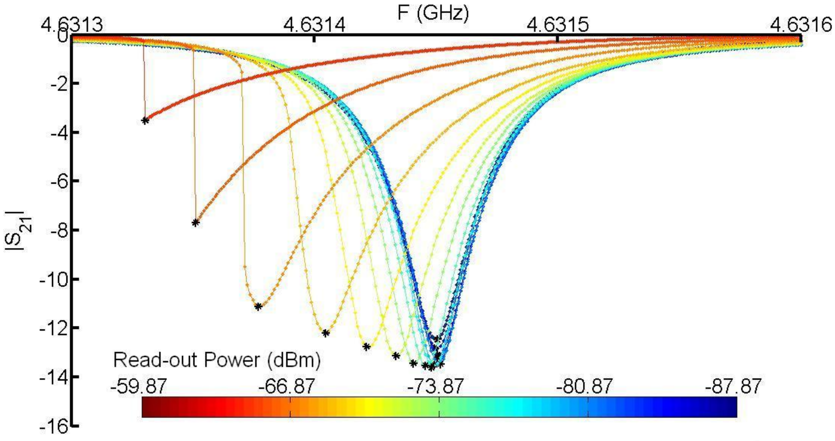

Figure 3.7: The feedline transmission near the resonance frequency of a $s = 1\ \mu\text{m}$ NbTiN resonator. As the read-out power is increased the resonator is slowly driven into non-linear behaviour.

by the geometry of the resonator, the maximum read-out power is limited by the central line width, s, and film thickness, t.

$$P_{read}^{max} \propto I_{max}^2 \propto (s \times t)^2 \tag{3.32}$$

3.5 Noise Sources in Superconducting Resonators

Like any alternative detector MKIDs also suffer from noise. The fundamental noise limits in a superconducting resonator are generation-recombation (GR) noise and Fano noise. However, in reality both in phase and amplitude read-out a different noise dominates. In phase read-out an excess noise was found that has been attributed to two-level systems (TLS) in the dielectrics at the surface of the superconducting film. In amplitude read-out the noise is usually dominated by the cryogenic amplifier. In this section each of these 4 noise sources will be discussed briefly.

3.5.1 Amplifier Noise

Conventional read-out systems for MKIDs use a high electron mobility transistor (HEMT) as a cryogenic amplifier. While this noise level of the HEMT is generally lower than the TLS noise, it is usually higher than GR noise and Fano Noise. This means the noise floor of the MKIDs read-out system is determined by the noise temperature of the HEMT amplifier, T_n^{HEMT}. This results in a frequency independent noise power spectral density (PSD):

$$S_x^{HEMT} = \frac{k_b T_n^{HEMT}}{r^2 P_{readout}} \tag{3.33}$$

x is used to show this is true for both amplitude, $x = A$, and phase, $x = \theta$, read-out.

3.5.2 Generation-Recombination Noise

In any superconductor, which is not cooled to $T = 0$ K, there will be a mean quasi-particle density, n_{qp}. However, this mean density is the result of a continuous generation and recombination (GR) of quasi-particles. This process can be described by Poissonian statistics. Because the GR fluctuations in n_{qp} can be larger than the change in n_{qp} due to absorbed light, thermal quasi-particle GR is a source of noise for MKIDs. The PSD of this GR noise is given by:

$$S_x^{GR}(\omega) = \frac{4N_{qp}\tau_{qp}}{1+\omega^2\tau_{qp}^2}\left(\frac{\delta x}{\delta N_{qp}}\right)^2 \tag{3.34}$$

3.5.3 Fano Noise

When a photon with an energy, $h\nu > 2\Delta$, is absorbed in a superconductor it can break a Cooper pair. However, if the energy is much larger than the energy gap it can break not just one, but many Cooper pairs.

$$N_{qp} = \frac{\eta h\nu}{\Delta} \tag{3.35}$$

Where η is the quasi-particle creation efficiency that has a typical value of 0.57 [48]. This gives MKIDs used for the optical, ultraviolet and X-ray detection an inherent energy resolution. But it also is an additional noise source, because this quasi-particle creation process is a stochastic one which obeys Poissonian-like statistics. The resulting PSD is given by:

$$S_x^F(\omega) = \frac{F\eta h\nu\tau_{qp}}{\Delta}\frac{1}{1+\omega^2\tau_{qp}^2}\left(\frac{\delta x}{\delta N_{qp}}\right)^2 \tag{3.36}$$

Where F is the Fano factor that has a typical value of 0.2. The reduced fluctuations compared to pure Poissonian statistics, which GR noise obeys, are due to electron-phonon interaction. These interactions create a strong correlation between the phonons and quasi-particles created from the energy of the original photon.

3.5.4 Two-Level System Noise

While GR noise was expected to be the fundamental noise limit of MKIDs experiments found an excess phase noise [56]. Based on experiments by Barends [6] and Gao [32] the hypothesis was formulated that this noise is caused by dipoles in the dielectric near the resonator. These dipoles will create fluctuation in the dielectric constant ϵ, which by means of the geometric capacitance results in frequency fluctuations.

$$\frac{\delta\omega_{res}}{\omega_{res}} = \frac{\alpha}{2}\frac{\delta\sigma_2}{\sigma_2} - \frac{F}{2}\frac{\delta\epsilon}{\epsilon} \tag{3.37}$$

These two-level system (TLS) fluctuators were found to be located on all the interfaces between the substrate, air and superconducting material. It was found by Gao [32] that increasing the width of the resonator decreases the TLS noise, because of the increased volume to surface ratio.

$$S_\theta^{TLS} \propto s^{-1.6} \tag{3.38}$$

Gao [32] also found that for a variety of superconducting metals and substrates the TLS showed the same dependence on the microwave power inside the resonator.

$$S_\theta^{TLS} \propto P_{int}^{-0.5} \tag{3.39}$$

This is assumed to be the result of a saturation effect that occurs it the TLS are exposed to a high electric field. Based on the two dependencies given above an empirical quantitative theory was developed that assumes the TLS noise contributions scale with the cube of the electric field, $|E|^3$ [32]. Near the open end of a resonator the electric fields are the highest. This makes it advisable to use a large coupler, even if the rest of the resonator is reduced to submicron widths.
Baselmans et al. [9] found that TLS noise also depends on the resonator quality factor.

$$S_\theta^{TLS} \propto Q_l \tag{3.40}$$

To reduce TLS noise it will be preferential to use a wide, low Q_l resonator that is read-out using a high microwave power. However, not all these things are favorable for the overall performance of the resonator, as will be shown in the next 2 sections. However, one of the main results by Barends [6] is that the presence of oxides significantly increases the TLS noise. Removing the SiO_x before deposition and using superconductors that are natural nitrides, like NbTiN, will reduce the TLS noise. The next step in reducing the TLS noise is to remove the substrate altogether [7].

3.6 Resonator Responsivity

Most of the sources of noise presented in the previous section are expected to increase in noise level if the resonator width is decreased.

While this would suggest making submicron resonators is not favorable for the NEP the responsivity of the resonators is expected to improve.

Therefore this section will focus on obtaining an expression for the amplitude responsivity, $\frac{dA}{dN_{qp}}$, and the phase responsivity, $\frac{d\theta}{dN_{qp}}$, in which all geometry dependent factors are clear. Note that the responsivity is a derivate to the change in the number of quasi-particle in the resonator, N_{qp}.

$$N_{qp} = n_{qp} \times V \tag{3.41}$$

Where V is the volume of the resonator, usually taken to be the volume of the CPWs central line, and n_{qp} is the quasi-particle density, which in thermal equilibrium is given by equation 3.7. Changes in this quasi-particle density will result in a change of the resonance frequency, because of a change in L_k through σ_2. Combining the equations in sections 3.1 and 3.3 it can be shown that

$$\frac{\delta\omega_{res}}{\omega_{res}} = \frac{f_{res}(T) - f_{res}(0)}{f_{res}(0)} = \frac{\alpha\beta}{4}\frac{\sigma_2(T) - \sigma_2(0)}{\sigma_2(0)} \tag{3.42}$$

If this result is substituted in equation 3.30 it can be shown that the phase responsivity is equal to

$$\frac{d\theta}{dN_{qp}} = \frac{-\alpha\beta Q_l}{4V\sigma_2(0)}\frac{d\sigma_2}{dn_{qp}} \tag{3.43}$$

As can be seen from equation 3.14 $\frac{1}{\sigma_2(0)}\frac{d\sigma_2}{dn_{qp}}$ is independent of the resonator geometry.
The amplitude of the resonance circle is changed due to a change in Q_i. Substituting equations 3.16 and 3.17 in equation 3.26 shows that

$$Q_i = \frac{2}{\alpha\beta}\frac{\sigma_2}{\sigma_1} \tag{3.44}$$

Quasi-particle creation will increase the losses in the resonator

$$\frac{d(1/Q_i)}{dN_{qp}} = \frac{\alpha\beta}{2V}\left(\frac{1}{\sigma_2}\frac{d\sigma_1}{dn_{qp}} - \frac{\sigma_1}{\sigma_2^2}\frac{d\sigma_2}{dn_{qp}}\right) \tag{3.45}$$

At the low operating temperatures of MKIDs $\sigma_2 \gg \sigma_1$. This means that of the last two terms $\frac{1}{\sigma_2}\frac{d\sigma_1}{dn_{qp}} \gg \frac{\sigma_1}{\sigma_2^2}\frac{d\sigma_2}{dn_{qp}}$. This is also shown in figure 3.8. Combining this information with equation 3.29 gives

$$\frac{dA}{dN_{qp}} = \frac{-\alpha\beta Q_l}{V\sigma_2(0)}\frac{d\sigma_1}{dn_{qp}} \tag{3.46}$$

3.7 Noise Equivalent Power

The main goal of this research is to reduce the noise equivalent power (NEP) of MKIDs by reducing their width. In this section it will be shown that from a theoretical point of view reducing the width of the resonators CPW will indeed lower the NEP. To simplify the analysis a constant ratio between s and w is assumed. The NEP in W Hz$^{-0.5}$ as function of the modulation frequency, $\omega = 2\pi f$, for a superconducting resonator is given by [56]:

$$NEP_x(\omega) = \sqrt{S_x(\omega, P_{int})}\frac{\Delta}{\eta\tau_{qp}}\left(\frac{\delta x}{\delta N_{qp}}\right)^{-1}\sqrt{1+\omega^2\tau_{qp}^2}\sqrt{1+\omega^2\tau_{res}^2} \tag{3.47}$$

Where $\tau_{res} = \frac{Q_l}{\pi f_{res}}$ is the resonator ring time. In the case of a very long quasi-particle lifetime this will limit the resonators response time. Therefore, it only appears in the last two terms: $\sqrt{1+\omega^2\tau_{qp}^2}$

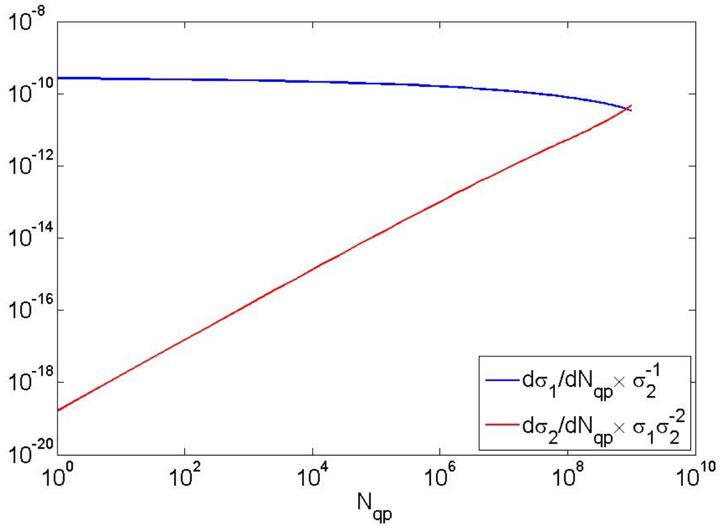

Figure 3.8: Numerical evaluation of the last terms of equation 3.44 using equations 3.7, 3.13 and 3.14. In the operating range of MKIDs, where the number of quasi-particles is low, $\sigma_2 \gg \sigma_1$. This makes the term containing the derivative of σ_1 dominant.

and $\sqrt{1+\omega^2\tau_{res}^2}$. These are present to describe the degrading performance at high frequency, but will for typical resonator parameters be between 1 and $\sqrt{2}$. The lowest value for the NEP is typically found at 1 kHz. Because the last 2 terms in equation 3.47 do not significantly depend on s they will be disregarded in the rest of this section. x is again used to show the equation can be applied to both amplitude, $x = A$, and phase, $x = \theta$, read-out.

As was shown in section 3.4 both amplitude and phase responsivity are proportional to [56]:

$$\frac{\delta x}{\delta N_{qp}} \propto \frac{\alpha Q_l}{V} \tag{3.48}$$

The volume, V, is off course directly proportional to s. The kinetic inductance fraction is difficult to capture in a pure power-law due to its inherent asymptotic behavior for $s \leq \lambda$ and $s \gg \lambda$ where α approaches 1 or 0, respectively. It can be shown that for $\alpha \propto s^\gamma$, γ is given by:

$$\gamma = \frac{d\alpha}{ds} \times \frac{s}{\alpha} \tag{3.49}$$

Using the theory presented in section 3.3.2 γ can be evaluated. Figure 3.9 shows γ for a 100 nm thick film using various magnetic penetration depths. It can be seen in figure 3.9 that for an aluminum detector with a central line of 600 (nm) $\gamma \approx -0.7$. However, for a similar resonator in a NbTiN film $\gamma \approx -0.15$. Gao [32] predicts a dependency of $\alpha \propto s^{-1.0}$ for a film thickness, $t > \lambda$. Figure 3.9 shows a convergence to $\gamma = -0.9$. As the initial prototypes for SAFARI will be using 600 (nm) central lines in aluminum a value of $\gamma = -0.7$ will be assumed for the rest of this section. This is the same as the value predicted by Porch et al. [72].

Contrary to the responsivity, amplitude and phase noise do have a different dependency on resonator width. Combining equations 3.32, 3.38, 3.39 and 3.40 it can be shown that the TLS dominated phase noise will have a width dependency equal to:

$$S_\theta \propto \frac{Q_l^2}{s \times s^{1.6}} \tag{3.50}$$

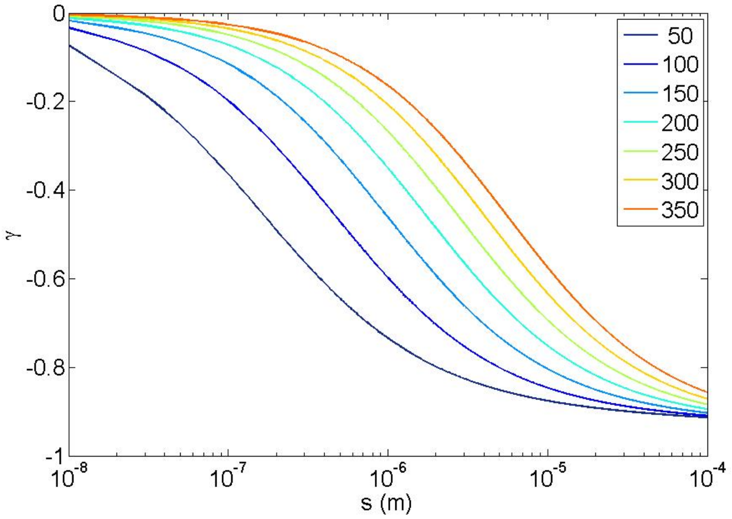

Figure 3.9: The power γ as a function of the width for 7 different magnetic penetration depths (nm). A film thickness of 100 nm has been assumed.

The amplitude noise is dominated by the HEMT. Therefore, this noise level will only depend on the used read-out power.

$$S_A \propto \frac{1}{P_{read}} \propto s^{-2} \tag{3.51}$$

Combining all the width dependencies of the noise and responsivity found above gives:

$$NEP_\theta \propto \sqrt{\frac{Q_l^2}{s^{2.6}}} \frac{s^{0.7} \times s}{Q_l} \propto s^{0.4} \tag{3.52}$$

$$NEP_A \propto \sqrt{\frac{1}{s^{2.0}}} \frac{s^{0.7} \times s}{Q_l} \propto \frac{s^{0.7}}{Q_l} \tag{3.53}$$

This means the NEP in both phase and amplitude read-out can be improved by using submicron resonators. In addition a high Q_l improves the NEP in amplitude read-out, which is the read-out method planned for SAFARI.

Chapter 4

Design and Fabrication of Submicron Resonators

The main advantage of MKIDs from a fabrication point of view is the fact that with a single layer process an entire array of pixels can be made. The basic principle of such a one layer lithographic process is illustrated in figure 4.1. After cleaning a wafer, or substrate (black), the desired superconductor (grey) is deposited onto it. This metal is then coated with a resist (dark blue) not unlike the coating of the old films used in photography. Exposure to light, or high energy electrons, breaks the polymers in the resist (cyan). This allows these exposed areas to be developed and removed. By controlling which regions are exposed any pattern can be made. To transfer this pattern to the superconducting film an etch is applied. This can either be a liquid chemical or a plasma. During the etch the unexposed resist will protect the metal, while the exposed metal is removed by the etch. After removing the unexposed resist the sample is ready for measurement.

Most structures made using nano-fabrication need to repeat these 6 steps multiple times to create a stack of metal and insulating layers. The Transition Edge Sensor (TES) of Morozov et al. [63] mentioned in chapter 1 needs at least 5 deposition and 3 etching steps. MKIDs, however, need to go through this process only once to pattern the 2 slots of the coplanar waveguides (CPWs) that form the superconducting resonators and feedline. For the current generation of MKIDs this pattern is defined using UV light, but this limits the slot widths to $\sim 1\ \mu\mathrm{m}$. To improve the sensitivity by reducing the width of the CPW, as shown in section 3.7, a new recipe has to be developed to make slot widths of a few hunderd nanometers.

In the following sections all individual steps of the lithographical process developed to make these narrow resonators are discussed in more detail. The fabrication of the samples was mostly done in the cleanroom facilities of the Van Leeuwenhoek Laboratory (VLL) using the equipment of the nanofacility (NAF) and physics of nano-electronics (PNE) group of the Kavli Institute of Nanoscience in Delft. The aluminum films were supplied by SRON. The deposition was done in the SRON cleanroom located in Utrecht. In this chapter multiple scanning electron microscopy (SEM) images are shown. These were made using the FEI Philips XL30S SEM in the general usage area of the NAF.

Appendix A contains a summary of the recipe developed in this thesis to fabricate submicron resonators.

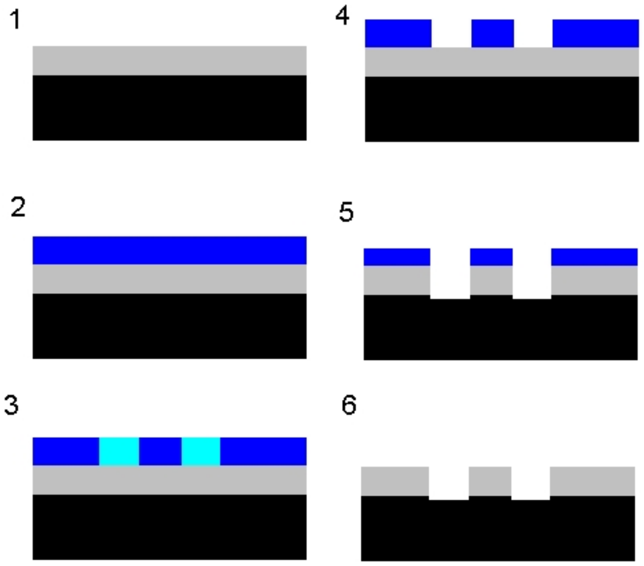

Figure 4.1: Illustration of a single layer nanofabrication process. After a metal (grey) is deposited on a substrate (black) (1), this metal is coated with a resist (dark blue) (2). This resist is then exposed to light or electrons at the location where the metal should be removed. In the exposed areas the resist is modified (cyan) (3). This modified resist can be developed and removed (4). To transfer the pattern in the resist to the metal, either a plasma or a wet etch is used to etch away the exposed metal (5). After removing the remaining resist the production of a single layer of the device is completed (6).

4.1 Material Choice

The superconducting materials used in this thesis are niobium titanium nitride (NbTiN) and aluminum (Al). NbTiN was used to investigate the resonator properties as a function of width. NbTiN was chosen for this because [6]:

- NbTiNs $T_c \approx 14$ K allows the measurements to be done in the MKIDs setup in Delft.
- Within the PNE-group there is a large amount of experience with and data of NbTiN resonators fabricated using optical lithography.
- NbTiN has a large magnetic penetration depth, $\lambda \approx 350$ nm. Based in the theory presented in chapter 3 it could be expected that additional effects arise when the width of the central line becomes of the order of λ.

The downside of NbTiN is the unmeasurable short quasi-particle lifetime, $\tau < 1$ μs [6]. This makes a proper calculation of the noise equivalent power (NEP) impossible. As a substrate HF-cleaned silicon wafers (350 μm, 1 kΩcm) have been used.

For the creation of a low noise detector aluminum is still the material of choice. Its high quasi-particle lifetime $\tau_{qp} \approx 2$ ms, low gap energy, $\Delta_0 \approx 0.17$ meV [10] and similar noise and Q compared to other materials make very low NEP possible. The low gap energy is also the disadvantage of aluminum. Since aluminum only has a T_c of 1.1 K it can only be measured in the setups of SRON, either the ADR in Utrecht or the dilution fridge in Groningen.

The preferred substrate below actual detectors is sapphire, c-plane in this case. While this substrate generally gives a slightly higher frequency noise than HF-cleaned silicon, it allows a higher internal power to give an overall better NEP [88]. However, for back-illuminated optical experiments there is a problem. Sapphire becomes opaque to radiation above 2 THz [36]. This is also true for regular, 1 $\mathrm{k\Omega cm}$, silicon [36]. This means that while optical experiments for the low frequency band of SAFARI can be done on sapphire, another wafer material is needed for bands 1 and 2. The material of choice for this is high-resistivity, 10 $\mathrm{k\Omega cm}$, silicon, which shows an order of magnitude less absorption in the THz regime [18].

4.2 Wafer Cleaning

Before deposition wafers are cleaned to remove any contaminations and oxides. It has been shown that these oxides at the metal-substrate interface are the main cause of TLS noise [6]. Silicon wafers used below NbTiN are first cleaned with an oxygen plasma in the Leybold Hereaus of the PNE-group using the settings given in table 4.3. This is typically done for 2 minutes. This exposes the $\mathrm{SiO_x}$ surface, which is then removed using an ammonium fluoride buffered solution of hydrofluoric acid (BHF, AF 87.5-12.5). At an etchrate of 12 $\mathrm{nm/min}$ removal of the natural oxide of silicon typically takes a minute. Over time the hydrogen passivated silicon bonds will become $\mathrm{SiO_x}$ again. This process takes place on a timescale of half a day. Therefore deposition is typically done within an hour after HF cleaning.

Since deposition of aluminum is done in the cleanroom of SRON in Utrecht the cleaning is done here as well. For silicon wafers this is done using Piranha, SC1 and diluted HF. The precise recipe is shown in table 4.1. To clean sapphire wafers they are submerged in Aqua Regia for 10 minutes at 100 °C. Because of the cleaning and hydrogen passivation no RF cleaning of the substrate is applied inside the deposition chamber before deposition of either metal.

4.3 Film Deposition

Both the aluminum and NbTiN films are deposited using DC magnetron sputtering. The NbTiN is deposited in the Nordiko-2000 of the PNE-group using a 99.8% pure $\mathrm{Nb_{0.7}Ti_{0.3}}$ target. Using a nitrogen flow this target is nitrodized during the deposition. The process for the reactive sputter deposition of NbTiN in the Nordiko was developed by Iossad [40]. The deposition parameters used in this research can be found in table 4.2.

Table 4.1: This table details the wafer cleaning procedure used at SRON in Utrecht before deposition of the aluminum film. After each step the wafer is rinsed in a beaker of ultra-pure water. The source chemicals used are H_2SO_4, H_2O_2, NH_4OH, HF and H_2O with concentrations of 95%, 30%, 25%, 5% and 100%, respectively.

	removal of	Mixture Type	Volume Ratio Mixture	Temperature	Clean time
1	Organic Contaminant	Piranha	$H_2SO_4 : H_2O_2$ 3:1	95 °C	10 min
2	Particles	SC-1	$NH_4OH : H_2O_2 : H_2O$ 1:1:5	70 °C	10 min
3	Surface Oxides & Hydrogen Passivation	Dilute HF	HF	20 °C	0.5 min

The aluminum is deposited in the SRON LLS 801 of the Unaxis Blazers company. The controls of this batch machine, which can hold up to 60 4” wafers, has been modified to allow use as a R&D machine. Like the Nordiko this machine has a load-lock to allow the main chamber to be constantly under vaccuum conditions, reducing oxidation and contamination. This is important to obtain a clean film from the 5N5 aluminum target. To improve the uniformity of the deposition the wafer is rotated on a drum oscillating over a 20 degree angle with a speed of 0.375 rot/min. Table 4.2 lists the parameters used during the deposition of aluminum in the LLS.

4.4 Electron Beam Lithography

Instead of optical lithography to expose the resist this project makes use of electron beam lithography (EBL) using the Leica EBPG 5000+ available at the VLL cleanroom facility. Instead of deep UV a beam of highly energetic electrons is used to expose the resist. Using the EBPG 5000+ any pattern drawn in a CAD program can be exposed onto the resist. This gives an increased flexibility over optical lithography for which mask plates have to be written. However, the main reason to use EBL in this research is the diffraction limit of optical lithography. This only allows structures down to approximately 1 $\mu\mathrm{m}$. In EBL it is the so-called proximity effect, which limits the resolution. The high energy primary electrons will hit the polymers in the resist in an inelastic collision. This will not only break the polymers, increasing their solubility in the developer, but it also generates secondary electrons. These secondary electrons can break more resist polymers and release more secondary electrons. However, the direction of travel of these secondary electrons will not be the same as the primary electrons. The secondary electrons create a region of typically 50 nm around the beam focus were the resist is exposed, even if the beam is focused in a smaller spot. While compensations for this effect can be made by exposing some areas with a lower dose of electrons, it does make leaving small structures near large exposed areas more difficult. Despite the proximity effect structures down to 5 nm have been fabricated [78].

A disadvantage of EBL compared to optical lithography is the throughput. A single beam of electrons is used point-by-point expose the desired pattern in a rectangular grid. In optical lithography a complete wafer can be exposed at once. In order to reduce the writing time beams with a different spot-size can be used to expose structures of different sizes. The pattern can be split into different layers, allowing each layer to be written with a different beam.

4.4.1 Electron Sensitive Resist

Before applying the resist to the wafer it is given a primer coating of HMDS spun at 4000 rpm for 1 min. The electron sensitive resist PMMA 950k, a 6% concentration solved in anisol, is then applied. This resist is spun on the wafer for 1 min at 1500 rpm to coat 100 nm NbTiN and at 4000 rpm to coat $\leq$ 100 nm Aluminum. The resulting resist thicknesses should be 600 nm and 300 nm, respectively. For both resist thicknesses a CPW slotwidth down to 200 nm can be fabricated. However, due to the

Table 4.2: This table details the parameters used in the Nordiko and LLS for the deposition of NbTiN and Al, respectively.

Machine	Target	Argon	N_2	DC Power	DC Voltage	Pressure	Deposition Rate
Nordiko	$Nb_{0.7}Ti_{0.3}$	100 sccm	4 sccm	300 W	300 V	8.0 μbar	53 nm/min
LLS	Al	113 sccm	–	876 W	357 V	6.7 μbar	30 nm/min

different etchrate of NbTiN and Al in the various plasmas more resist is required to protect the NbTiN during etching. After the primer and resist are spun on the wafer it is baked on a 175 °C hot plate for 15 min.

4.4.2 Intelligent Electronic Pattern Design

A very common pattern that needs to be exposed for this project are the 2 slots of the CPW geometry. In order to quickly vary the parameters of the desired resonators without redrawing the design in AutoCAD a Matlab routine was developed. Based on a large number of desired parameters, such as resonance frequency, Q_c and meander length, this program generates the coordinates required to describe a large number of polygons. Together these polygons describe the resonator, as shown in figure 4.2(a). In a similar way feedlines are generated. By varying the input parameters of the resonators and feedlines complete chips and wafers can be designed within minutes. If desired, different (parts of the) resonators or feedlines can be put in different layers, allowing exposure using different beams in the EBPG.

Using the CIF file format [87] the Matlab generated coordinates were read into the program LinkCAD. In this program the adjoining polygons were merged into a single polygon to decrease writing time. The resulting pattern, as seen in figure 4.2(b), was stored in a DXF file, which can be read and modified by AutoCAD, for final modifications, and by the LayoutBeamer software that generates the exposure patterns for the EBPG. Final modifications in AutoCAD usually included the addition of identifying text and the addition of patterns for DC measurement.

After the first test runs 2 problems in the EBL patterning showed up. They can be seen together in figure 4.3 where a Matlab generated pattern can be compared to the final result as seen in the SEM. The first problem is a vertical shift between 2 layers containing the micron and submicron CPW, given in red and blue in figure 4.3(a). In addition a horizontal shift between the 2 layers is present, which cannot be seen in this geometry. These shifts can be up to 1 μm and are found to vary between exposures. An easy solution to this problem is the creation of an overlap that takes all shifting directions into account. Because the dimensions of the CPW geometry are about the size of the shift this solution cannot be applied. Another location where these shift between layers causes a problem is at the coupler. If the feedline is written using a different beam than the resonators, the width of the ground plane between feedline and resonator is uncontrolled. This creates an unpredictable Q_c. This problem was resolved by writing all active structures, resonators and feedline, in a single layer using the smallest beam required for the job, which has a typical beam spot size of 30 nm. The price paid for this was an increase in writing time to typically 5 hours per 2” wafer. An alternative solution would be the use of alignment markers that are etched into the metal. However, this would create a second lithographical loop of exposure and etching for just these alignment markers. This means the advantage of the single layer process is gone. The use of markers could become viable during the fabrication of submicron material hybrid KIDs [27] or when bridging of the KIDs [49] is done. For these processes markers are required anyway.

The second problem can be seen at the edges connecting the 6 right most points in figure 4.3(a). Because the EBPG uses a rectangular grid to expose the pattern any line that is not horizontal, vertical or at a $45°$ slope will be discretized into a staircase pattern with the beam step size as a step height. This can be seen on the right most bit of the CPW in figure 4.3(b). This is especially clear in more narrow resonators, with 200 nm wide slots, that are written using a beam step size of 10 nm 4.6(a). Each of these steps will act as a scattering center for the traveling microwave reducing the resonator quality factor. This had been observed at SRON were resonators fabricated using optical lithography showed the same problem with a similar relative roughness scale compared to the slot width [88]. The most

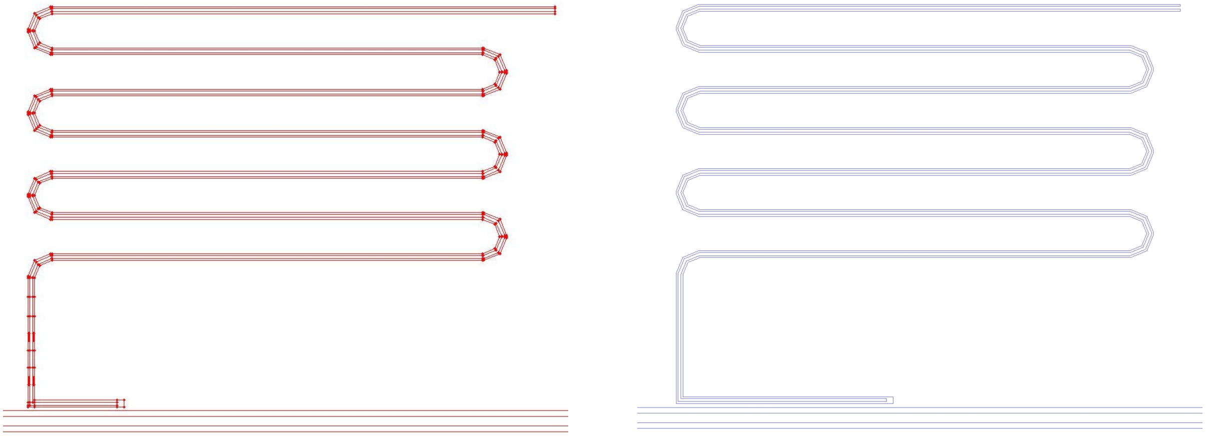

(a) Matlab Output

(b) LinkCAD Output

Figure 4.2: A resonator during 2 stages of the electronic design. Matlab generates the coordinates for basic polygon that together form the resonator. Adjoining polygons are merged into one using LinkCAD to improve the writing time. In these designs the new curves with a low number of sections per 180° can be seen.

likely cause is given by the fact that the mask plates were made using EBL. The technique developed at SRON to solve this problem was reflowing the DNQ/Novolak based optical resist by heating it for 30 s on a 135 °C hot plate after development [49]. Due to the critical time and temperature combination to get the right smoothing another solution was looked for instead of developing this process for PMMA. The electronic design was modified in such a way that bends used 2 or 4 sections per 180° instead of 30. This means the CPW edges are only along a line 0, 22.5, 45 or 90° from the horizontal direction of the exposure grid. In this redesign care had to be taken that the slot widths were kept the same in the bends as in the horizontal sections. The final design of bends using 4 sections per 180° used for the fabrication of submicron resonators can been seen in figure 4.2.

4.4.3 Development

After the PMMA has been exposed, using a typical dose of 1200 $\mu\mathrm{C\,cm^{-2}}$, it is developed using a 3:1 mixture of 2-propanol, IPA : MIBK, Methyl IsoButyl Ketone. The wafer is submerged in this solution vertically for 90 s. Immediately afterwards it is put vertically in IPA for 30 s to stop the development. The wafer is rinsed with IPA and blow dried to make sure no semi-developed resist remains. After optical inspection using polarization filters the decision can be made to add more time to the development.

4.5 Etching

4.5.1 Wet Etching

As a first experiment a wet etch of aluminum was tried. During a wet etch the wafer with metal and developed resist is submerged in a liquid chemical. This liquid is chosen in such a way that it will selectively react with the metal, removing it, while leaving the resist and substrate undamaged.

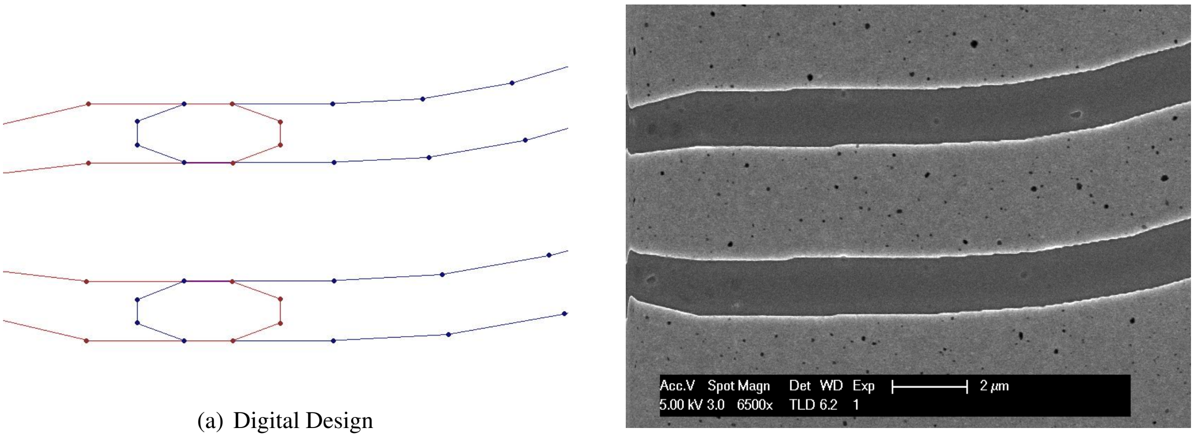

(a) Digital Design

(b) Fabrication Result

Figure 4.3: SEM images of a pieces of a resonator in aluminum showing the two problems due to the mode of operation of the EBPG. Figure (a) shows the digital design, which after fabrication resulted in figure (b). Both the vertical shift between the two layers, which are given in red and blue, and the rectangular grid used for exposure are visible.

To etch aluminum a recipe developed by SRON has been used. The following base chemicals were used: phosphoric acid (H_3PO_4, 85%), acetic acid (CH_3COOH, 100%), nitric acid (HNO_3, 65%) and distilled water (H_2O, 100%) in a volumetric mixture ratio of 16:1:1:2. The percentages given in the brackets are the concentrations of the source chemicals. In this mixture the aluminum is etched at a rate of approximately 40 $\mathrm{nm/min}$ at room temperature. However, the type of deposition, thickness of the oxide layer and previous processing steps can have a significant influence on the etch rate.
From SEM inspection, of which two examples are shown in figure 4.4, it was concluded that this was not the way forward for this project. The downside of wet etching is the fact that it is an isotropic process. Ass a result no resonator with a central line width smaller than 500 nm survived the etch. Furthermore, the three acids seemed to have flown below the PMMA resist in areas close to the slots. The size of these areas increased with the applied dose, pointing towards minor exposure caused by the proximity effect as the source of this allowed access.

4.5.2 Dry Etching using SF_6

In order to fabricate resonators with a central line width down to 100 nm reactive ion etching (RIE) was used instead of wet etching. The advantage of a dry etch over a wet etch is its anisotropy. This is exactly what is needed based on the results of the wet etch. In a reactive ion etch the substrate is placed on one of the plates of a capacitor. Under a low pressure a gas is then released, which is ionized by the low frequency RF signal applied to the capacitor. The radicals and ions of this plasma can then help the etching process in 2 ways. The first one is by means of physical etching. The ions are accelerated towards the substrate and can knock out atoms there. The second method is chemical etching. By choosing the right gas, the radicals can stick to the metal through adsorption and react with it. The product of this reaction can then leave the substrate by desorption and diffuse back into the main gas flow. By keeping the temperature low enough the ion bombardment, which stimulates the desorption, can be made the dominant factor in the desorption. Making also the reactive component of the etching anisotropic. The disadvantage of reactive ion etching is the fact that any material will be physically etched. This means the resist masking the metal needs to be thick enough to survive during the entire

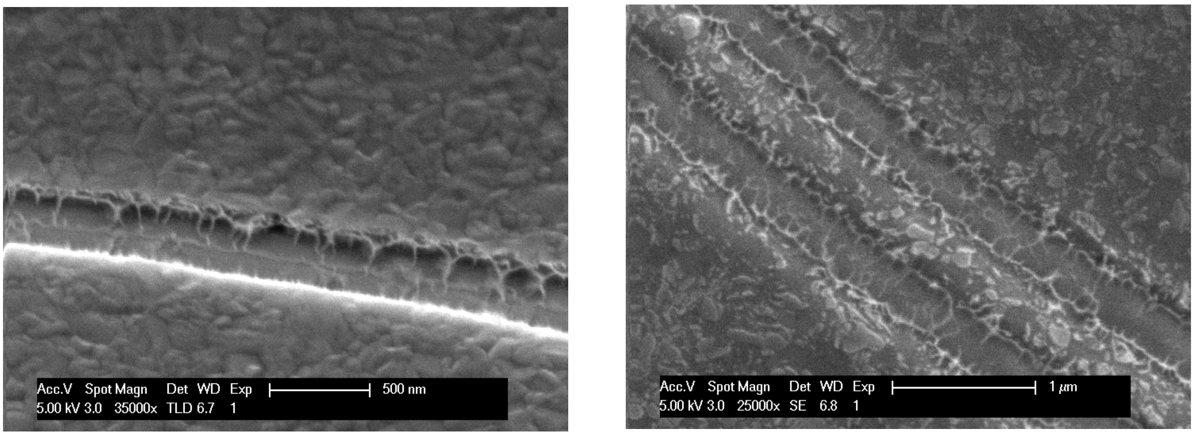

(a) The result of a triple acid wet etch applied to submicron resonators. The central line has almost been completely removed.

(b) A "regular" sized resonator after wetetching. While the resonator is still there the slots are not very clean and the film seems to be damaged.

Figure 4.4: SEM images of a wet etched aluminum.

etching. Also the etch has to be stopped in time to avoid overetching into the substrate.
To etch NbTiN a plasma of SF_6 and O_2 is used in the Leybold Hereaus Fluorine etcher of the PNE-group. The settings used can be found in table 4.3. While NbTiN is etched anisotropically very well in this plasma, this chemistry was originally developed for etching silicon. This means there is a significant risk of overetching. To control this laser endpoint detection was used. In this method the reflectivity of the surface is measured using a laser. Because the reflectivity of NbTiN is higher than silicon, the reflected power will drop when the silicon is exposed. For wafers up to 2 inch the etching is uniform enough to stop a few seconds after the reflectivity change, whilst maintaining a good balance between overetching and a clean etch.

4.5.3 Dry Etching using Chlorine

For aluminum SF_6 is not a suitable reactive chemical, thus a chlorine based plasma is used instead. This type of plasma is available in the Alcatel GIR300 in the general user area of the VLL. This machine is a reactive ion etcher as described in the previous section, except that it uses a plasma consisting of BCl_3, Cl_2 and N_2. While the two chlorine compounds react with the aluminum to form a volatile compound, the nitrogen creates aluminum nitride. This is, like aluminum oxide, extremely resilient against the reaction with chlorine. This creates an AlN_x sidewall in the slots that protects the underlying aluminum. Thus creating an even more anisotropic result. This anisotropy can be clearly seen in figure 4.6(a) where the 10 nm beam step size of the EBPG has been transferred to the metal. The resilience of aluminum oxide also means that, while aluminum is etched away very quickly, the

Table 4.3: This table details the parameters used in the Leybold Hereaus SF_6-etcher for oxygen plasma cleaning and the dry etch of NbTiN. During the etch of NbTiN the valve to the vaccuum pumps are left open for a pressure as low as possible.

	O_2	SF_6	Pressure	RF Power	RF Voltage
Oxygen Cleaning	25 MLN	0 MLN	0.230 mbar	20 W	100 V
NbTiN Etching	5 MLN	13.5 MLN	0.006 mbar	230 W	50 V

natural oxide needs to be removed by physical etching. A small variation in the thickness of this oxide can thus result in a variation of the time needed to etch the aluminum. This is why laser end-point detection is used again to determine when to stop the etch. When working on sapphire, Al_2O_3, one can overetch wafers significantly, because sapphire will not be etched by this plasma. When working on silicon more care should be taken, although it does not etch as quickly as in a SF_6 plasma. Overetching times of up to 20 s have been used without significant overetching into the silicon. The settings used on the Alcatel GIR3000 can be found in table 4.4.

Etching NbTiN using a Dry Chlorine Etch

While NbTiN can be etched anisotropically using a SF_6-plasma, it can be etched in a chlorine plasma using the same recipe used for aluminum. The advantage from a fabrication point of view is that NbTiN etches faster in a chlorine plasma with respect to PMMA and silicon than in a SF_6-plasma. This means a slightly thinner resist can be used, which allows smaller structures. It also allows a slightly longer overetching time, because chlorine does not etch silicon very rapidly. After etching the edges of the NbTiN also have a minor slope, as can be seen in figure 4.5(a), which is advantageous for the fabrication of NbTiN-Al hybrid resonators, because it improves step coverage. However, measurements have shown that resonator fabricated using a chlorine plasma generally have a lower internal quality factor than those made using an SF_6-plasma. The internal quality factor in a chlorine plasma usually is up to 500.000, while over 1 million has been shown in SF_6 [6]. The cause of this might be the sloped edges [32], but is more likely due to the material of which these edges are made. In figure 4.5(b) one can see the result of a resist shortage while etching NbTiN in a chlorine plasma. Due to the proximity effect of the EBL the resist of the central line of this coupler was partially exposed. During development most of the resist was removed. The plasma removed the remaining resist before the etch of the regular slots was complete. As can be seen the central line has been etched away, except for the edges. It is likely that these edges are a modified material, likely with an increased nitrogen content. Since most of the current is running in the edges this modified material is most likely the cause of the systematically lower quality factors.

4.6 Resist Removal

The final step of the one layer process is the removal of any remaining resist. The removal of PMMA was typically done by submerging the wafer vertically in hot, 50 °C acetone for 30 min. This beaker was then transferred to the ultrasonic bath. After 2 min of ultrasonic cleaning the wafer was rinsed with IPA and blown dry. Although this process removed most of the resist sometimes a thin film or spots remained. These could not be removed by repeating the process.
This is why a switch from acetone to PRS3000 was made. The wafer was again submerged vertically and the PRS3000 was heated to 70 °C for 30 min. After 2 min in the ultrasonic bath it was then rinsed in acetone and IPA and blown dry. This process did generally clean the wafer completely. Because the

Table 4.4: This table details the parameters used in the Alcatel GIR300 chlorine based etcher. The typical time to etch through 100 nm of aluminum is 2.5 min. This recipe can also be used for etching NbTiN. A typical etch time for 100 nm NbTiN is 4 min.

BCl_3	Cl_2	N_2	Pressure	RF Power
15 sccm	7.5 sccm	10 sccm	0.0100 mbar	50 W

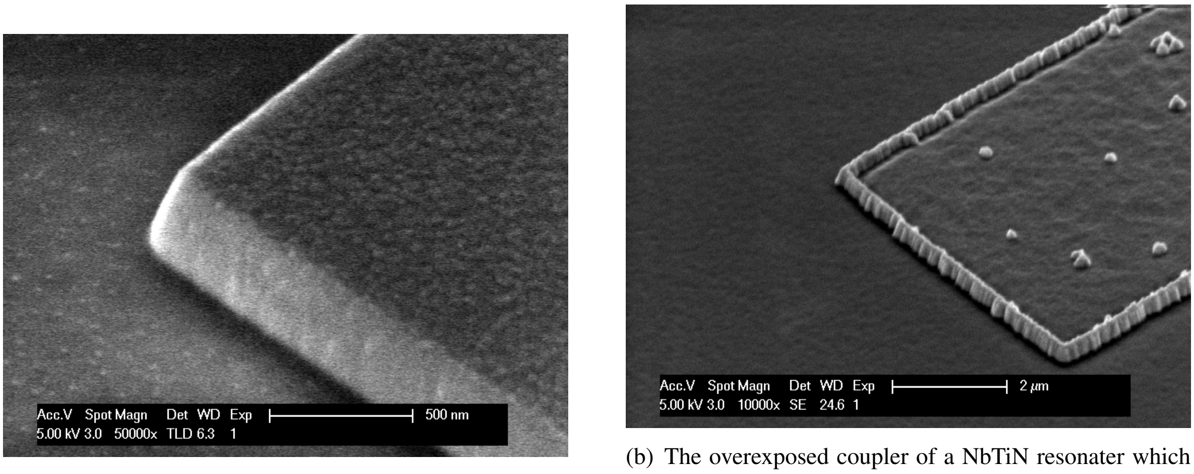

(a) The corner of a NbTiN resonator etched using a dry chlorine-based etch. From this image the slightly slope of the walls is clearly visible.

(b) The overexposed coupler of a NbTiN resonater which was etched using the chlorine dry etch. Only the edges of modified NbTiN are remaining as the central line was etched away after the resist ran out. The edges are clearly more resilient against the plasma.

Figure 4.5: SEM images of NbTiN films etched in a chlorine plasma.

wafer after cleaning is again covered in PMMA to protect during dicing, the application of PRS3000 was only done when this second coating needed to be removed. The application of PRS3000 was only used once, because of the possible etching behavior of PRS3000 against aluminum [3].
This hypothesis was tested when one wafer showed, after chlorine etching and acetone cleaning, ribbon-like structures in the SEM. These ribbons, as seen in figure 4.6(b), are a carbon-chlorine compound, which is known to form occasionally during the use of PMMA in a chlorine plasma [26]. The exact conditions under which this compound forms are unclear and they were, luckily, only observed once during this research. Due to the importance of the batch 2 duplicate chips were used to test cleaning of these ribbons. The first chip was cleaned using the above PRS3000 recipe except with a 45 min heating time. This has no effect on both the ribbons and the aluminum. The chip was then left room temperature PRS3000 overnight, approximately 15 hours. From SEM inspection it was found this had not damaged either the aluminum or the contaminating ribbons.
The second chip was exposed to an oxygen plasma in the Leybold Hereaus SF_6-etcher. The plasma used an oxygen flowrate of 25 MLN, 0.150 mbar of pressure and was driven using 50 W of power resulting in a 270 V potential. The sample was exposed to this plasma first for 30 s and a second time for 5 min. After the second exposure minor damage could be observed to the ribbons. A much longer exposure, possibly on the order of an hour, would be required to remove the ribbons completely. Not only would this damage the aluminum due to physical etching, this plasma is also an ideal condition for the creation of aluminum oxide [27]. Oxides that are known to be the cause of TLS noise in these superconducting resonators.

4.7 Final Fabrication Results

Combining the fabrication methods described in this chapter submicron resonators can be made. The key aspects are the use of EBL with an intelligent pattern design and RIE. This recipe, of which a cookbook style version can be found in appendix A, allows fabrication of resonators with slots down to 200 nm in both Al and NbTiN. Adjusting e-beam resist thickness allows film thicknesses up to 300

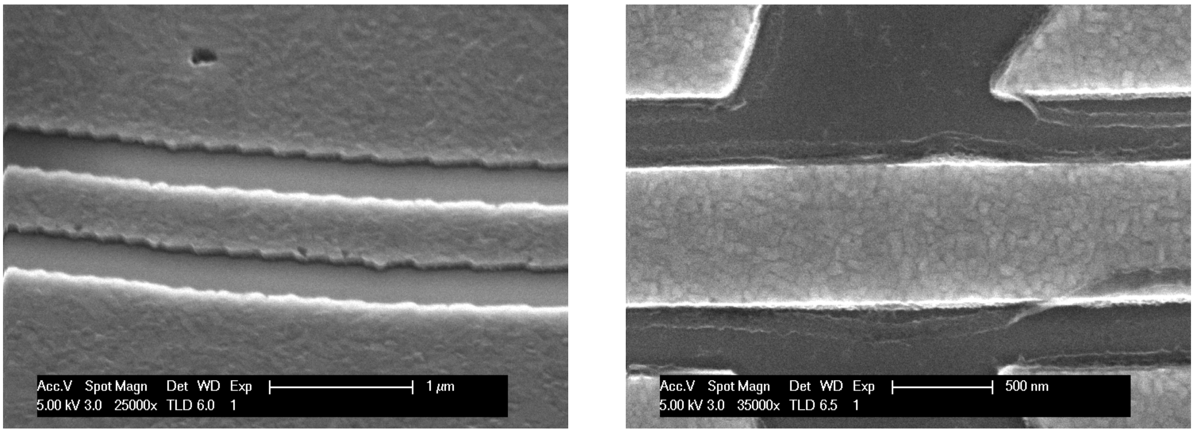

(a) A curved CPW section with 200 nm slots. The edge is roughened as the rectangular EBPG grid of 10 nm steps is transfered in the metal. This shows the anisotropy of dry etching, but damage the resonator quality.

(b) Ribbons of a carbon-chlorine compound created during the RIE using a Chlorine plasma while using PMMA as a mask. The exact conditions of their formation or effects on the resonator performance are unknown.

Figure 4.6: SEM images of RIE results of aluminum.

nm even in NbTiN. Figure 4.7 shows 2 SEM images of submicron resonators fabricated in this way. A possible improvement to the recipe is the use of a lower temperature and shorter time to bake the PMMA resist before exposure. While NbTiN films and sapphire substrates do not seem to be affected by these high temperatures, it could be the cause of the very low quality resonators in a aluminum on HF-cleaned Si substrate. These chips were found to have very low Q resonators and dips which only show a resonator-like response at temperatures below 100 mK. Although T_c has not been measured this might be an indication of a modified T_c compared to pure aluminum. The hypothesis is that the high temperatures could cause the silicon to diffuse into the aluminum, dramatically changing its properties. This should mean that when sapphire or $\mathrm{SiN_x}$ is used as a substrate there is no problem. However, this aluminum on silicon batch also had the ribbons of modified PMMA on it, as described in the previous section. These ribbons could also be the cause of the unusual behavior. A last possibility could be that the high temperatures change the aluminum itself regardless of the substrate. However, measurement of aluminum on C-plane sapphire chips do not support this hypothesis. They are baked at the same high temperatures as the aluminum on silicon, but show no indication of a decrease in performance.

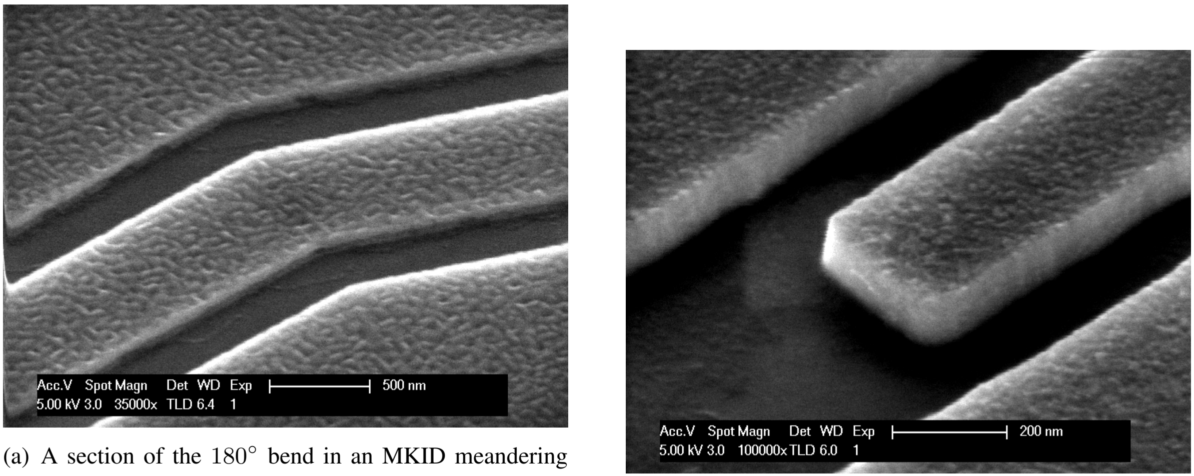

(a) A section of the 180° bend in an MKID meandering through a 100 nm aluminum film. A central line of 700 nm and slots of 350 nm were used to match the line through the 6.3 THz planar antenna for SPICA B1 shown in figure 3.1(b).

(b) The open end of a submicron resonator in 100 nm NbTiN. The central line is 300 nm and the slots 200 nm.

Figure 4.7: SEM images of resonators fabricated using the recipe in this chapter.

Chapter 5

Properties of a Superconducting Resonator as a Function of Width

5.1 Measurement Chip Design

As shown in section 3.7 the noise equivalent power (NEP) of a superconducting resonator can be improved by reducing the width of the coplanar waveguide (CPW). This has, however, never been experimentally shown for widths below the “standard” 3 $\mu\mathrm{m}$. Therefore, a chip, labeled RJ11V2C6, was fabricated using the techniques developed in chapter 4. This chip contained 5 sets of 2 resonators with a layout similar to the one shown in figure 1.2(a). Each set had a different central line width varying between 0.3 $\mu\mathrm{m}$, which is the smallest dimensions that could be achieved reliably by the fabrication process, and 3 $\mu\mathrm{m}$, which is the central line width commonly used in literature [6, 56]. For all these resonators a ratio of $s/w = 3/2$ was used. The exact design values of f_{res}, Q_c, s and w for these 10 resonators are listed in table 5.1.

These 10 resonators were patterned in a 100 nm NbTiN film on a 1 $\mathrm{k\Omega cm}$ silicon substrate. NbTiN was chosen, for its higher T_c compared to aluminum. This allowed measurements in the Delft KIDs setup, which can only reach temperatures down to 310 mK. Using this setup the transmission dips and noise of the resonators on RJ11V2C6 were measured as a function of temperature and power. The width dependences of the kinetic inductance fraction, quality factor, responsivity, optimum read-out power and noise that were derived from these measurements are presented in this chapter.

5.2 TU Delft Measurement Setup

The KID setup at the TU Delft, most of which has been built by Barends [6], is based on a HDL-8 cryostat from Infrared Laboratories, Inc. with a He-3 sorption cooler. The setup has a base temperature of 310 mK. This is well below $0.1T_c$ for NbTiN. The cryogenic system is completely integrated with the microwave setup needed to measure the transmission dips of the KIDs on a 20 by 4 mm sample.

5.2.1 Cryostat

After the HDL-8 cryostat has been pumped vacuum, liquid nitrogen and liquid helium are used to cool the system to 77 and 4.2 K, respectively. The cold plate and all parts connected to it, shown in figure 5.1(a), are kept at this temperature by the tank of liquid helium below it. To increase the lifetime of the liquid helium it is surrounded by a shield kept at 77 K using liquid nitrogen. Mounted on the

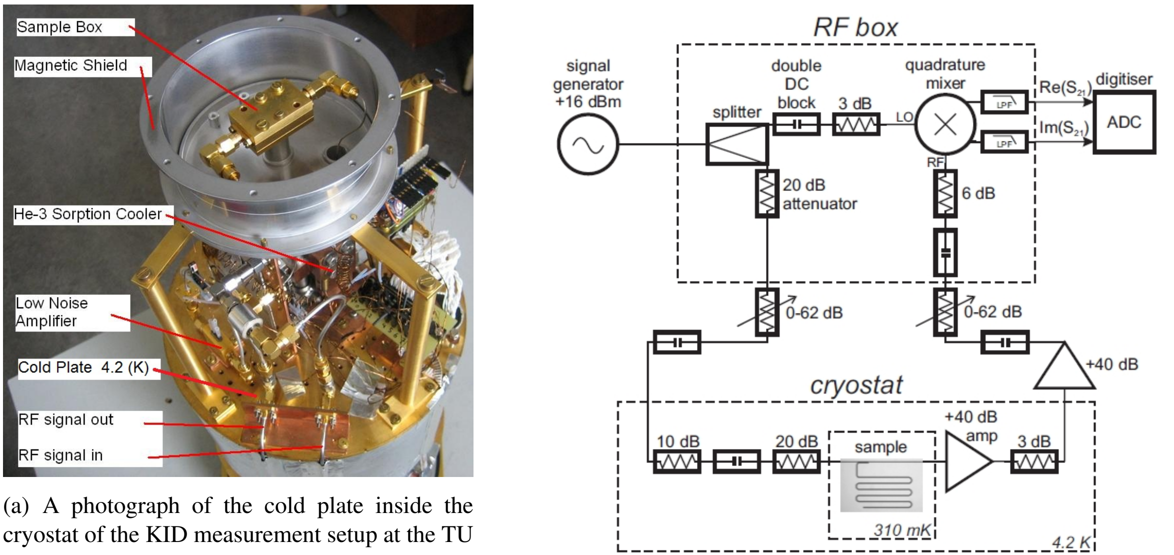

(a) A photograph of the cold plate inside the cryostat of the KID measurement setup at the TU Delft. Indicated are some key components like the sorption cooler and the low noise cryogenic amplifier.

(b) A block diagram of the RF setup in the KID measurement setup at the TU Delft.

Figure 5.1: A photo of the cryostat (a) and a schematic overview of the electronics (b) used for KID measurements at the TU Delft. Both images were taken from Barends [6].

coldplate is a two-stage He-3 sorption cooler that makes it possible to reach a base temperature of 310 mK. In the sorption cooler He-3 is contained within a porous material. By heating this material the helium is desorbed. The released helium is liquefied as it passes a condenser that is kept cold using the second stage of the sorption cooler. The liquid helium-3 fills a bath connected to the sample stage. When all of the helium-3 is desorbed, the heater of the porous material is turned off. This allows the material to start absorbing the He-3 gas again, lowering the vapor pressure in the chamber. This lowered pressure will cause the liquid He-3 to evaporate and cool the sample stage to 310 mK. By controlling the heating of the porous material the vapor pressure in the sorbtion chamber can be set, which ultimately determines the temperature of the sample stage. Through this chain the temperature of the sample can be set to a value between the base temperature and 4.2 K. To reach temperatures above this value direct heating is applied.
The second stage of the sorption cooler is another sorption cycle as described before. However this second stage uses helium-4 instead of helium-3 and instead of the sample it cools the condenser of the first stage. The second stage condenser is connected to the cold plate to liquefy the He-4.

5.2.2 Microwave Setup

After the sample has been cooled to the desired temperature, measurements of the microwave transmission can be done. For this purpose an RF setup, schematically shown in figure 5.1(b), is integrated in the cryostat. A signal generator provides a microwave signal, which is split in two. The first part of the signal is, after a number of attenuators, led into the cryostat by SMA cables. Inside the cryostat these cables are connected to the nitrogen shield and cold plate. Attenuators are used to suppress the thermal radiation from outside the cryostat. The signal is then carried to the gold-plated copper sample box, in which a 20 by 4 mm chip is glued using GE varnish. The sample is electrically connected using Al-Si (1% Si) wire bonds. To ensure a well-defined ground plane wire bonds between the sample box and ground plane are made on all sides of the chip, and not just between the CPW on the holder and CPW on the narrow side of the chip. Special care has to be taken to keep the CPW feedline on the chip approximately 50 Ω in order to avoid reflections or the creation of standing waves. After the signal has passed the sample and its transmission has been modified by the resonators on the chip, it returns to the cold plate through SMA cables. Here the signal is amplified using a High Electron Mobility Transistor (HEMT). This cryogenic low noise amplifier (LNA) amplifies this signal by approximately 40 dB before it is lead out off the cryostat. At room temperature another 40 dB amplifier amplifies the signal before it is returned to the RF box. Here the signal is mixed using a quadrature mixer with the second part of the original signal. The mixer returns the real and imaginairy parts of the transmission, which are registered by a measurement computered using an ADC. Between the RF box and the cryostat a variable attenuator is places in the line to and the line from the cryostat. By varying the attenuation towards the cryostat a read-out power dependent measurement of the transmission can be done. The attenuator in the line towards the RF box is used to keep the signal in a power range where the IQ-mixer is linear. The total attennuation is kept constant to simplify the data analysis.

Instead of the RF box a Vector Netwerk Analyser (VNA) can be used to measure the transmission. In this setup the signal generator is used to stabilize the frequency generator inside the VNA. While the VNA is significantly faster in reading a single sweep of the resonator transmission, S_{21}, its sampling rate per point is too slow to perform noise measurements up to frequencies of 1 MHz. Therefore the VNA is used for the characterization of the resonator transmission as a function of power and temperature, while the IQ-mixer is used to measure the noise performance.

Before the actual measurements both systems, the VNA and the IQ-mixer, are calibrated for any remaining standing waves and other non-uniformities in the transmission as a function of microwave frequency. One example of a non-uniformity in the transmission is the strongly reduced amplification of the LNA outside the 2 to 8 GHz frequency band. These offsets are corrected by subtracting the system transmission measured at a significant fraction of T_c, typically 9 K for NbTiN. At this temperature the transmission dips of the resonators disappear and allow an unperturbed measurement of the largely temperature independent box resonances and system transmission. The measurement must be done below T_c, where theoretically the resonator dips are still present, because of the sharp increase of the resistance above the critical temperature.

5.3 Measurement Results

After cooling down the sample to liquid helium temperatures the sample was heated, first to 8 K for calibration and then to 15 K. During this second heating the average transmission of a broadband 4 to 6 GHz microwave signal was measured as a function of temperature. A similar measurement was also done as the sample cooled back to 4.2 K. Using this measurement, the transition temperature was determined to be 13.7 K, which is typical for NbTiN.

The sample was then cooled to 310 mK were it was found that 8 of the 10 resonators behaved as a normal quarter-wave (QW) resonator. One 3 μm central line resonator was not found. In addition one of the smallest 0.3 μm central line resonators was found at frequencies corresponding to its half-wave (HW) resonating mode, suggesting a broken central line close to the shorted end. Of this half-wave the first overtone was found and investigated in detail as well, as the transmission dip of this overtone was originally believed to be one of the largest resonators. The first overtone of the other narrowest resonator was investigated in detail as well. However, the motivation for this was the low base resonance frequency of $f_{res}^{meas} = 1.7925$ GHz, which is outside the ideal operating range of the LNA. A summary of the measured f_{res} and Q_c of each resonator can be found in table 5.1. In this table the measured overtones are given as well. The overtones are labeled x.5, where x is the base resonance.

5.3.1 Kinetic Induction Fraction

As can be seen in table 5.1 there is a large difference between the measured and designed resonance frequency. This occurred because in the design the kinetic inductance of the resonators is not taken into account. Using equation 3.23 the kinetic inductance fraction of the resonators can be estimated using the designed and measured resonance frequency. The results are shown in figure 5.2 as a function of the resonator central line width (red). It is clear that the kinetic inductance fraction increases rapidly as the width decreases.

However, Gao [32] has shown that the error in this estimate of α increases as the value of α itself decreases. A constant accuracy on the value of α can be achieved by looking at the kinetic inductance of a resonator relative to the narrowest resonator on the chip. The ratio of the kinetic inductance fraction of 2 resonators can be determined from the difference in their frequency shift as a function of temperature. As temperature increases thermal fluctuations will break an increasing number of Cooper pairs, increasing the kinetic inductance. This in contrast to the geometric inductance that is largely temperature independent. The increase in temperature will still increase the total inductance and thus the resonance frequency will shift downwards. This effect becomes stronger as α increases, because the resonator is more dependent on the kinetic inductance. This effect is shown in figure 5.3. Figure 5.3 shows the frequency shift as a function of temperature for the 5 different resonator widths of the measured chip. Because the increased temperature changes the complex conductivity in the film uniformly, it can be seen from equation 3.42 that dividing 2 of these $f_{res}(T)$-traces, of resonators i and j, will give the kinetic inductance ratio between these resonators.

$$\left(\frac{\delta f_{res}(T)}{f_{res}(0)}\right)_i \left(\frac{\delta f_{res}(T)}{f_{res}(0)}\right)_j^{-1} = \frac{\alpha_i}{\alpha_j} \tag{5.1}$$

Table 5.1: The designed, ^{des}, and measured, ^{meas}, parameters of the 10 resonators on chip RJ11V2C6 used for the investigation of the properties as a function of width. Resonator 9 was not found at all and resonator 2 was found to operate in the half-wave mode. Of the smaller resonators the first overtone was investigated as well. This is labeled as number x.5, where x is number of the base resonance dip.

Number	f_{res}^{des} (GHz)	f_{res}^{meas} (GHz)	s (μm)	w (μm)	$10^{-3} \times Q_c^{des}$	$10^{-3} \times Q_c^{meas}$
1	6.0	1.7925	0.30	0.20	50	1070
1.5	18.0	5.3741	0.30	0.20	–	332
2	6.2	3.8356	0.30	0.20	250	34
2.5	12.4	7.6613	0.30	0.20	–	11
3	6.6	2.6736	0.60	0.40	50	101
4	6.8	2.7727	0.60	0.40	250	610
5	7.2	3.5795	1.00	0.60	50	106
6	7.4	3.6985	1.00	0.60	250	463
7	7.8	4.6314	1.50	1.00	50	75
8	8.0	4.7686	1.50	1.00	250	331
9	8.4	–	3.00	2.00	50	–
10	8.6	6.1819	3.00	2.00	250	284

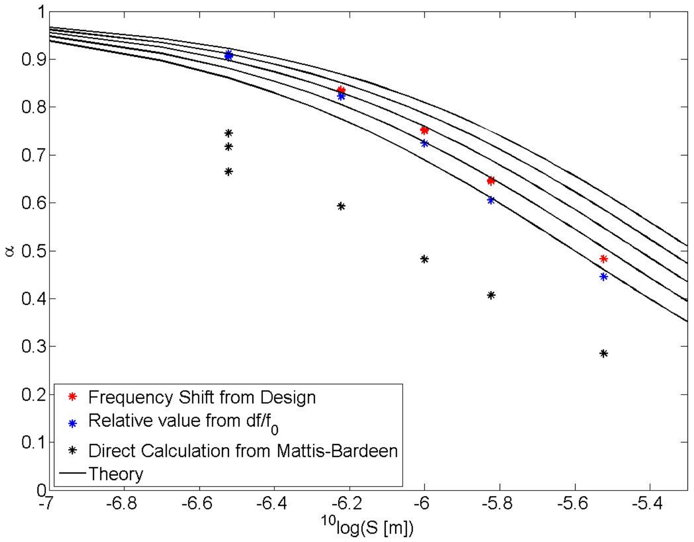

Figure 5.2: The kinetic inductance fraction, α, as a function of their central line width, s. Both the value inferred from the frequency shift compared to design (red) and relative value determination using the $f_{res}(T)$ dependency (blue) is shown. The black lines show theoretical estimated based on the theory presented in section 3.3.2. Between the 5 lines the magnetic penetration depth is varied between $\lambda = 350$ nm (top line) and $\lambda = 250$ nm (bottom line) is steps of 25 nm. α determined directly from equation 3.42 are shown using black stars. While this method shows the same trend as the other two, all values are a significant underestimation.

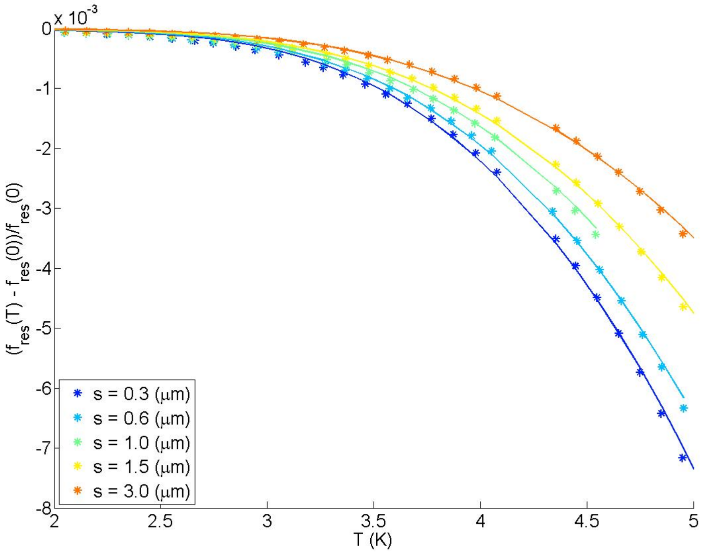

Figure 5.3: The change in resonance frequency as a function of temperature for resonators of 5 different widths. The dots are measured values, while the lines are a fit for α based on theoretical calculation of the values for $\sigma_2(T)$.

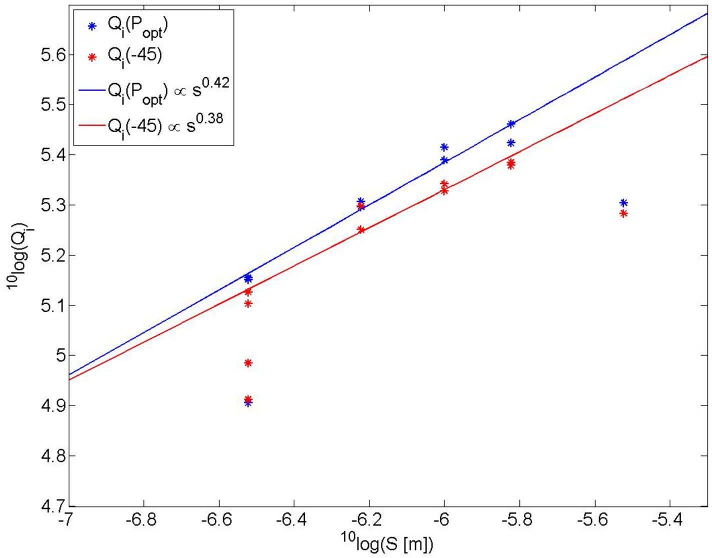

Figure 5.4: Internal quality factor as a function of central line width. Both the value at optimum resonator power (blue) and constant internal power (red) are shown. A fit (lines) through the points following the clear trend line shows a width dependency of $s^{0.4}$

This method was applied using $\alpha = 0.91$, as found for resonance 1, as a reference. The results can be seen in figure 5.2.
A third method to determine α is based on equation 3.42. Using the T_c, T and $f_{res}^{meas}(T)$ of each measurement point equation 3.8 and the integrals for σ_1 and σ_2 derived by Mattis and Bardeen [54] were evaluated in a Matlab code developed by de Visser [20]. A linear fit could then be made between 2 and 5 K to obtain α from equation 3.42. The values obtained this way can be seen in black stars in figure 5.2. While the general trend is the same as for the other estimations there is a large offset.
Using the theory presented in section 3.3.2 the black lines in figure 5.2 can be generated. Using the known geometry of the resonator the only unknown variable is the magnetic penetration depth. λ is varied between 350 and 250 nm in steps of 25 nm between the top and bottom line. A magnetic penetration depth of $\lambda \approx 275$ nm seems to be consistent with the data. This is lower than the value, $\lambda \approx 350$ nm, typically found by Barends [6], but corresponds closely to a rough estimate of 270 nm found using equation 3.9 when a $\rho = 100\ \mu\Omega\mathrm{cm}$ [40] is assumed.

5.3.2 Internal Quality Factor

Besides the kinetic inductance fraction and the volume it is the quality factor that influences the responsivity of the resonator. While in phase read-out this quality factor dependence cancels out in the NEP, SAFARI will use amplitude read-out. This means a high Q will improve the NEP. In figure 5.4 the internal quality factor of the resonators can be seen as a function of central line width. Both the Q_i at the optimum read-out power for each resonator (blue) and at constant $P_{int} = -45$ dBm (red) are given. The first is more interesting from a detector point of view. The latter removes any power dependency of Q_i making it more interesting from a physics point of view. Both show a dependency on central line width, which can be described as a power-law. This is shown by the solid lines. It

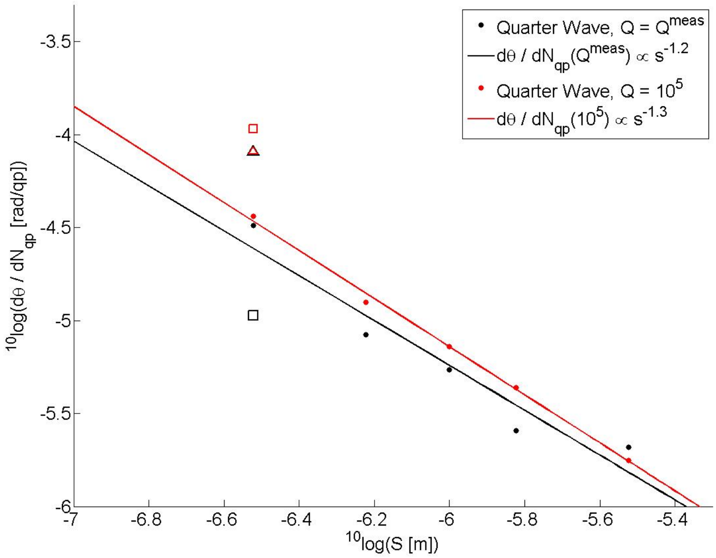

Figure 5.5: The phase responsivity of 7 resonances as a function of width. The different symbols indicated different resonance modes: dots for QW, squares for HW and triangles for the overtone of the QW. The half wave resonance is due to its low Q_c most influenced by the application of a constant $Q_l = 10^5$ to all resonators (red), compared to the use of the measured value of the resonators Q_l^{meas} (black). Changing to a constant value for Q_l changes the width dependence from $\frac{\delta\theta}{\delta N_{qp}} \propto s^{-1.2}$ (black line) to $\frac{\delta\theta}{\delta N_{qp}} \propto s^{-1.3}$ (red line).

is shown that $Q_i(P_{opt}) \propto s^{0.424\pm0.029}$ and $Q_i(-45) \propto s^{0.380\pm0.036}$. For these fits the two 300 nm resonators with a $Q_i < 100000$ have been ignored. The same is true for the 3 μm resonator. This Q_i is most likely lowered due to aluminum contamination from the bonding wires. When Q_i is investigated as a function of T it jumps at 1.2 K, the T_c of aluminum.

The cause of the width dependency of Q_i is unclear. The slopes of both fits are not significantly different, suggesting a power independent phenomena. Radiative losses, due to an increased dominance of the CPW odd-mode, are also not a candidate. Radiative losses are expected to increase as resonators become wider, following $Q_{rad} \propto (Z_0 s^2)^{-1}$ [85].

5.3.3 Responsivity

Now each component of the responsivity, α, Q_l and volume, has been looked at individually, the responsivity itself can be investigated. From the measured resonance circle the change in amplitude and phase can be determined as a function of temperature. The resonance circle at base temperature is set as a reference with radius unity and $\theta = 0$ at f_{res}. In this method the phase will reach a value close to π at $T = T_c/6$. This makes a direct determination of θ above these temperatures impossible. However, using equation 3.7 and a typical resonator volume of 5×10^{-16} m^3 it can be found that only at $T \approx T_c/6$ there will be 1 quasi-particle in the resonator. Any phase change at lower temperatures are mainly caused by small variations in the dielectric constant.

Therefore we adopt the method of Baselmans et al. [9] to determine the phase responsivity of each resonator. This method uses the the frequency shift as a function of the number of quasi-particles in

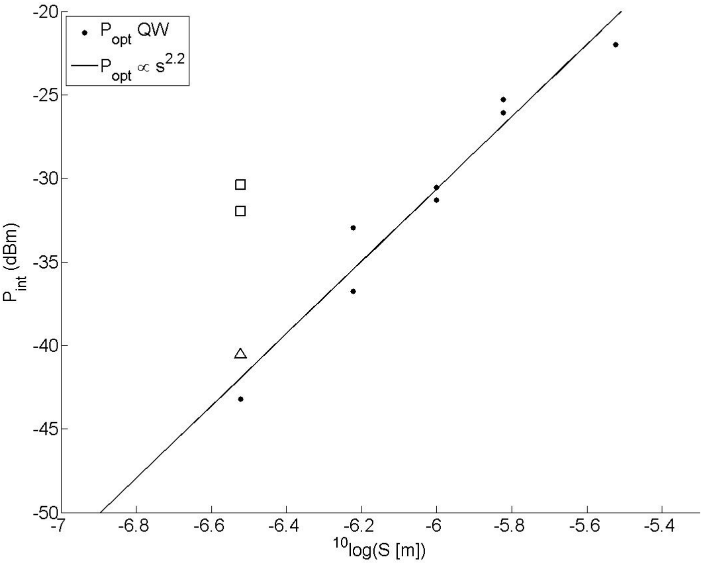

Figure 5.6: The internal power of each resonator at the optimum read-out power as a function of central line width. A distinction has been made between the quarter-wave (dots), half-wave (squares) and the first overtone of the quarter-wave (triangle) resonances. For the quarter-wave resonators the internal power depends on width as $P_{int} \propto s^{2.16\pm0.20}$.

the resonator to obtain the responsivity.

$$\frac{\delta\theta}{\delta N_{qp}} = -4Q_l\frac{\delta x}{\delta N_{qp}} \tag{5.2}$$

The fit to determine $\frac{\delta x}{\delta N_{qp}}$, where $x = (f_{res}(T) - f_{res}(0))/f_{res}(0)$, is applied at $T > T_c/6$. This is possible, because in the frequency domain the 2π redundancy is removed and working above $T_c/6$ makes this method less sensitive to changes in the dielectric constant.

Figure 5.5 shows that the phase responsivity increases for decreasing widths. Using only the quarter-wave mode resonances, this dependency can be described by a power law $\frac{\delta\theta}{\delta N_{qp}} \propto s^{-1.20\pm0.19}$. The scatter in figure 5.5 is not only caused by measurement uncertainty, but also by the variation in Q_c, because the responsivity depends on the loaded $Q_l = Q_l(Q_i, Q_c)$. To remove this dependency all responsivities have also been determined using a $Q_l = 1e5$, as shown by the red dots in figure 5.5. Only resonance 2.5 is influenced since it had only a $Q_c = 11e3$. Application of a constant Q_l changes the slope of the least-square fit to $\frac{\delta\theta}{\delta N_{qp}} \propto s^{-1.29\pm0.04}$.

Because of similar problems in the resonance circle a direct measurement of the amplitude responsivity is not possible. As shown by Baselmans et al. [9] this can be done reliably using the amplitude response to an optical pulse. These measurements are typically used to determined the quasi-particle lifetime of a film from the decay time of the response. The quasi-particle lifetime of NbTiN is so short that this decay cannot be measured. Hence, it is impossible to get a valid estimation of the amplitude responsivity.

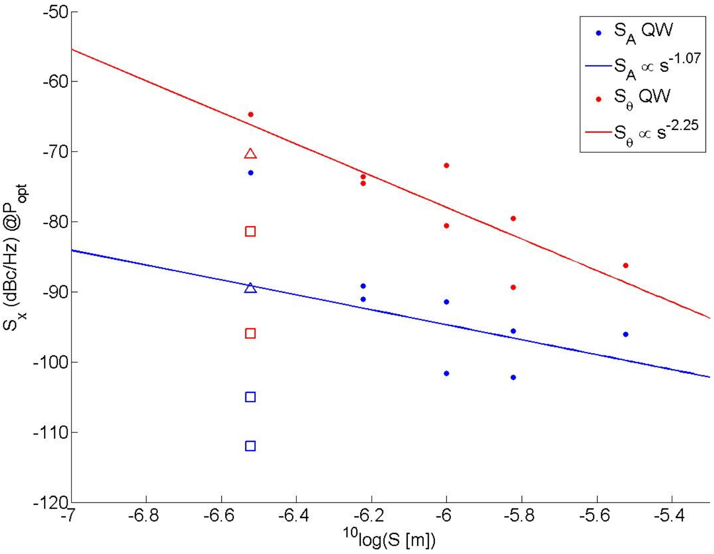

Figure 5.7: The 1 kHz amplitude (red) and phase (blue) noise of each resonator measured at the optimum read-out power. The quarter-wave resonances are indicated by the dots, while the squares indicate half-wave resonances and the triangle the first overtone of the quarter-wave. The power law found by least-square fit analysis of the is shown as a solid line.

5.3.4 Power Handling

Before investigating the noise, the maximum power that can be used to read each resonator is investigated. The optimum read-out power is determined using the level of the amplitude noise between 10 and 100 Hz. When the read-out power is lowered the noise fluctuations of the HEMT amplifier increase. This means the amplitude noise decreases with increasing power. However, overdriving the resonator creates and additional 1/f-noise. This increases the low frequency amplitude noise. Thus an optimum can be found. The method used to find this optimum start with the visual inspection of the resonance circles and dips and flagging any resonances showing non-linear behavior. The resonance dip of the second highest unflagged power is then set as reference. Any power with its resonance frequency within $df = f_{res}^{ref}/(6Q^{ref})$ of f_{res}^{ref} is considered a candidate for the optimum power. Of all candidates the power with the lowest mean amplitude noise between 10 and 100 Hz is chosen as the optimum power.
Using equation 3.31 the optimum read-out power is converted to optimum internal power. The measurement setup does this automatically, but it assumes $Z_{feedline} = Z_{res}$. While both the resonator impedance, Z_{res}, and feedline impedance, $Z_{feedline}$, are geometrically designed to be 50 Ohm, the resonators kinetic inductance can change the resonators impedance significantly. This means that the actual internal power is

$$P_{int} = \sqrt{1-\alpha} P_{int}^{meas} \tag{5.3}$$

Figure 5.6 shows the optimum internal power for each resonance as a function of width. Using only the QW resonances (dots) a dependency on width can found to be $P_{int} \propto s^{2.16 \pm 0.20}$.

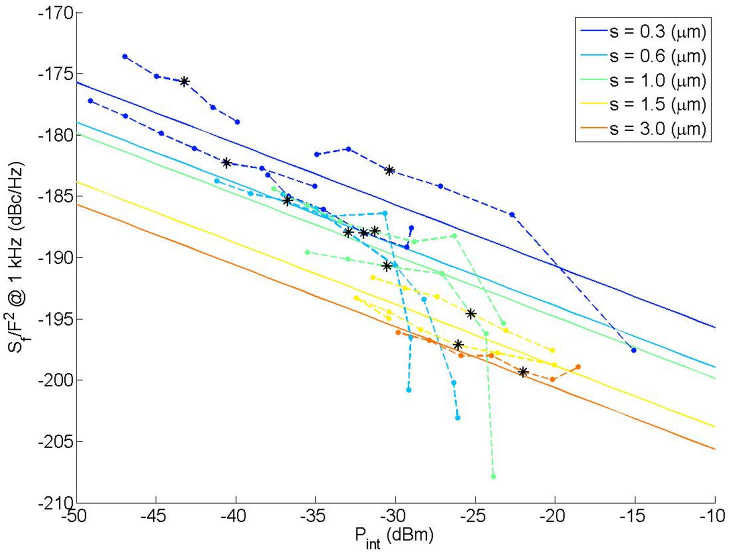

Figure 5.8: The frequency noise at 1 kHz as a function of internal power for each of the 11 resonances. The dashed-dotted lines show the measured values, with a black star indicating the optimum read-out power. The solid lines show a $P_{int}^{-0.5}$ dependence that is expected for TLS noise. For each width, indicated by a different color, these lines are shifted to match all points of that width that were not overdriven.

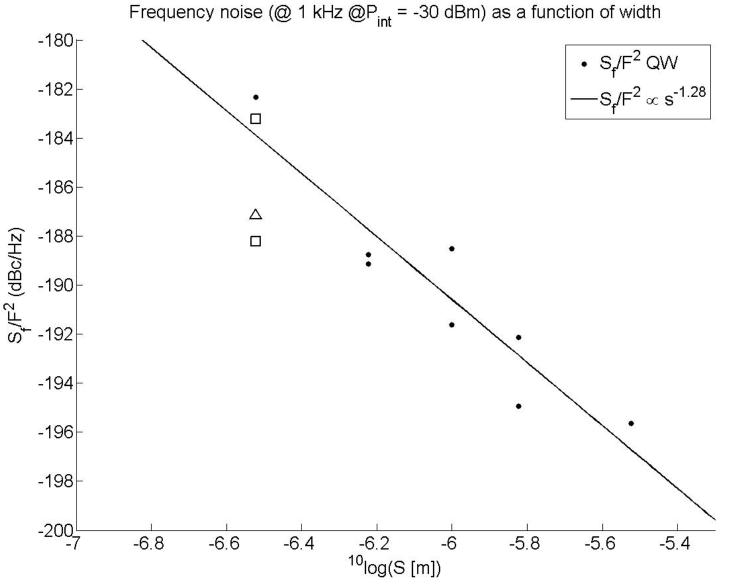

Figure 5.9: The 1 kHz frequency noise of every resonator measured at -30 dBm of internal power. The quarter wave resonances are indicated by the dots, while the squares indicate HW resonances and the triangle the first overtone of the quarter-wave. The power law found by least-square fit analysis is shown as a solid line.

5.3.5 Noise

Together with the responsivity, the power spectral density (PSD) of the noise forms the NEP. The noise level of resonators with different widths is shown in figure 5.7. For each resonance the 1 kHz value of the PSD, measured at optimum read-out power, is shown. Both the amplitude (red) and phase (blue) noise are shown. The latter clearly has a higher noise level due to the TLS noise, while the amplitude noise is limited by the system. Ignoring the QW resonance near 1.7 GHz a width dependence of $S_A \propto s^{-1.07\pm0.80}$ is found for the amplitude noise. The resonance below 2 GHz is ignored, because outside the range between 2 and 7 GHz the LNA is significantly more noisy. A noise temperature of $T_n \approx 100$ K is measured for resonator 1, compared to a typical value of 20 K between 2 and 7 GHz. The noise PSD of resonator 1 shows that at 1 kHz the TLS noise still dominates the noise in phase read-out. Hence this resonance is not ignored when investigating the width dependence of the phase noise, which is determined to be $S_\theta \propto s^{-2.25\pm0.54}$.

In order to confirm that TLS are still the dominant noise source in phase read-out, the frequency noise $S_f/F^2 = S_{theta} \times (4Q_l)^{-2}$ is investigated, where F is the resonance frequency of the resonator. The advantage of using the frequency noise is that it is independent from Q_l. Figure 5.8 shows the frequency noise at 1 (kHz) of all 11 resonances as a function of internal power. The stars indicate the optimum read-out power of each resonance and the colors indicate the width of the resonator generating this resonance. Literature has shown that TLS noise creates a characteristic $S_f/F^2 \propto P_{int}^{-0.5}$ power dependence [32, 6]. For each width a line of this slope is shown in figure 5.6. The offset is determined by minimizing the distance between the line and noise levels of resonances below optimum read-out power. It can be seen that the power-law characteristic for TLS noise is followed by all resonances.

Because of this power dependence a constant internal power level, $P_{int} = -30$ dBm, is chosen to compare the frequency noise between different resonances. Figure 5.9 shows the frequency noise as a function of the different widths. Taking into account only the QW resonances a width dependency of $S_f/F^2 \propto s^{-1.28\pm0.21}$ is found.

5.4 "Noise Equivalent Power"

Because the quasi-particle lifetime of NbTiN cannot be measured no real NEP can be determined for the resonators. However, since τ_{qp} and Δ can be assumed uniform over the entire film, thus equal for all resonator, a partial NEP can be determined to compare the performance of each resonator width.

$$\mathrm{NEP}^2(\omega) = (S_x(\omega)) \left(\frac{\delta x}{\delta N_{qp}}\right)^{-2} \left(1+\omega^2\tau_{res}^2\right) \tag{5.4}$$

Since only the phase responsivity, $\frac{\delta\theta}{\delta N_{qp}}$ has been determined, the amplitude responsivity is estimated using the phase responsivity and the relation expected based on the theory of Mattis-Bardeen [32], $\frac{\delta A}{\delta N_{qp}} = 0.26\frac{\delta\theta}{\delta N_{qp}}$. While Baselmans et al. [9] has shown this is not fully correct it is a reasonable first estimate. The resulting "NEP" at optimum read-out power for the 5 widths is shown in figure 5.10. As can be seen from the figure NEP in phase read-out is hardly influenced by the width. This is in accordance with the width dependencies of the noise and responsivity found in this chapter.

$$NEP_\theta \propto \sqrt{S_\theta}/\frac{d\theta}{dN_{qp}} \propto \sqrt{s^{-2.25}}s^{1.29} \propto s^{0.16\pm0.31} \tag{5.5}$$

Despite the fact that the increased TLS noise is less than expected from previous work, $S_f/F^2 \propto s^{-1.6}$ [32], the increasing phase noise cannot be compensated by the increased responsivity. The

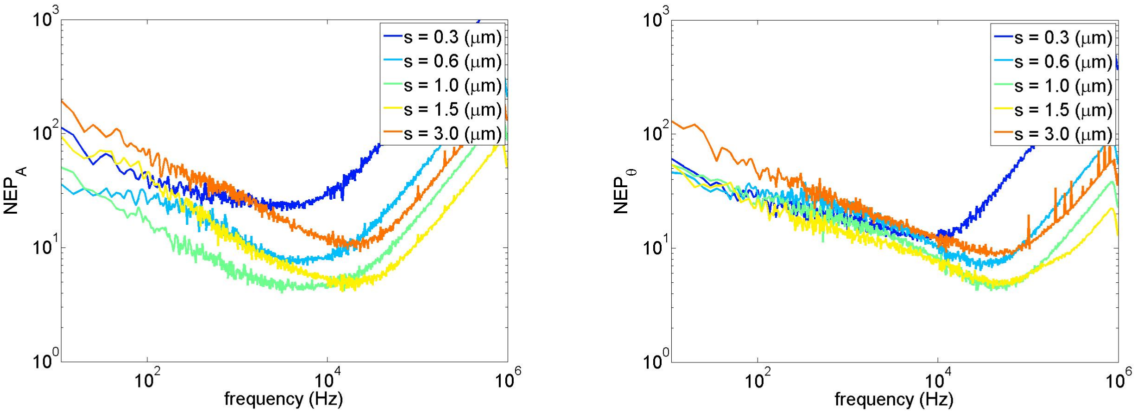

(a) Amplitude NEP

(b) Phase NEP

Figure 5.10: Noise Equivalent Power, as far as can be calculated, from the NbTiN resonators. While the phase read-out shows no clear improvement, amplitude read-out seems to have an optimum at $s = 1.00\ \mu\mathrm{m}$

width dependence of the responsivity, $s^{-1.3}$ is found to match the dependency on volume and kinetic inductance fraction perfectly. The trend found in Q_i is largely migitated by the scatter in Q_c. This can also be seen from the fact there is no significant difference between the width dependencies of the responsivity in the case of a constant or actual Q value.

Assuming that NbTiN follows the theory of Mattis and Bardeen [54] closely enough that amplitude and phase responsivity have an equivalent width dependency it can be shown that the amplitude NEP will improve as width decreases.

$$NEP_A \propto \sqrt{S_A} / \frac{\theta}{dN_{qp}} \propto \sqrt{s^{-2.16}} s^{1.29} \propto s^{0.21 \pm 0.11} \tag{5.6}$$

The level of the amplitude noise is completely dominated by the power handling capabilities of the resonators. Using $S_A \propto \sqrt{P_{int}}$ shows that the width dependencies of internal power, $s^{2.16}$, and amplitude noise, $s^{1.07}$, match perfectly. The power handling of these resonators also is consistent with the expected dependency based on geometrical arguments found in section 3.7.

The improved NEP for amplitude read-out is given in figure 5.10(a). However, an optimum occurs at $s = 1.0\ \mu\mathrm{m}$. It will require further investigation to see if this is a true or accidental optimum. The unfortunate resonance frequency of the 300 nm resonator outside the HEMT range increases the NEP by approximately one order of magnitude. Taking this into account would put the NEP of this narrowest resonator at the same level as the $s = 1.0\ \mu\mathrm{m}$ resonator. However, no such explanation can be found for the for the 600 nm wide resonator. This would support the existence of a real optimum $s < 1.0\ \mu\mathrm{m}$, which is most likely due to the decreasing improvement of the kinetic inductance.

Chapter 6

Submicron MKID Pixels for SAFARI

In the previous chapter it was shown experimentally that the noise equivalent power (NEP) can be reduced by reducing the width of the resonator if amplitude read-out is used. Because the SAFARI detectors will be operated in this read-out mode the submicron resonators can be incorporated in the detector design for SAFARI. First a test chip was made with hybrid resonators, which had a width that is partially submicron and partially micron sized. Using the experience gained from this chip a fully submicron resonator design was then made. This design was used to make a 9×8 pixel array. Both these chip designs were fabricated in aluminum and measured in the KIDs setup at SRON Utrecht. In this chapter the results of these measurements will be compared to "regular" aluminum resonators to see if the new designs for SAFARI have an improved sensitivity.

6.1 SRON Measurement Setup

The use of aluminum means the KID measurement setup in Delft as described in section 5.2 cannot be used. In order to reach a temperature below $0.1T_c$ a system is required that reaches 100 mK. Therefore the measurements of these aluminum pixels were done using the KID measurement setup at SRON Utrecht. This setup is very similar to that in Delft, especially from an RF point of view. The main difference is the cooling mechanism. Instead of liquid nitrogen, liquid helium and dual stage sobtion cooler, a Vericold GMHB dual stage Adiabatic Demagnetization Refrigerator (ADR) mounted inside a pulse tube cooler is used to cool the detector. The pulse tube first cools the system, reaching a cold plate temperature of approximately 3.5 K. This cold plate, along with the cold components of the RF setup can be seen in figure 6.1(a).

Cooling below this cold plate temperature is done using the ADR. An ADR cools by means of a paramagnetic salt pill. This pill is exposed to a high magnetic field aligning all the magnetic spins inside. When all spins are aligned, the magnetic field is turned off allowing the spins to randomize again. This randomization requires energy as the paramagnetic material has it disorders the material, increasing entropy. This means the surroundings of the pill is cooled as thermal energy is extracted from it to randomize the spins. In this dual stage ADR a ferric ammonium alum (FAA) salt pill and gadolinium gallium garnet (GGG) crystal are used as the diamagnetic pills. The GGG crystal first cools the system to 700 mK after which the FAA salt pill can cool it further to 50 mK. The temperature of this system can be controlled by applying a current to the superconducting magnet near the FAA salt pill. The weak magnetic field created this way will re-align the magnetic spins. This releases energy heating the detector.

Because of the magnetic fields involved the sample is located inside a superconducting magnetic shield

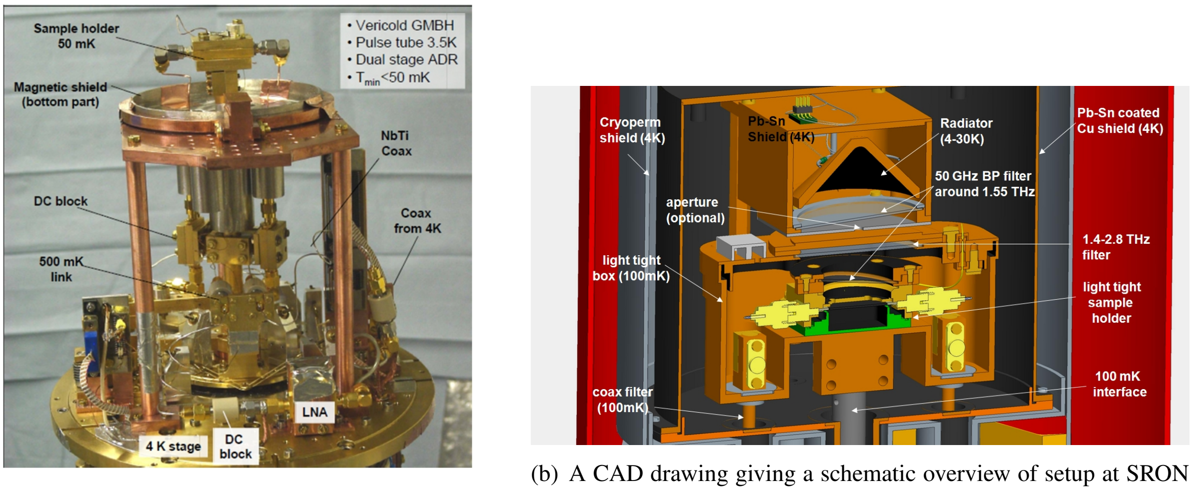

(a) A photograph of the cold plate in the pulse tube cooler of the measurement setup at SRON Utrecht. The bottom of the superconducting magnetic shield can be seen. In this image the box-in-box setup and other changes to improve the light tightness of the are not present.

(b) A CAD drawing giving a schematic overview of setup at SRON Utrecht inside the magnetic shielding. Two light tight boxes and coax filters are used to reduce stray light, while a blackbody is present for optical testing.

Figure 6.1: A photo and CAD drawing giving an overview of the inside of the cryostat used in the KID measurement setup at SRON Utrecht.

in the form of a lead-tin plated copper box. This is in turn located in a cryoperm magnetic shield. The low transition temperature of aluminum also means it has a very small band gap. This means it will be influence by any photons with a frequency above 90 GHz, making it a lot more sensitive to stray light than NbTiN. To remove stray light photons at the sample 2 measures were taken. First coax filter were applied to prevent light, particularly from the cold plate stage, traveling down the cables to reach the aluminum film. The second measure was the application of mounting the detector in a box-in-box setup. The already light-tight chip holder is mounted inside a light tight lead-tin coated copper box. A CAD drawing of this setup can be seen in figure 6.1(b). In this figure also a blackbody radiator can be seen. This can be used to investigate the optical properties of the detector for radiation at 1.55 THz, which corresponds to band 3 of SAFARI.

6.2 Width Hybrid Pixels

6.2.1 Hybrid Design

The first chip measured with a realistic pixel design for SAFARI B1 was a 100 nm aluminum on C-plane sapphire chip containing 11 quarterwave resonators with a hybrid-width design. This design, as shown in figure 6.2, had for the biggest part of the resonator, about 80%, a central line width of $S = 3.04$ μm. To reduce the TLS-noise, a wider "444-coupler" was used. In this coupler design S, W and V are all equal to 4 μm. For the final 20% of the resonators length near the shorted end, which is expected to be the most sensitive part of the KID, the central line width was reduced to $S = 0.66$ μm. In the center of this section a scaled version the orignal X-slot antenna as described in section 3.1 was patterned. It is scaled to a center frequency of 6.7 THz to match SAFARI B1. Except for the coupler the resonator CPW had a ratio $S/W = 2$. The full length of the resonator was meandered

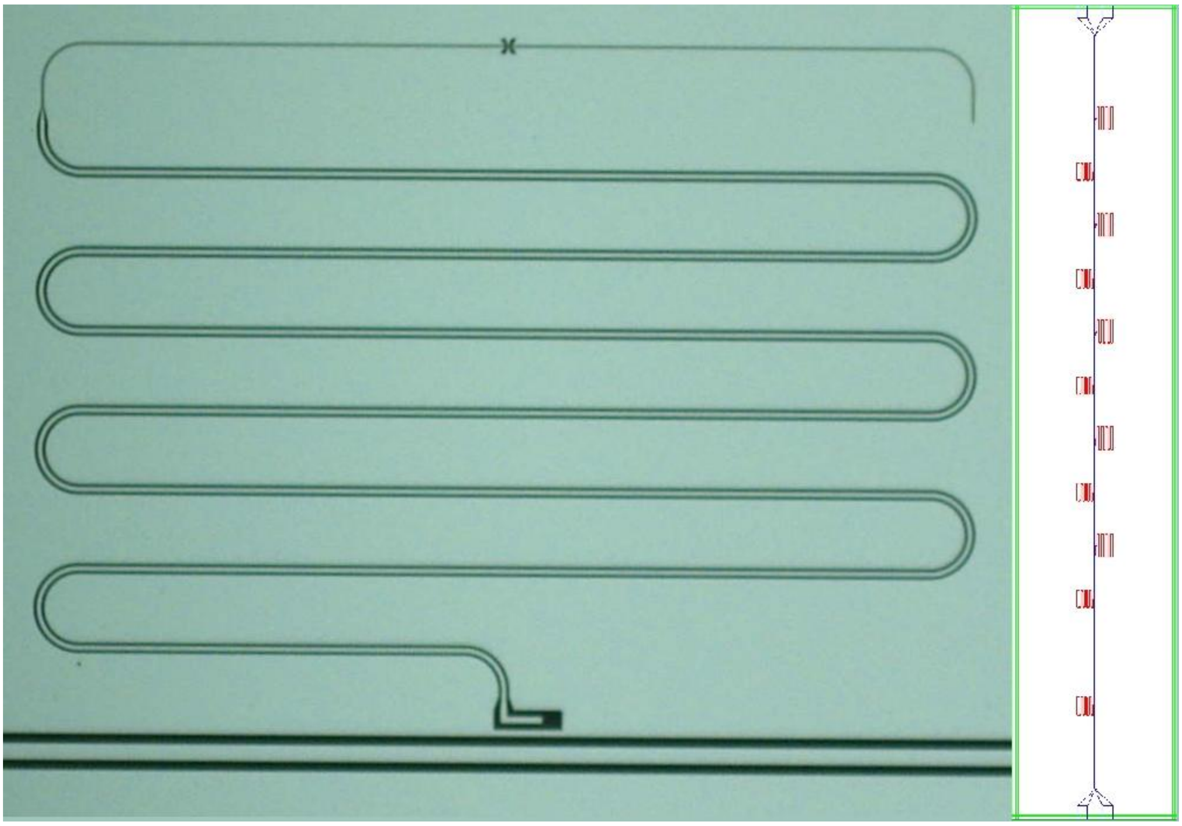

Figure 6.2: A photo taken under an optical microscope of the width-hybrid design as patterned in the aluminum. The top meander, which is the most sensitive part of the KID, is made submicron and contains the X-slot antenna scaled to SAFARI B1 frequencies. To the right is a CAD design showing the full 20x4 (mm) chip containing 11 of these resonators.

using 4 section bends in such a way that it fitted within the 480 by 480 $\mu\mathrm{m}$ footprint of a SAFARI B1 pixel.
On the measured chip, labeled “RJ4 SPICA pixeltest 22_5”, 11 of these resonators were present. By varying the length of the coupler 2 sets of Q_c were achieved, where $Q_c = 35\mathrm{k}, 60\mathrm{k}, 100\mathrm{k}, 500\mathrm{k}, 1\mathrm{M}, 3\mathrm{M}$. One of these sets was designed to have a base frequency of 8 GHz and one at 6 GHz increasing by 0.1 GHz at a time as Q_c increased. The lower frequency set lacked the $Q_c = 35k$ due to the coupler becoming too long, hence the 11 instead of 12 pixels.

6.2.2 Basic Measurement Results

Investigation of the basic properties of the hybrid chip showed a $T_c = 1.2$ K and a quasi-particle lifetime $\tau_{qp} \approx 400$ μs. Of the 11 resonators present on the chip 4 were found as significant transmission dips. 7 additional dips were found which could have been either low quality factor resonators or artifacts. These dips were not investigated further. This low yield is likely the result of a mistake during processing. Because the sapphire wafer is transparent a first EBPG writing was done upside down. This resulted in a lot of scratches on the aluminum surface. While inspection under an optical microscope showed direct damage to only 2 of the 11 resonators, further microscopic damage due to the mistreatment could have resulted in lower Q or broken central lines.

The 4 resonators that were identified were matched to their design properties. A comparison of which can be seen in table 6.1. An unusual feature is found in that the measured frequencies are actually higher than the designed frequencies. This mean not the kinetic inductance, but another process is dominating the frequency shift. This could be a result of the impedance mismatch between the 2 sections due to the difference in kinetic inductance. The higher impedance of the narrow section will create an effectively shorter resonator. Combined with the frequency of the kinetic inductance fraction, which is still present, a slightly upwards shifted frequency is the result.

6.3 Fully Submicron Pixels

6.3.1 Submicron Pixel Design

The second test was a 20 by 12 mm chip made of 50 nm aluminum on C-plane sapphire. Centered on it was an array of 8 by 9 pixels with a 1 mm pixel pitch. This meant it fit perfectly below the lens array available at SRON Utrecht. By placing this on the backside of the array optical tests were made possible. Two pixels were made in location that was not covered by the lens array, to have the possibility of seeing the effect of the lenses. The array was designed to have a center frequency of 6 GHz and a pixel spacing in the frequency domain of 5 MHz.

The individual pixel was a half-wave CPW resonator with $S = 600$ nm and $W = 300$ nm as shown in figure 6.3. In order to suppress TLS noise the coupler is made wider, $S, W = 4\ \mu\text{m}$, with 4 μm of ground plane between the coupler and the through line. The long piece perpendicular to the through line was made this way to allow wire bonding over the through line. This suppresses the odd-mode inside it. This odd-mode couples more strongly and differently to the resonators changing the frequency and depth of the resonance dips. In the center of the KID, where it is most sensitive to broken Cooper pairs, a modified version of the X-slot antenna is placed. This version is matched to 1.55 THz radiation, which is SPICA B3, but also impedance matched to the narrow line going through it. This makes it not a design that is simply a scaled version of the original X-slot antenna.

6.3.2 Basic Measurement Results

Of the 74 pixels designed on the chip 64 were detected within a narrow frequency span centered on 4.53 GHz as seen in figure 6.4. The frequency spacing between the pixels was found to be $dF = 4.53 \pm 3.7$ MHz. The internal quality factors of the resonators were found to be $Q_i = (1.4 \pm 0.3) \times 10^6$. While the error on both these values seems rather large the stability of the frequency spacing is typical for an array with a wire-bonded through line. The stability of the internal quality factor is slightly better than what is typically found at SRON. The film in which this array was patterned showed a $T_c = 1.11$ K and a quasi-particle lifetime of $\tau_{qp} = 1.2$ ms. Both values are typical for aluminum films fabricated at SRON.

Table 6.1: The designed, ^{des}, and measured, ^{meas}, parameters of the 4 identified resonators on chip RJ7V1 SPICA pixeltest 22_5.

Number	f_{res}^{des} (GHz)	f_{res}^{meas} (GHz)	$10^{-3} \times Q_c^{des}$	$10^{-3} \times Q_c^{meas}$	$10^{-3} \times Q_i^{meas}$
103	8.2	8.40	100	86	106
108	6.1	6.30	60	54	295
109	6.2	6.47	100	322	430
110	6.3	6.56	500	423	404

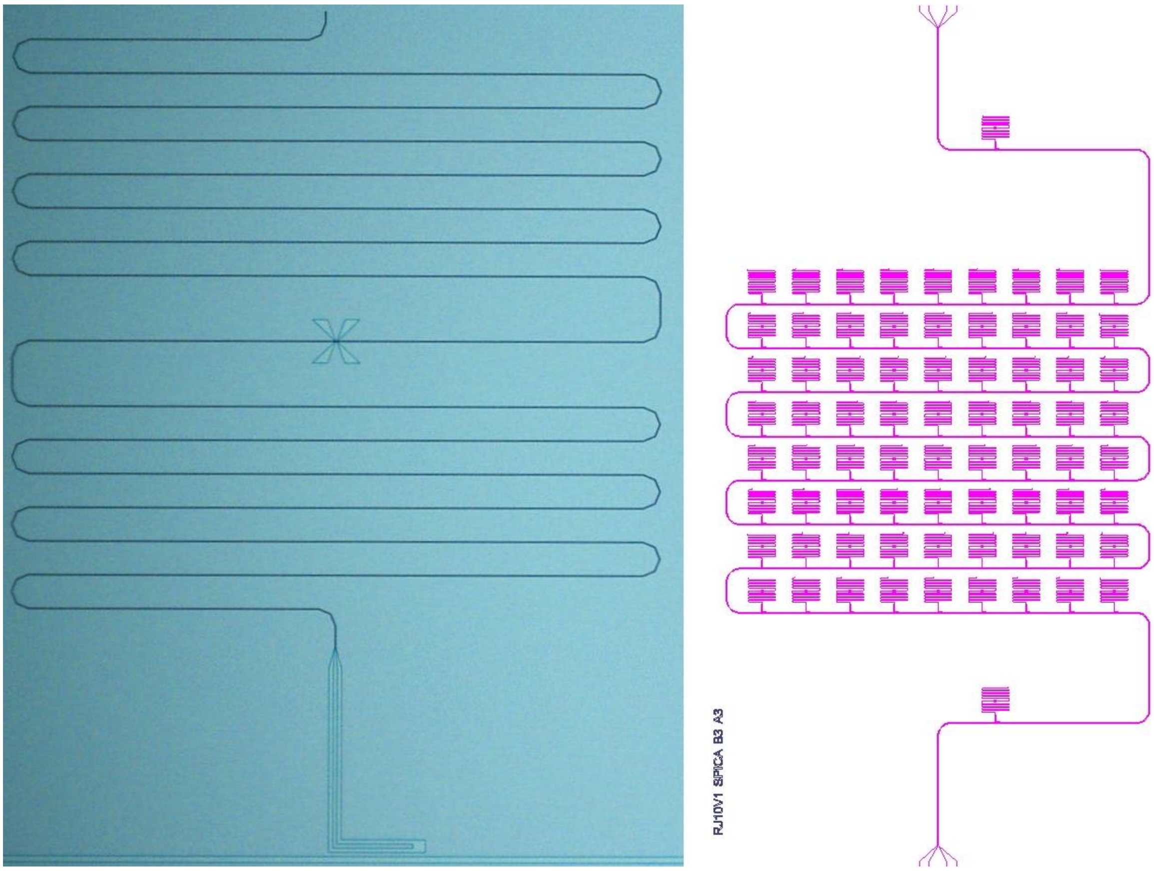

Figure 6.3: A photo taken under an optical microscope of the submicron half-wave design as patterned in the aluminum. In the center of the half-wave, which is the most sensitive part of the KID, a modified version of the X-slot antenna scaled to SAFARI B3 frequencies is placed. To the right is a CAD design showing the full 20 by 12 mm chip containing the 8 by 9 array and 2 blind pixels are placed.

6.4 Micron-sized Pixels

6.4.1 Micron-sized Pixel Design

To see if the performance of hybrid and submicron resonators is indeed a performance improvement their performance the performance of "regular" MKID pixel. The SRON chip K30, as shown in figure 6.5, contains 8 quarter-wave (QW) and 8 half-wave (HW) resonators that are patterned in 40 nm aluminum on c-plane sapphire. These resonators, of which the QW design is shown in figure 1.2(a), were patterned with optical lithography and the three acid wet etch described in section 4.5.1. These micron-sized resonators have a central line $S = 3\ \mu\mathrm{m}$ and slot width of $W = 2\ \mu\mathrm{m}$. For each set of 8 resonators the "444-coupler" is varied in length to create $60k < Q_c < 3M$. The base design frequency is 6 and 8 GHz for the QW and HW resonators, respectively. The resonators have a designed frequency separation of 0.1 GHz.

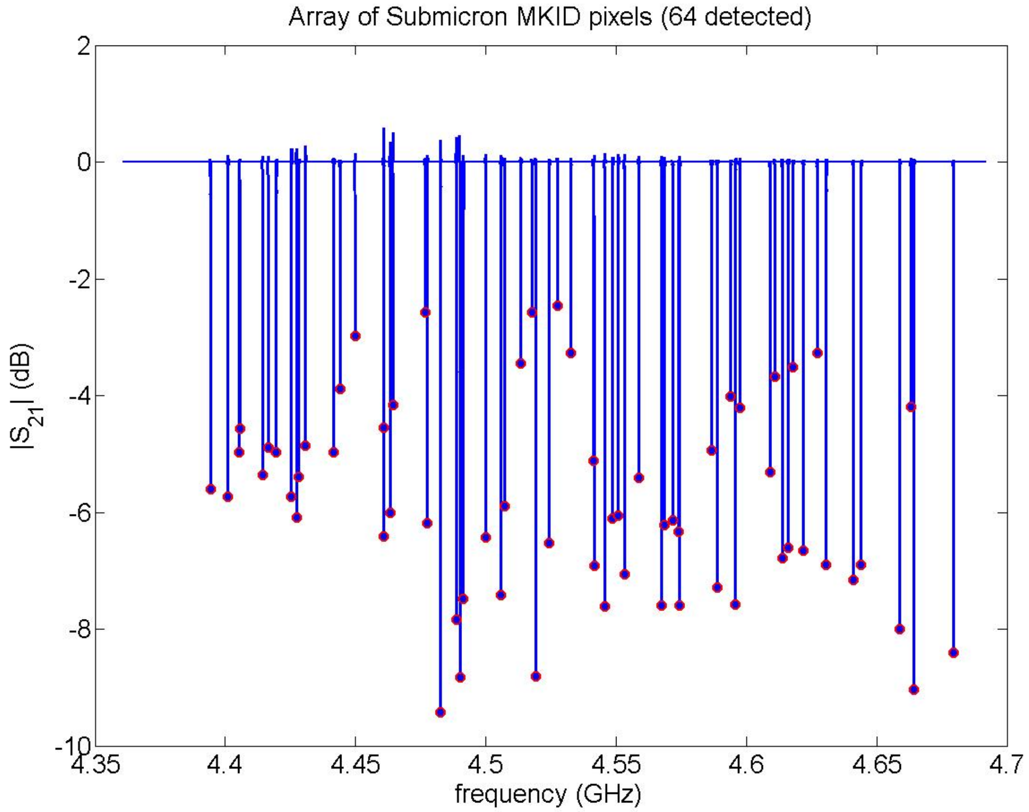

Figure 6.4: 64 resonances of the 74 resonators on the RJ11 chip. The red dots are the maximum depths at the resonance frequency.

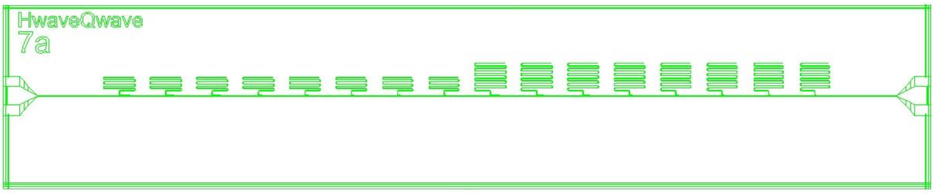

Figure 6.5: The CAD design of the chip containing the 16 micron-sized resonators. Half-wave and quarter-wave resonators can be clearly identified due to their size.

6.4.2 Basic Measurement Results

The aluminum film of the K30 chip had a $T_c = 1.11$ K and quasi-particle lifetime of $\tau_{qp} = 1.3$ ms. All 16 resonators were identified with base frequencies of 5.66 GHz and 6.60 GHz for the QW and HW resonators, respectively. A frequency separation of ≈ 90 MHz was found.

6.5 Pixel Layout Comparison

The performance of the submicron and hybrid resonator is investigating using the "regular" resonators of K30 as a reference. In table 6.2 the T_c, τ_{qp}, mean Q_i and P_{int}^{opt} are summarized for the QW hybrids, HW submicron and HW and QW micron sized resonators. For these resonator layouts the kinetic inductance fraction, responsivity, power handling and noise will be compared. Because the HW and QW micron resonators show similar performance for the properties and the resulting NEP, only the QW micron resonator will be used as reference. To compare the performance the most sensitive resonator of each chip will be used as a representative of this chip. The reference numbers of each of these representatives can be found in table 6.3. In the graphs in this chapter the measurements and fits belonging to the micron, submicron and hybrid design will be shown in black, red and blue, respectively.

6.5.1 Kinetic Induction Fraction

The kinetic inductance fraction can again be determined from the frequency difference between the design and measured frequency. Using equation 3.23 an $\alpha \approx 0.30$ and $\alpha \approx 0.43$ can be determined for the micron and submicron-sized resonator, respectively. For the hybrid pixels this method does not give a good result as their measured frequency is higher than the design frequency.
The second method given in section 5.3.1 using the relative frequency change as a function of temperature as proposed by Gao [32] also does not work. Because the submicron resonances become to shallow to quickly, the temperature sweep went only up to $T = 0.24$ K. This temperature is to low for the relative frequency shift to level off to a steady value.
To get an indication of the kinetic inductance improvement between all three resonator geometries α is determined directly from equation 3.42. While it was shown in section 5.3.1 that this method gives an unreliable absolute value, relative changes can be trusted. Figure 6.6 shows the frequency change as a function of temperature for each of the three pixel designs. From the fits (lines) made to the measured values (stars) kinetic inductance fractions of $\alpha = 13\%$, 23% and 9% was found for the micron, submicron and hybrid resonators, respectively. As expected the submicron resonators have a higher α than the micron resonators. The hybrid resonator, which is expected have an α at least equal or higher than the micron-sized design, has a lower value, however. This can be explained by the fact that the micron design was patterned in a 40 nm film, while the hybrids were in a 100 nm film. Using the theory in section 3.3.2 it can be estimated that the hybrid resonators in a 40 nm film would have an $\alpha \approx 12\%$, giving it a similar value as the "regular" resonators.

6.5.2 Responsivity

The phase responsivity of the 3 reference resonators was determined using the frequency response to temperature method presented in section 5.3.3. The results can be found in table 6.3. In this

Table 6.2: A comparison of the basic properties of the 3 chips measured.

Design	T_c (K)	τ_{qp} (ms)	$10^{-3}\times < Q_i >$	t (nm)	$< P_{int}^{opt} >$ (dBm)
QW Hybrid	1.2	0.4	309 ± 147	100	-36.0 ± 3.2
HW Submicron	1.11	1.2	739 ± 454	50	-54.8 ± 2.6
QW Micron	1.11	1.3	293 ± 143	40	-39.6 ± 2.8
HW Micron	1.11	1.3	243 ± 109	40	-39.4 ± 4.4

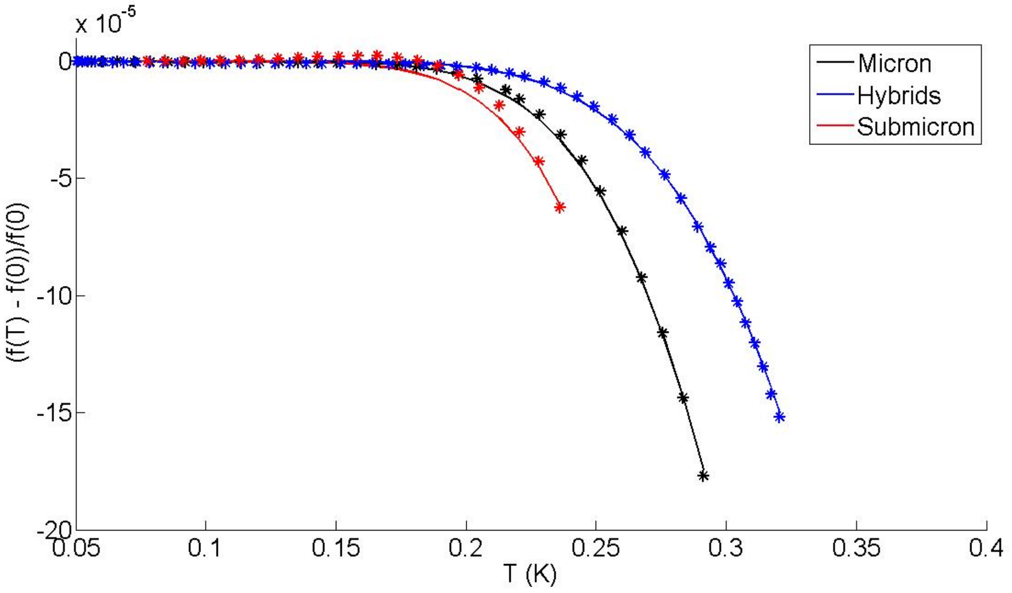

Figure 6.6: The change in resonance frequency as a function of temperature for 3 different resonator designs. The dots are measured values, while the lines are a fit for α based on theoretical calculation of the values for $\sigma_2(T)$. The submicron resonator has a higher $\alpha = 23\%$ than the micron-sized design, $\alpha = 13\%$,as expected. The lower value for the hybrid design, $\alpha = 9\%$, can be explained by the thicker film in which they are patterned.

table also the amplitude responsity is given. This was derived from the phase responsivity using $\frac{dA}{d\theta}$. Following Baselmans et al. [9] $\frac{dA}{d\theta}$ is obtained from lifetime measurements of the aluminum. During these measurements a fast LED pulse is used to excite many QPs in the film. The phase and amplitude response of the resonator will then be measured to see the decay of the QP back to Cooper Pairs. The typical timescale of this decay will be the τ_{qp}. For the small angle response created by the LED A and θ show a linear dependency on each other. A fit can be applied to obtain $\frac{dA}{d\theta}$ and thus $\frac{dA}{dN_{qp}}$=$\frac{dA}{d\theta}\frac{d\theta}{dN_{qp}}$. In table 6.3 it can be seen that the responsivity of the hybrid and submicron resonators has indeed been improved. For the submicron resonators this is even an order of magnitude. As can been seen from equation 3.48 the volume, Q and α are the main influences on the responsivity. The first 2 are given in table 6.3 as well while the latter can be found in the previous section. Using these numbers the difference in responsivity can be explained.

Table 6.3: A comparison of the Q, volume and responsivities of the 3 resonators taken as a representative for each of their designs.

Design	Resonator	$10^{-3} \times Q$	V (μm^3)	$\frac{dA}{dN_{qp}}$	$\frac{d\theta}{dN_{qp}}$
Micron	4	130	560	3.0×10^{-6}	1.5×10^{-5}
Hybrid	109	184	1300	1.2×10^{-6}	6.0×10^{-5}
Submicron	602	311	325	4.1×10^{-5}	1.7×10^{-4}

6.5.3 Power Handling

The optimum internal power to read-out the detectors are $P_{int}^{opt} = -38.7, -59.0, -34.5$ dBm for the micron, submicron and hybrid design, respectively. These values are within 2σ of the average internal power for each design given in table 6.2. Both the hybrid and the submicron resonators show a surprising effect. The power dependence expected in section 3.7 and confirmed in section 5.3.4 using NbTiN is based on geometrical arguments of a maximum current density. This would mean the read-out power is constrained by the narrowest section in the resonator. However, the hybrid and fully micron-sized resonator can handle a similar power, suggesting it is not constrained by the 600 nm central line at the end of the hybrid. A significant constrain does seem to be present in the fully submicron resonators. Their optimum power is 20 dBm lower compared to the other 2 geometries.
An untested hypothesis explaining this difference is the following [88]. Aluminum has, in contract to NbTiN, a very long quasi-particle relaxation time and diffusion distance. This means that the quasi-particles (QPs) in Aluminum will diffuse away from their creation location while this is not the case in NbTiN. This means that the quasi-particles in the narrow section of the hybrid can diffuse out off the narrow end to both the wide part and ground plane. This means that while the current density in the narrow section might be higher, creating more quasi-particles, the critical QP density required to drive the resonator non-linear is not reached. It is only reached when the microwave current is also generating a large amount of QPs in the wide section of the hybrid, which is of equal width as the micron resonator. The submicron resonators on the other hand have no large body of aluminum for the read-out current induced QP to diffuse to. The wider coupler is short compared to the total resonator length and the HW design prevents diffusion into the ground plane through the short in the CPW. For the micron resonators no difference is seen between HW and QW because the QP can diffuse from the edges, where the current is running, to the center. This central volume approximately a factor of 4 smaller for the submicron resonators. So where the micron resonators are limited by the diffusion out-off the current carrying edge, the submicron resonators are limited by the QP density in the full central line.

6.5.4 Noise

The power spectral densities (PSDs) of the noise for the 3 resonator designs can be found in figure 6.7. Both the micron and hybrid design shows a PSD as expected for both amplitude (dashed) and phase (solid) noise. The first is dominated by the system noise, while the latter is dominated by TLS. Little difference is observed as both the power handling is similar and the width of the resonator at the coupler side is similar. This open end is were the TLS predominantly originates from. The PSD of the submicron resonators. The system noise level is higher due to the lower read-out power that can be used. The phase noise shows a “regular” shape its TLS noise is 36 dBc/Hz higher than for the other designs. This increase is most likely caused by the narrower design and lower internal power. The increase is, however, more than the 22 dBc/Hz expected based on the width and power dependences found by Gao [32].
The most striking difference between the submicron and other designs, however, is the 20 dBc/Hz of excess amplitude noise. The most likely cause for this is the mixing of amplitude and phase noise. For high-Q KIDs this high noise level means it will the phase noise will scatter the resonance frequency in such a way that the amplitude measurement is not always on resonance. This mixes the 2 noise signals. The bump at 10^4 Hz is most definitely a result of this mixing and has been observed before in high-Q KIDs [88]. A lower frequencies the source is not so clear as mixing is a less likely candidate. A quasi-particle signal generated by unknown origin could be the cause of this flat PSD as well. Though

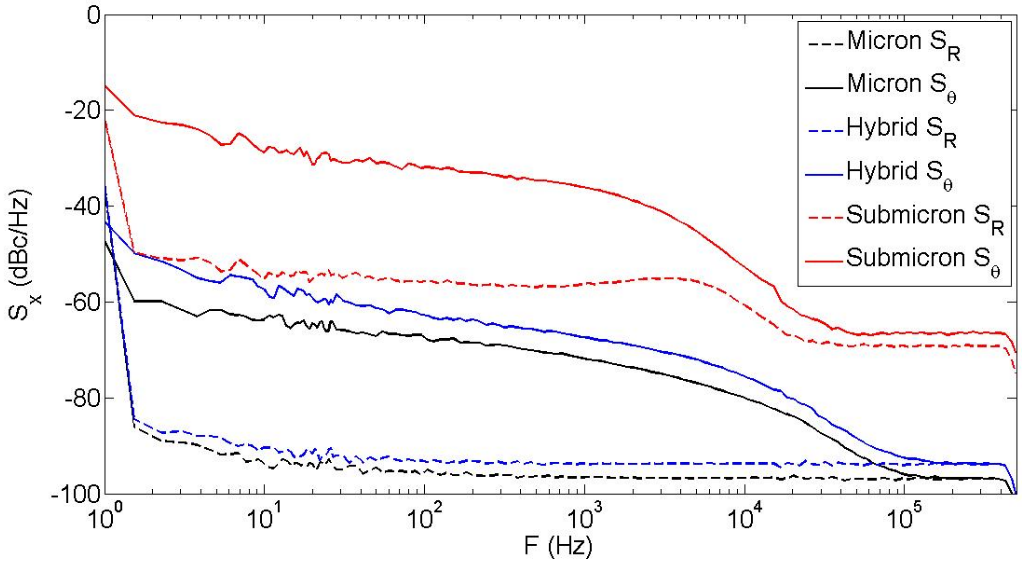

Figure 6.7: The spectra of the noise for the 3 different resonator designs. Both the amplitude (dashed) and phase (solid) noise are given. The system noise level of the submicron resonators is significantly higher due to their lower read-out power.

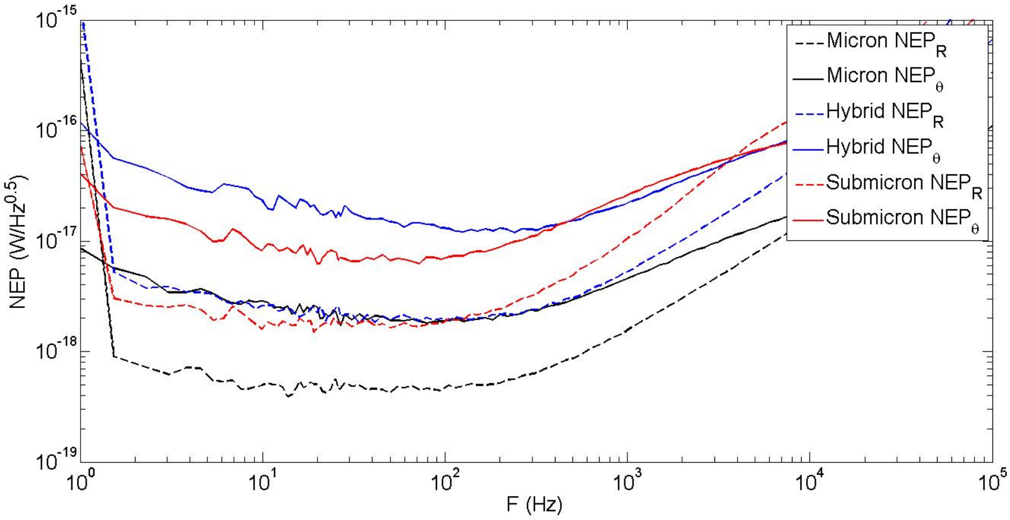

Figure 6.8: The noise equivalent power (NEP) in both amplitude (dashed) and phase (solid) read-out as measured for the 3 resonator geometries.

the level is to high to be generation-recombination noise [20].

6.6 Noise Equivalent Power

The ultimate test for the submicron resonator design is to see if the sensitivity, or NEP, has indeed been improved. In figure 6.8 the measured NEP for phase (solid) and amplitude (dashed) read-out are shown. The hybrid and submicron design have approximately the same NEP, because the higher noise level is compensated by a higher responsivity and longer τ_{qp}. Both are however a factor of ~ 5 worse than the "regular" pixel design as can be seen in table 6.4.

This does not mean, however, that the new design is inferior to the original resonator. The comparison made in this chapter is not completely fair as each resonator was on a different chip. Therefore, a number of factors could be appointed to explain the lower sensitivity of the new designs. For example the variation in Q influences the final performance as can be seen from:

$$NEP_x(\omega) \propto \sqrt{S_x(\omega, P_{int})}\frac{\Delta}{\eta\tau_{qp}}\frac{V}{\alpha Q} \tag{6.1}$$

This equation also helps identify a possible source for the low sensitivity of the 2 new designs. The hybrids for example were patterned in a 2 times thicker film than the other 2. This means a factor of 2 improvement from the volume along. This disregards the effects on α, which will also improve significantly, and the might increase of the phase noise. But since for SAFARI amplitude read-out is planned this is not an issue. The hybrid film also shows a QP lifetime that is 3 times lower. Combined with the volume effect this improved the NEP by a factor of 6.

The film of the submicron resonators is about the same as the micron-sized resonators. Their main performance limitation is the read-out power. However, in amplitude read-out, which is most important for SAFARI, there is also an excess noise source. If this is indeed mixing of the amplitude and phase noise, this is a read-out and not a resonator inherent problem. This means that a S_A at the system level is possible, which gives a 20 dBc/Hz in the noise.

Using these "corrections" for the hybrid and submicron design the NEP in the last two columns of table 6.4 and figure 6.9 can be obtained. Now we indeed see that the first tests of these new designs show equal NEP levels as the "regular" pixel design.

Table 6.4: The noise equivalent power (NEP) at 15 (Hz) for the 3 pixel designs. Given are the measured,^{m}, and "corrected", ^{c}, NEP for amplitude, $_A$, and phase, $_\theta$, read-out. All values are given in W Hz$^{-0.5}$.

Design	NEP_A^m	NEP_θ^m	NEP_A^c	NEP_θ^c
Micron	5.2×10^{-19}	3.8×10^{-18}	5.2×10^{-19}	3.8×10^{-18}
Hybrid	2.3×10^{-18}	2.2×10^{-17}	3.9×10^{-19}	3.6×10^{-18}
Submicron	1.8×10^{-18}	8.2×10^{-18}	4.1×10^{-19}	8.2×10^{-18}

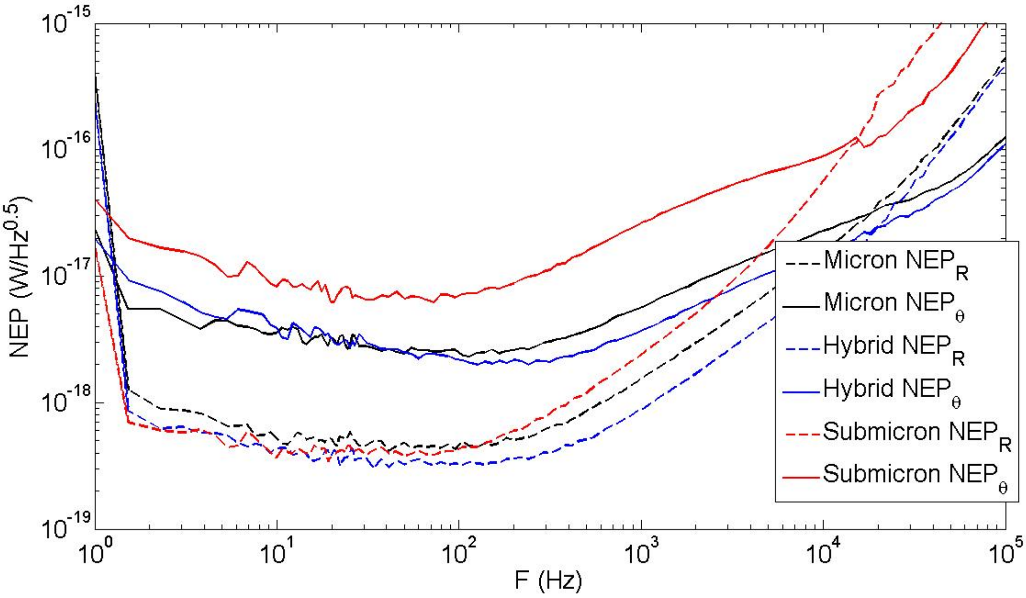

Figure 6.9: The NEP of the micron-sized resonators compared to the NEP of the two new designs after "corrections". For the hybrid design this a compensation of the lower quasi-particle lifetime and the volume effect of the thicker film. For the submicron resonator this is the reduction of the amplitude noise to the system noise level, under the assumption the excess amplitude noise is caused by mixing. Using these assumptions the NEP of all three designs is at an equal level.

Chapter 7

Conclusion and Discussion

The goal of this project was to improve the sensitivity of MKIDs by reducing the width, s, of their coplanar waveguide (CPW) geometry. A reduction of the Noise Equivalent Power (NEP) is needed to create background limited detectors for the SAFARI instrument on SPICA.

This requires the CPW width to be reduced below the limits of optical lithography ($\sim 1\ \mu\mathrm{m}$). Using electron beam lithography and reactive ion etching a fabrication method was developed to make submicron resonators. Initial tests showed a rough edge in the curves of the CPW due to the rectangular exposure grid of the electron beam pattern generator. This problem was amended using a different digital pattern design. Development of this fabrication process should focus on the reduction of the baking time and temperature of the electron sensitive resist. The high temperature is the main suspect for the performance degradation of aluminum resonators on hydrogen passivated silicon.

A systematic study was carried out on the width dependency of the kinetic inductance fraction, quality factor, responsivity, $\frac{d\theta}{dN_{qp}}$, optimum read-out power, P_{opt}, noise, S_θ and NEP of submicron superconducting resonators. Resonators with a central line width varying between 0.3 $\mu\mathrm{m}$ and 3 $\mu\mathrm{m}$ were patterned in a 100 nm NbTiN film on hydrogren passivated silicon. It was shown that:

- $\frac{d\theta}{dN_{qp}} \propto s^{-1.29\pm0.04}$
- $S_\theta \propto s^{-1.28\pm0.21}$
- $NEP_A \propto s^{0.21\pm0.11}$
- $NEP_\theta \propto s^{0.16\pm0.31}$
- $P^{opt} \propto s^{2.16\pm0.20}$

As the resonators become smaller, both the phase responsivity and phase noise show a slower increase than expected from literature. Both effects are most likely due to the differences between the NbTiN used in this experiment and the aluminum used by Gao [32]. The magnetic penetration depth of NbTiN, which was estimated to be 275 nm, is larger than that of aluminum. This means the kinetic inductance did not increase as strongly for decreasing resonator width. Hence, the lower increase in phase responsivity and the abscense of a sensitivity improvement in phase read-out.
The improved sensitivity of submicron resonator in amplitude read-out, which is the read-out mode that will be used for SAFARI, suggests that width reduction is indeed a good way forward.

Therefore, 11 SAFARI B1 pixel prototypes were patterned in a 100 nm aluminum film on a sapphire substrate. The resonator design was the same as "regular" quarter-wave (QW) micron-sized resonators except that the final 20% of their length had a width $s = 660$ nm instead of $s = 2\ \mu\mathrm{m}$. The amplitude responsivity of these resonators was only a factor 2 worse than the micron-sized resonator, despite the fact that their 2.5 times thicker film increased their volume and decreased their kinetic inductance fraction. A sensitivity of $NEP_A = 2.3 \times 10^{-18}$ W Hz$^{-0.5}$ was measured for the hybrid design. However the hybrid design was patterned in a thicker film that showed a three times shorter quasi-particle lifetime. If these are taken into account the sensitivity of the hybrid resonators is expected to be the same as the micron-sized design, $NEP_A \approx 4 \times 10^{-19}$ W Hz$^{-0.5}$.

A prototype array of fully submicron, $s = 600$ nm, SAFARI B3 pixels was made in a 50 nm aluminum film on a sapphire substrate. The uniformity in frequency spacing and quality factor of the submicron array was equal to arrays of micron-sized resonators. Investigation of the individual pixels showed an order of magnitude improvement of the responsivity compared to the micron-sized pixel design. Despite this gain the submicron MKIDs only showed a $NEP_A = 1.8 \times 10^{-18}$ W Hz$^{-0.5}$. The main reasons for this low sensitivity was an unidentified excess amplitude noise of 20 dBc/Hz and a 20 dB lower maximum read-out power. While the excess amplitude noise might be a measurement problem, the low read-out power is a serious problem for submicron resonators.

The power handling appears to be a key issue that will determine if submicron resonators are a viable route to improve the MKIDs sensitivity. Aluminum probably has a different width dependence of its power handling than NbTiN. However, from the prototypes made in this project it is not clear what this difference is. Of all four designs tested in this thesis, only the half-wave submicron resonators have a 20 dB lower P_{opt}. A systematic study of submicron resonators in aluminum, which focuses on the power handling, is therefore required.

Bibliography

[1] O. Almaini, S.E. Scott, J.S. Dunlop, J.C. Manners, C.J. Willott, A. Lawrence, R.J. Ivison, O. Johnson, A.W. Blain, J.A. Peacock, S.J. Oliver, M.J. Fox, R.G. Mann, I. Pérez-Fournon, E. González-Solares, M. Rowan-Robinson, S. Serjeant, F. Cabrera-Guerra, and D.H. Hughes. The coincidence and angular clustering of chandra and scuba sources. *Monthly Notices of the Royal Astronomical Society*, 338:303–311, jan 2003. doi: 10.1046/j.1365-8711.2003.05989.x.

[2] M.D. Audley, W.S. Holland, W.D. Duncan, D. Atkinson, M. Cliffe, M. Ellis, X. Gao, D.C. Gostick, T. Hodson, D. Kelly, M.J. Macintosh, H. McGregor, T. Peacocke, I. Robson, I. Smith, K.D. Irwin, G.C. Hilton, J.N. Ullom, A. Walton, C. Dunare, W. Parkes, P.A.R. Ade, D. Bintley, F. Gannaway, M. Griffin, G. Pisano, R.V. Sudiwala, I. Walker, A. Woodcraft, M. Fich, M. Halpern, G. Mitchell, D. Naylor, and P. Bastien. Scuba-2: A large-format tes array for submillimetre astronomy. *Nuclear Instruments and Methods in Physics Research A*, 520:479–482, mar 2004. doi: 10.1016/j.nima.2003.11.378.

[3] T.J. Baker. Baker prs-3000$^{\mathrm{TM}}$ stripper technical note, 2004. URL `http://www.mallbaker.com/micro/documents/performance/bakerprs3000_tpn.pdf`.

[4] J. Bardeen, L.N. Cooper, and J.R. Schrieffer. Theory of superconductivity. *Physical Review*, 108:1175–1204, 1957.

[5] Barends. Various values for kids, jun 2009.

[6] R. Barends. *Photon-detecting superconducting resonators*. PhD thesis, Delft, University of Techology, Delft, The Netherlands, jun 2009.

[7] R. Barends, N. Vercruyssen, A. Endo, P.J. de Visser, T. Zijlstra, T.M. Klapwijk, and J.J.A. Baselmans. Reduced frequency noise in superconducting resonators. *Applied Physics Letters*, 97(3): 33507–33509, jul 2010. doi: 10.1063/1.3467052.

[8] J. Baselmans, R. Barends, J.N. Hovenier, J.R. Gao, H. Hoevers, P. de Korte, and T.M. Klapwijk. High q niobium superconducting resonators for use as kinetic inductance sensing elements. *Bulletin de la Societe Royale des Sciences de Liege*, 74:491–497, jun 2005.

[9] J. Baselmans, S.J.C. Yates, R. Barends, Y.J.Y. Lankwarden, J.R. Gao, H. Hoevers, and T.M. Klapwijk. Noise and sensitivity of aluminum kinetic inductance detectors for sub-mm astronomy. *Journal of Low Temperature Physics*, 151:524–529, apr 2008. doi: 10.1007/s10909-007-9684-3.

[10] J.J.A. Baselmans and S.J.C. Yates. Long quasiparticle lifetime in aluminum microwave kinetic inductance detectors using coaxial stray light filters. In B. Young, B. Cabrera, & A. Miller,

editor, *American Institute of Physics Conference Series*, volume 1185 of *American Institute of Physics Conference Series*, pages 160–163, dec 2009. doi: 10.1063/1.3292305.

[11] P.N. Best, G. Kauffmann, T.M. Heckman, J. Brinchmann, S. Charlot, Z. Ivezic, and S.D.M. White. The host galaxies of radio-loud active galactic nuclei: mass dependences, gas cooling and active galactic nuclei feedback. *Monthly Notices of the Royal Astronomical Society*, 362: 25–40, 2005.

[12] P.N. Best, A. von der Linden, G. Kauffmann, T.M. Heckman, and C.R. Kaiser. On the prevalence of radio-loud active galactic nuclei in brightest cluster galaxies: implications for agn heating of cooling flows. *Monthly Notices of the Royal Astronomical Society*, 379:894–908, aug 2007. doi: 10.1111/j.1365-2966.2007.11937.x.

[13] H. Bondi. On spherically symmetrical accretion. *Monthly Notices of the Royal Astronomical Society*, 112:195–204, 1952.

[14] M. Cisternas, K. Jahnke, K.J. Inskip, J. Kartaltepe, A.M. Koekemoer, T. Lisker, A.R. Robaina, M. Scodeggio, K. Sheth, J.R. Trump, R. Andrae, T. Miyaji, E. Lusso, M. Brusa, P. Capak, N. Cappelluti, F. Civano, O. Ilbert, C.D. Impey, A. Leauthaud, S.J. Lilly, M. Salvato, N.Z. Scoville, and Y. Taniguchi. The bulk of the black hole growth since z 1 occurs in a secular universe: No merger-agn connection. *ArXiv e-prints*, sep 2010.

[15] R.E. Collins. *Foundations for Microwave Engineering*. McGraw-Hill, New York, 1992.

[16] L.N. Cooper. Bound electron pairs in a degenerate fermi gas. *Physical Review*, 104:1189–1190, nov 1956. doi: 10.1103/PhysRev.104.1189.

[17] D.J. Croton, V. Springel, S.D.M. White, G. De Lucia, C.S. Frenk, L. Gao, A. Jenkins, G. Kauffmann, J.F. Navarro, and N. Yoshida. The many lives of agn: cooling flows, black holes and the luminosities and colours of galaxies. *Monthly Notices of the Royal Astronomical Society*, 365: 11–31, 2006.

[18] J. Dai, J. Zhang, W. Zhang, and D. Grischkowsky. Terahertz time-domain spectroscopy characterization of the far-infrared absorption and index of refraction of high-resistivity, float-zone silicon. *Journal of the Optical Society of America B*, 21:1379–1386, 2004.

[19] P.K. Day, H.G. LeDuc, B.A. Mazin, A. Vayonakis, and J. Zmuidzinas. A broadband superconducting detector suitable for use in large arrays. *Nature*, 425:817–821, 2003.

[20] P.J. de Visser. private communication, 2010.

[21] P.J. de Visser, S. Withington, and D. Goldie. Readout-power heating and hysteretic switching between thermal quasiparticle states in kinetic inductance detectors. *Journal of Applied Physics*, 108:1–10, 2010.

[22] Y. Doi, S. Hirooka, A. Sato, M. Kawada, H. Shibai, Y. Okamura, S. Makiuti, T. Nakagawa, N. Hiromoto, and M. Fujiwara. Large-format and compact stressed ge:ga array for the astro-f (iris) mission. *Advances in Space Research*, 30:2099–2104, 2002. doi: 10.1016/S0273-1177(02)00594-X.

[23] Y. Doi, Y. Sawayama, S. Matsuura, M. Shirahata, T. Arai, S. Kamiya, T. Nakagawa, and M. Kawada. Monolithic ge:ga detector development for safari. In A.M. Heras, B.M. Swinyard, K.G. Isaak, & J.R. Goicoechea, editor, *The Next-Generation Infrared Space Mission: SPICA*, pages 5004–5007, dec 2009. doi: 10.1051/spica/200905004.

[24] H. Dole, G. Lagache, J.-L. Puget, K.I. Caputi, N. Fernández-Conde, E. Le Floc'h, C. Papovich, P.G. Pérez-González, G.H. Rieke, and M. Blaylock. The cosmic infrared background resolved by spitzer. contributions of mid-infrared galaxies to the far-infrared background. *Astronomy & Astrophysics*, 451:417–429, may 2006. doi: 10.1051/0004-6361:20054446.

[25] S. Doyle, P. Mauskopf, J. Naylon, A. Porch, and C. Duncombe. Lumped element kinetic inductance detectors. *Journal of Low Temperature Physics*, 151:530–536, apr 2008. doi: 10.1007/s10909-007-9685-2.

[26] E.F.C. Driessen. private communication, 2010.

[27] A. Endo. private communication, 2010.

[28] A.C. Fabian, J.S. Sanders, G.B. Taylor, S.W. Allen, C.S. Crawford, R.M. Johnstone, and K. Iwasawa. A very deep chandra observation of the perseus cluster: shocks, ripples and conduction. *Monthly Notices of the Royal Astronomical Society*, 366:417–428, feb 2006. doi: 10.1111/j.1365-2966.2005.09896.x.

[29] M. Ferlet, N. Geis, J. Goicoechea, D.K. Griffin, A.M. Heras, K. Isaak, T. Nakagawa, T. Onaka, N. Rando, B. Swinyard, N. Takahashi, and S. Vives. Spica - assessment study report. Technical report, European Space Agency, 2009.

[30] L. Ferrarese and D. Merritt. A fundamental relation between supermassive black holes and their host galaxies. *The Astrophysical Journal*, 539:L9–L12, aug 2000. doi: 10.1086/312838.

[31] L. Ferrari, A.M. Baryshev, J.J.A. Baselmans, G. de Lange, P. Diener, J.W. Kooi, J.J. Lankwarden, and S.J.C. Yates. Kinetic inductance detectors (kids) for the safari instrument on spica. In *Society of Photo-Optical Instrumentation Engineers (SPIE) Conference Series*, volume 7731 of *Presented at the Society of Photo-Optical Instrumentation Engineers (SPIE) Conference*, jul 2010. doi: 10.1117/12.868529.

[32] J. Gao. *The Physics of Superconducting Microwave Resonators*. PhD thesis, California Institute of Technology, Pasadena, California, may 2008.

[33] J.R. Gao. private communication, 2010.

[34] S. Gottlöber, A. Klypin, and A.V. Kravtsov. Merging history as a function of halo environment. *Astroph*, 546:223–233, jan 2001. doi: 10.1086/318248.

[35] M.J. Griffin, J.J. Bock, and W.K. Gear. Relative performance of filled and feedhorn-coupled focal-plane architectures. *Applied Optics*, 41:6543–6554, nov 2002. doi: 10.1364/AO.41.006543.

[36] D. Grischkowsky, S. Keiding, M. van Exter, and C. Fattinger. Far-infrared time-domain spectroscopy with terahertz beams of dielectrics and semiconductors. *Journal of the Optical Society of America B*, 7:2006–2015, 1990.

[37] T.M. Heckman. The co-evolution of galaxies and black holes: Current status and future prospects. In *IAU Symposium*, volume 267 of *IAU Symposium*, pages 3–14, may 2010. doi: 10.1017/S1743921310005508.

[38] E.P. Hubble. Extragalactic nebulae. *Astrophysical Journal*, 64:321–369, dec 1926. doi: 10.1086/143018.

[39] D.H. Hughes, S. Serjeant, J. Dunlop, M. Rowan-Robinson, A. Blain, R.G. Mann, R. Ivison, J. Peacock, A. Efstathiou, W. Gear, S. Oliver, A. Lawrence, M. Longair, P. Goldschmidt, and T. Jenness. High-redshift star formation in the hubble deep field revealed by a submillimetre-wavelength survey. *Nature*, 394:241–247, jul 1998. doi: 10.1038/28328.

[40] N. Iossad. *Metal Nitrides for Superconducting Tunnel Detectors*. PhD thesis, Delft, University of Techology, Delft, The Netherlands, sep 2002.

[41] J.T. Kainulainen, J.F. Alves, Y. Beletsky, J. Ascenso, J.M. Kainulainen, A. Amorim, J. Lima, R. Marques, A. Moitinho, J. Pinhão, J. Rebordão, and F.D. Santos. Uncovering the kiloparsec-scale stellar ring of ngc 5128. *Astronomy & Astrophysics*, 502:L5–L8, aug 2009. doi: 10.1051/0004-6361/200912624.

[42] H. Kamerlingh Onnes. Further experiments with liquid helium g. on the electrical resistance of pure metals etc. vi. on the sudden change in the rate at which the resistance of mercury disappears. *Koninklijke Nederlandse Akademie van Weteschappen Proceedings Series B Physical Sciences*, 14:818–821, 1911.

[43] S.B. Kaplan, C.C. Chi, D.N. Langenberg, J.J. Chang, S. Jafarey, and D.J. Scalapino. Quasiparticle and phonon lifetimes in superconductors. *Physical Review B*, 14:4854–4873, 1976.

[44] G. Kauffmann, S.D.M. White, and B. Guiderdoni. The formation and evolution of galaxies within merging dark matter haloes. *Monthly Notices of the Royal Astronomical Society*, 264:201–218, sep 1993.

[45] A.K. Kembhavi and J.V. Narlikar. *Quasars and Active Galactic Nuclei*. Cambridge University Press, New York, 1999.

[46] P. Khosropanah, B. Dirks, J. van der Kuur, M. Ridder, M. Bruijn, M. Popescu, H. Hoevers, J.-R. Gao, D. Morozov, and P. Mauskopf. Low thermal conductance transition edge sensor (tes) for spica. In B. Young, B. Cabrera, & A. Miller, editor, *American Institute of Physics Conference Series*, volume 1185 of *American Institute of Physics Conference Series*, pages 42–47, dec 2009. doi: 10.1063/1.3292369.

[47] J. Kormendy and D. Richstone. Inward bound—the search for supermassive black holes in galactic nuclei. *Annual Reviews of Astronomy and Astrophysics*, 33:581–624, 1995. doi: 10.1146/annurev.aa.33.090195.003053.

[48] A.G. Kozorezov, A.F. Volkov, J.K. Wigmore, A. Peacock, A. Poelaert, and R. den Hartog. Quasiparticle-phonon downconversion in nonequilibrium superconductors. *Physical Review B*, 61:11807–11819, may 2000. doi: 10.1103/PhysRevB.61.11807.

[49] Y.J.Y. Lankwarden. private communication, 2010.

[50] S.N. Leitner and A.V. Kravtsov. Fuel efficient galaxies: Sustaining star formation with stellar mass loss. *ArXiv e-prints*, nov 2010.

[51] F. London and H. London. The electromagnetic equations of the supraconductor. *Royal Society of London Proceedings Series A*, 149:71–88, mar 1935.

[52] C.J. Lonsdale, D. Farrah, and H.E. Smith. *Ultraluminous Infrared Galaxies*, pages 285–337. Springer Verlag, 2006.

[53] G.A. Mamon. Are cluster ellipticals the products of mergers? *Astrophysical Journal*, 401: L3–L6, dec 1992. doi: 10.1086/186656.

[54] D.C. Mattis and J. Bardeen. Theory of the anomalous skin effect in normal and superconducting metals. *Physical Review*, 111:412–417, 1958.

[55] P. Mauskopf, D. Morozov, D. Glowacka, D. Goldie, S. Withington, M. Bruijn, P. DeKorte, H. Hoevers, M. Ridder, J. Van Der Kuur, and J.-R. Gao. Development of transition edge superconducting bolometers for the safari far-infrared spectrometer on the spica space-borne telescope. In *Society of Photo-Optical Instrumentation Engineers (SPIE) Conference Series*, volume 7020 of *Presented at the Society of Photo-Optical Instrumentation Engineers (SPIE) Conference*, aug 2008. doi: 10.1117/12.788976.

[56] B.A. Mazin. *Microwave Kinetic Inductance Detectors*. PhD thesis, California Institute of Technology, Pasadena, California, aug 2004.

[57] B.A. Mazin, D. Sank, S. McHugh, E.A. Lucero, A. Merrill, J. Gao, D. Pappas, D. Moore, and J. Zmuidzinas. Thin film dielectric microstrip kinetic inductance detectors. *Applied Physics Letters*, 96(10):102504–102506, mar 2010. doi: 10.1063/1.3314281.

[58] J. Mehl, P.A.R. Ade, K. Basu, D. Becker, A. Bender, F. Bertoldi, H.M. Cho, M. Dobbs, N.W. Halverson, W.L. Holzapfel, R. Gusten, J. Kennedy, R. Kneissl, E. Kreysa, T.M. Lanting, A.T. Lee, M. Lueker, K.M. Menten, D. Muders, M. Nord, F. Pacaud, T. Plagge, P.L. Richards, P. Schilke, D. Schwan, H. Spieler, A. Weiss, and M. White. Tes bolometer array for the apex-sz camera. *Journal of Low Temperature Physics*, 151:697–702, may 2008. doi: 10.1007/s10909-008-9738-1.

[59] W. Meissner and R. Ochsenfeld. Ein neuer effekt bei eintritt der supraleitfähigkeit. *Naturwissenschaften*, 21:787–788, nov 1933. doi: 10.1007/BF01504252.

[60] A. Merloni, G. Rudnick, and T. Di Matteo. Tracing the cosmological assembly of stars and supermassive black holes in galaxies. *Monthly Notices of the Royal Astronomical Society*, 354: L37–L42, nov 2004. doi: 10.1111/j.1365-2966.2004.08382.x.

[61] I.F. Mirabel, O. Laurent, D.B. Sanders, M. Sauvage, M. Tagger, V. Charmandaris, L. Vigroux, P. Gallais, C. Cesarsky, and D.L. Block. A barred spiral at the centre of the giant elliptical radio galaxy centaurus a. *Astronomy & Astrophysics*, 341:667–674, jan 1999.

[62] A. Monfardini, L.J. Swenson, A. Bideaud, F.X. Désert, S.J.C. Yates, A. Benoit, A.M. Baryshev, J.J.A. Baselmans, S. Doyle, B. Klein, M. Roesch, C. Tucker, P. Ade, M. Calvo, P. Camus, C. Giordano, R. Guesten, C. Hoffmann, S. Leclercq, P. Mauskopf, and K.F. Schuster. Nika: A millimeter-wave kinetic inductance camera. *ArXiv e-prints*, apr 2010.

[63] D. Morozov, P.D. Mauskopf, P. Ade, M. Bruijn, P.A.J. de Korte, H. Hoevers, M. Ridder, P. Khosropanah, B. Dirks, and J.-R. Gao. Ultrasensitive tes bolometers for space based fir astronomy. In B. Young, B. Cabrera, & A. Miller, editor, *American Institute of Physics Conference Series*, volume 1185 of *American Institute of Physics Conference Series*, pages 48–51, dec 2009. doi: 10.1063/1.3292385.

[64] T. Nakagawa. Spica: space infrared telescope for cosmology and astrophysics. *Advances in Space Research*, 34:645650, 2004.

[65] T. Nakagawa. Spica and its instrumentation. In W. Wild, editor, *Ninteenth International Symposium on Space Terahertz Technology*, pages 20–26, apr 2008.

[66] S. Oliver, M. Frost, D. Farrah, E. Gonzalez-Solares, D.L. Shupe, B. Henriques, I. Roseboom, A. Alfonso-Luis, T.S.R. Babbedge, D. Frayer, C. Lencz, C.J. Lonsdale, F. Masci, D. Padgett, M. Polletta, B. Rowan-Robinson, M. andSiana, H.E. Smith, J.A. Surace, and M. Vaccari. Specific star formation and the relation to stellar mass from $0 < z < 2$ as seen in the far-infrared at 70 and 160 μm. *Monthly Notices of the Royal Astronomical Society*, 405:2279–2294, jul 2010. doi: 10.1111/j.1365-2966.2010.16643.x.

[67] J. Perez, P. Tissera, N. Padilla, and D.G. Alonso, M.S. andLambas. Global environmental effects versus galaxy interactions. *Monthly Notices of the Royal Astronomical Society*, 399:1157–1166, nov 2009. doi: 10.1111/j.1365-2966.2009.15358.x.

[68] A.B. Pippard. An experimental and theoretical study of the relation between magnetic field and current in a superconductor. *Royal Society of London Proceedings Series A*, 216:547–568, feb 1953.

[69] A. Poglitsch, C. Waelkens, N. Geis, H. Feuchtgruber, B. Vandenbussche, L. Rodriguez, O. Krause, E. Renotte, C. van Hoof, P. Saraceno, F. Cepa, J. andKerschbaum, P. Agnèse, B. Ali, P. Altieri, B. andAndreani, J.-L. Augueres, Z. Balog, L. Barl, O. H. Bauer, N. Belbachir, M. Benedettini, N. Billot, O. Boulade, H. Bischof, J. Blommaert, E. Callut, C. Cara, R. Cerulli, D. Cesarsky, A. Contursi, Y. Creten, W. De Meester, V. Doublier, E. Doumayrou, L. Duband, K. Exter, R. Genzel, J.-M. Gillis, U. Grözinger, T. Henning, J. Herreros, R. Huygen, M. Inguscio, G. Jakob, C. Jamar, C. Jean, J. de Jong, R. Katterloher, C. Kiss, U. Klaas, D. Lemke, D. Lutz, S. Madden, B. Marquet, J. Martignac, A. Mazy, P. Merken, F. Montfort, L. Morbidelli, T. Müller, M. Nielbock, K. Okumura, R. Orfei, R. Ottensamer, S. Pezzuto, P. Popesso, J. Putzeys, S. Regibo, V. Reveret, P. Royer, M. Sauvage, J. Schreiber, J. Stegmaier, D. Schmitt, J. Schubert, E. Sturm, M. Thiel, G. Tofani, R. Vavrek, M. Wetzstein, E. Wieprecht, and E. Wiezorrek. The photodetector array camera and spectrometer (pacs) on the herschel space observatory. *Astronomy & Astrophysics*, 518:L2, jul 2010. doi: 10.1051/0004-6361/201014535.

[70] M. Polletta, T.J.-L. Courvoisier, E.J. Hooper, and B.J. Wilkes. The far-infrared emission of radio loud and radio quiet quasars. *Astronomy & Astrophysics*, 362:75–96, oct 2000.

[71] M.d.C. Polletta, B.J. Wilkes, B. Siana, C.J. Lonsdale, R. Kilgard, H.E. Smith, D.-W. Kim, F. Owen, A. Efstathiou, T. Jarrett, G. Stacey, A. Franceschini, M. Rowan-Robinson, S. Babbedge, T.S.R. andBerta, F. Fang, D. Farrah, E. González-Solares, G. Morrison, J.A. Surace, and D.L. Shupe. Chandra and spitzer unveil heavily obscured quasars in the chandra/swire survey. *Astrophysical Journal*, 642:673–693, may 2006. doi: 10.1086/500821.

[72] A. Porch, Mauskopf P., S. Doyle, and Dunscombe C. Calculation of the characteristics of coplanar resonators for kinetic inductance detectors. *IEEE Transactions on Applied Superconductivity*, 15:552–555, 2005.

[73] W. Raab, A. Poglitsch, R. Höhnle, and L. Barl. Development of a large scale stressed ge:ga detector array for safari. In A.M. Heras, B.M. Swinyard, K.G. Isaak, & J.R. Goicoechea, editor, *The Next-Generation Infrared Space Mission: SPICA*, pages 5006–5009, dec 2009. doi: 10.1051/spica/200905006.

[74] G.H. Rieke. *Detection of light: from the ultraviolet to the submillimeter*. Cambridge University Press, UK, second edition, 2003.

[75] R. Sancisi, F. Fraternali, T. Oosterloo, and T. van der Hulst. Cold gas accretion in galaxies. *Astronomy & Astrophysics Reviews*, 15:189–223, jun 2008. doi: 10.1007/s00159-008-0010-0.

[76] P. Schechter. An analytic expression for the luminosity function for galaxies. *The Astrophysical Journal*, 203:297–306, jan 1976. doi: 10.1086/154079.

[77] J. Schlaerth, A. Vayonakis, P. Day, J. Glenn, J. Gao, S. Golwala, S. Kumar, H. Leduc, B. Mazin, J. Vaillancourt, and J. Zmuidzinas. A millimeter and submillimeter kinetic inductance detector camera. *Journal of Low Temperature Physics*, 151:684–689, may 2008. doi: 10.1007/s10909-008-9728-3.

[78] V. Sidorkin, A. van Run, A. van Langen-Suurling, A. Grigorescu, and E. van der Drift. Towards 210 nm electron-beam lithography: A quantitative approach. *Microelectronic Engineering*, 89: 805809, 2008.

[79] L. Spinoglio, M. Magliocchetti, S. Tommasin, A.M. di Giorgio, C. Gruppioni, G. de Zotti, A. Franceschini, M. Vaccari, K. Isaak, F. Pozzi, and M.A. Malkan. Spectroscopic cosmological surveys in the far-ir. In A.M. Heras, B.M. Swinyard, K.G. Isaak, & J.R. Goicoechea, editor, *The Next-Generation Infrared Space Mission: SPICA*, pages 4002–4008, dec 2009. doi: 10.1051/spica/200904002.

[80] V. Springel, C.S. Frenk, and S.D.M. White. The large-scale structure of the universe. *Nature*, 440:1137–1144, apr 2006. doi: 10.1038/nature04805.

[81] J.A. Stern, B. Bumble, H.G. Leduc, J.W. Kooi, and J. Zmuidzinas. Fabrication and dc-characterization of nbtin based sis mixers for use between 600 and 1200 ghz. In R. McGrath, editor, *Ninth International Symposium on Space Terahertz Technology*, pages 305–313, mar 1998.

[82] C. Tasse, P.N. Best, H.J.A. Röttgering, and D. Le Borgne. Radio-loud agn in the xmm-lss field ii. a dichotomy in environment and accretion mode? *Astronomy & Astrophysics*, 490:893–904, 2008.

[83] M. Tinkham. *Introduction to Superconductivity*. McGraw-Hill Book Co., second edition, 1996.

[84] G. E. Vardulakis. *Superconducting Kinetic Inductance Detectors*. PhD thesis, Astrophysics Group, Cavendish Laboratory and Trinity Hall, Cambridge, May 2007.

[85] A. Vayonakis and J. Zmuidzinas. Radiative losses from 2d apertures. 2001.

[86] A. Wallraff, D.I. Schuster, A. Blais, L. Frunzio, R.-S. Huang, J. Majer, S. Kumar, S.M. Girvin, and R.J. Schoelkopf. Strong coupling of a single photon to a superconducting qubit using circuit quantum electrodynamics. *Nature*, 431:162–167, sep 2004. doi: 10.1038/nature02851.

[87] S.R. Whiteley. The cif file format, 2006. URL `http://www.wrcad.com/manual/xicmanual/node493.html`.

[88] S.J.C. Yates and J.J.A. Baselmans. private communication, 2010.

[89] S.J.C. Yates, J.J.A. Baselmans, A.M. Baryshev, A. Neto, G. Gerini, R. Barends, and Y.J.Y. Lankwarden. Antenna coupled kinetic inductance arrays for space and ground based imaging arrays. In B. Young, B. Cabrera, & A. Miller, editor, *American Institute of Physics Conference Series*, volume 1185 of *American Institute of Physics Conference Series*, pages 144–147, dec 2009. doi: 10.1063/1.3292301.

[90] X. Zhou, Y. Wang, and S. Wang. Concise formulas of quasistatic parameter for parallel coupling coplanar lines. *IET Electronics Letters*, 34:1671–1672, 1998.

Appendix A

Submicron MKIDS Fabrication Process

Wafer Cleaning

Silicon - TU Delft

Leybold Hereaus SF_6-etcher (PNE)
O_2 − flow: 25 MLN
Pressure: 0.230 mbar
RF Power: 20 W
RF Voltage: 100 V
Time: 2 minutes

Silicon Oxide Removal in BHF
Chemical: AF 87.5-12.5
Time: 2 minutes
Temperature: 20°C

Sapphire - SRON Utrecht

Cleaning in Aqua Regia
Chemical: Aqua Regia
Time: 10 minutes
Temperature: 100°C

Silicon - SRON Utrecht

See table A.1

Film Deposition

See table A.2

Table A.1: After each step the wafer is rinsed in a beaker of ultra-pure water. The source chemicals used are H_2SO_4, H_2O_2, NH_4OH, HF and H_2O with concentrations of 95%, 30%, 25%, 5% and 100%, respectively.

	removal of	Mixture Type	Volume Ratio Mixture	Temperature	Clean time
1	Organic Contaminant	Piranha	$H_2SO_4 : H_2O_2$ 3:1	95 °C	10 min
2	Particles	SC-1	$NH_4OH : H_2O_2 : H_2O$ 1:1:5	70 °C	10 min
3	Surface Oxides & Hydrogen Passivation	Dilute HF	HF	20 °C	0.5 min

Electron Beam Lithography

Resist and Exposure

Spin HMDS on the wafer at 4000 rpm
Spin PMMA 950k 6% anisol at 4000 rpm on the wafer ($\leq$ 100 nm Al)
Spin PMMA 950k 6% anisol at 1500 rpm on the wafer ($\leq$ 100 nm NbTiN)
Bake for 15 minutes at $175^\circ\mathrm{C}$ on a hot plate

EBPG exposure using a submicron resonator pixel design with a typical dose of 1.2 $\mathrm{mC\ cm^{-2}}$

Development

90 seconds in MIBK:IPA 1:3 mixture
30 seconds in IPA
Blow dry
Quick Dip in IPA and IPA rinse
Blow dry

Reactive Ion Etching

Fluorine Chemistry

Leybold Hereaus $\mathrm{SF_6}$-etcher (PNE)
$\mathrm{SF_6}$ – flow: 13.5 MLN
$\mathrm{O_2}$ – flow: 5 MLN
Pressure: 0.006 mbar (open valve)
RF Power: 230 W
RF Voltage: 50 V
Time: Using laser endpoint detection.

Chlorine Chemistry

Alcater GIR300 etcher (NAF)
$\mathrm{BCl_3}$ – flow: 15 sccm
$\mathrm{Cl_2}$ – flow: 7.5 sccm
$\mathrm{N_2}$ – flow: 10 sccm
Pressure: 0.0100 mbar
RF Power: 50 W
Time: Using laser endpoint detection plus 20 seconds overetch.

Resist Cleaning

Cleaning of unexposed resist
Chemical: PRS3000
Time: 30 minutes
Temperature: $70^\circ\mathrm{C}$

Directly after PRS-bath
Ultrasonic bath for 2 minutes
Rinse with Acetone and IPA
Blow dry

Table A.2: Deposition parameters used in the Nordiko (NbTiN and LLS (Al).

Machine	Target	Argon	$\mathrm{N_2}$	DC Power	DC Voltage	Pressure	Deposition Rate
Nordiko (PNE)	$\mathrm{Nb_{0.7}Ti_{0.3}}$	100 sccm	4 sccm	300 W	300 V	8.0 μbar	53 nm/min
LLS (SRON)	Al	113 sccm	–	876 W	357 V	6.7 μbar	30 nm/min

Acknowledgements

In June 2009 the superconducting resonator expert of the TU Delft, Rami Barends, presented his PhD thesis. During the drinks I met my current supervisor Akira for the first time. I really enjoyed talking to another instrumental astronomer. It was no surprise to me that Teun coupled us for the development of KIDs. Without your guidance the level of this work, especially the astronomical motivation, would not have been of this high a standard. I have really enjoyed working with you, Akira, during the last 1.5 years and I'm looking forward to helping you develop DESHIMA for another 4 years.

Four years in which I hope I can continue to enjoy the created by everyone in the NF group. There are a few persons I would like to thank specifically. Nathan for introducing me to the clean room and having hours of patience as I perfectly aligned the EBPG holder. Rami and Pieter for all the discussions related and unrelated to KIDs. Eduard for the discussion on clean room results and the continued miniaturization of KIDs by another order of magnitude. And finally Robbert-Jan for keeping me company in the largest office of NF.

I also would like to thank the people in the SRON KIDs group for the collaboration during this work. I would like to thank Jochem Baselmans for all the fruitful discussions and design assistance, Stephen Yates for helping me with the measurements in the ADR and Jan-Joost for all the last minute top priority aluminum deposition.

However, this project was not just within the TUD/SRON KIDs community. I would like to thank Berhard Brandl for his supervision from the Leiden Observatory. Even though we might not have had as much discussion as would have been preferable. It was great to see a stronger collaboration arise between UL and TUD on the topic of astronomical instrumentation.

I would also like to thank my friends for all the distractions they provided over the course of this project. In particular I would like to thank Renzo Trip for the last minute corrections on this thesis and Rob Opdam for all the interdisciplinary discussions during much needed hot chocolate breaks and corrections on this thesis. Finally I would like to thank my mother, sister and brother for their continued support and the acceptance of my late night dinner schedule.